QUANTIFYING THE PROPERTIES OF MAGMATIC INTRUSIONS IN THE CENTRAL ANDES WITH GEODESY

A Dissertation

Presented to the Faculty of the Graduate School

of Cornell University

in Partial Fulfillment of the Requirements for the Degree of

Doctor of Philosophy

by

Scott Thomas Henderson

May 2015

QUANTIFYING THE PROPERTIES OF MAGMATIC INTRUSIONS IN THE CENTRAL ANDES WITH GEODESY

Scott Thomas Henderson, Ph.D.

Cornell University 2015

ABSTRACT

Volcanism in convergent arcs is the end result of magma ascending to the Earth's surface. However, many of the details of the ascent process are still debated. In particular, how long does magma persist in reservoirs at particular depths? What is the timescale and physical mechanism of ascent between reservoirs? To address these questions this thesis investigates volcanic deformation in the Central Andes Volcanic Zone of South America (CVZ, 15-28°S). The CVZ is one of three distinct volcanic arc segments in the Andes that results from the subduction of the Nazca Plate beneath the South America Plate. To begin, I compile available information for Holocene eruptions to show that despite containing the largest number of 'active volcanoes' (70), the CVZ has only 12% of recorded eruptions in the Andes. I then demonstrate through a synoptic survey with Interferometric Synthetic Aperture Radar (InSAR) that 40% of volcanic deformation events in the Andes over the last two decades occur in the CVZ. Next, I attempt to constrain the physical properties of two active intrusions in the CVZ that are unique in terms of their large size (>50km diameter) and persistent maximum rates of uplift (>1 cm/yr for >10yrs). First, I focus on Uturuncu Volcano, where I analyze InSAR and GPS data to constrain the spatial and temporal deformation pattern between 1992 and 2014. I propose a 'dipole' model of magma transport between vertically-aligned reservoirs in the lower crust and

middle crust to explain the observation of uplift and peripheral subsidence at Uturuncu. The ratio of vertical to radial surface displacements for single inflation source is increased by adding a dipole reservoir, but decreased to a greater degree by crustal heterogeneity known from seismic tomography. Additionally, volume discrepancies of 1-10x between source and sink reservoirs are expected given known ranges of lower crustal material properties in the Central Andes. Finally, I present current InSAR and GPS observations at Lazufre Volcanic Complex through 10/2014 that show maintained spatial and temporal patterns of uplift compared to the previous two decades. Using a finite element model for an opening sill I demonstrate the role of layering and 3D heterogeneous structure based on newly-available seismic tomography. The proposed heterogeneous structure increases the surface displacements for homogeneous crust by less than 7% within a 10km radius of the center of uplift.

BIOGRAPHICAL SKETCH

The author of this thesis, Scott Henderson, grew up in the Capital City of Washington State, which happens to be about halfway between Mt. Olympus and Paradise. It was a truly impressive place to grow up, surrounded by mountains. Spectacularly big mountains! To this day the most inspirational and awe-inspiring places he's seen were on multi-day hikes through the Cascades and the Olympics. He grew up hearing stories of the infamous 1980 Mt. St. Helens eruption, and witnessed first hand the minor eruption in 2005 from the vantage of Portland, OR. Recognizing the capacity for volcanoes to shape both beautiful and terrifying landscapes inspired Scott to study geology.

In college, Scott opted for the liberal arts, wavering between astronomy and international relations before ending up with a B.A. in physics from Lewis and Clark College and a job with the U.S. Geological Survey. Through astronomy, he recognized the power in remote sensing but soon realized that he preferred pointing the space telescopes back at Earth. So it was that Scott found his way into remote sensing and came to Cornell with the intention of learning the trade and contributing something new to a fascinating field.

I dedicate these pages to my ever-supportive parents, Tom and Heidi

ACKNOWLEDGEMENTS

I feel the need to thank a lot of people for indirectly or directly contributing to this work, so please bear with me. If you're interested in technical details jump right ahead to the table of contents, but if you're interested in some of the back story of this work, this section is for you!

First and foremost I thank those who have been at my side through it all. My family - Tom, Heidi, and Jodi who taught me from the ground up. Without their ceaseless encouragement and support I would never have been able to complete this endeavor. My dear friend Megan Mills-Novoa, who helped me overcome many hard times and celebrate many good ones over the years. My amazing friends in Ithaca - Nimish Pujara, Rayna Bell, Christian Guzman, Thea Whitman, Sheila Saia, Ben Currens, Carrie Freshour. And Amy Willis, for her inspiration, love, and unwavering support over the last year.

Learning starts early and I have all my teachers and peers from the past 24 grades of school to thank for preparing me for the modern world. From my time at Lewis and Clark College, I acknowledge my physics professors Michael Broide and Stephen Tufte for being fantastic educators and getting me going with scientific research. Above all, I acknowledge Liz Safran for cultivating my passion for geology and pointing me towards a job with the USGS; and Dick Iverson and Mark Reid for being an inspirational mentors once I got there.

Over the past five years I've benefited from the camaraderie and inspiration of many colleagues in Cornell Earth and Atmospheric Sciences. I'd especially like to thank my lab mates, Phillip Nee, Holly Taylor, Andrew Melkonian, Bill Barnhart, Veronica Prush, Chelsea Scott, and Francisco Delgado for discussions and help over the years, both in and out of lab: The world (and ROI_PAC) are just too complex to go it alone! An extra special thank you goes to Jennifer Jay

whose friendship and work ethic helped inspire me every step of the way. I'd also especially like to thank Kyle Trostle, Sander Hunter, Felipe Aron, and Chris Siron for their friendship and willingness to explain parts of geology outside of the realm of geophysics. Thank you also to Andes Seminar attendees for great talks and feedback: In particular Muawia Barazangi for keeping us all well-fed and on-track.

I am indebted to my committee members Suzanne Kay, and Alan Zehnder, and Matt Pritchard for enlightening lectures and discussions over the years. Alan taught me everything I know about solid mechanics. Sue helped me navigate the extensive literature of research in the Andes in addition to teaching me the non-geophysical side of volcanoes through classes and a spectacular field course in Argentina. Finally, I am especially appreciative of my advisor Matt Pritchard, for providing constant guidance and unfailing enthusiasm over the last 5 years!

A major component of this research project involved installing geophysical equipment in remote areas of Chile and Bolivia. This simply would not have been possible had it not been for the aid of staff in the Cornell Earth and Atmospheric Science Department: Amy Colvin and Savannah Sawyer in particular. Also, Bolivian colleagues at the Observatorio San Calixto (OSC) in La Paz, and Mayel Sunagua, our collaborator at Sergeotecmin were instrumental in completing field work in Bolivia. In Chile, Sergio Barrientos, Jorge Clavero assisted in getting equipment through customs and guiding our field work. Also, Maria Soledad Bembow at Universidad Catolica del Norte in Antofagasta and Bianca Glass at Universidad de Tarapaca in Arica helped us navigate tricky logistics. Our regular drivers from the Chilean Geological Survey (Sernageomin), Hector Toro and Greco Ramirez went above and beyond to make sure we com-

pleted our sometimes overly ambitious field work goals safely and on time. ¡Les Agradezco!

In this paragraph I'm going to try and thank other researchers who have assisted me in one way or another. Yuri Fialko and Jillian Pearse provided valuable feedback at conferences and have provided ROI_PAC processing tips and other modeling software used in this study, in particular Chapter 2. Finite element models in Chapters 3 and 4 benefited from the timely and useful responses of developers Brad Aagaard, Charles Williams, and Matthew Knepley. Paul Lundgren was generous to share InSAR data for Lazufre used in Chapter 4. Julie Elliott helped coordinate the campaign GPS survey at Lazufre, and processed campaign and continuous GPS data that was instrumental for chapters 3 and 4. Yo Fukushima helped us access ALOS data and provided feedback on several manuscripts. Eric Fielding provided assistance with modifying ROI_PAC codes. I also thank members of the PLUTONS team for critical discussions, sharing preliminary results, and Zack Spica and Kevin Ward for kindly providing preliminary velocity models based on their work. Finally, most of the figures in this report were created with Python packages, in particular the Matplotlib library (*Hunter*, 2007).

This work was supported by multiple National Aeronautics and Space Administration (NASA) grants NNX10AN57H, NNX08AT02G, NNX12AM24G issued through the Science Mission Directorate's Earth Science Division. Funding was also provided by NSF (National Science Foundation) grant 0908281 which is part of the PLUTONS project (http://plutons.science.oregonstate.edu). So a much deserved acknowledgement goes to the tax-paying public for supporting science in general, and my work in particular!

TABLE OF CONTENTS

LIST OF TABLES

LIST OF FIGURES

CHAPTER 1

CENTRAL ANDES VOLCANIC ZONE IN GLOBAL AND REGIONAL CONTEXT

Volcanic eruptions are one of the most awe-inspiring natural processes on our planet, renowned for their beauty and destructive power. Our quest to understand them stems from both a timeless curiosity and a need to protect a growing population living in proximity to volcanic centers. As of 1990, approximately 12% of the population lived within 100 km of a volcano active within the Holocene (*Small and Naumann*, 2001). Although this percentage has not been updated 25 years later, it has likely remained constant or grown slightly with increasing urbanization.

In a recent research review, *Cashman and Sparks* (2013) point out that major advancements in our understanding of volcanoes over the last 25 years are owed largely to technological advances in equipment for monitoring and modeling. With a vast accumulation of geophysical, geochemical, and petrological datasets there is an ongoing effort to create databases from which patterns in eruptive behavior can be identified. In addition to acknowledging the importance of modern data collection and organization, *Cashman and Sparks* (2013) note that long-term forecasts of volcanic hazard are probabilistic and largely determined by eruptive deposits not observed in human history. The most recent edition of the authoritative database of Holocene volcanic eruptions, Volcanoes Of The World Database (VOTW), has been available in print since 1981 (*Siebert et al.*, 2011). Since May, 2013 the database has been available for public download (*Venske et al.*, 2014). In Section 1.2, I bring up to date the current database of global volcanic deformation events, and draw connections with the Holocene

eruption catalog.

In an effort to compare explosive eruptions globally, the Volcano Explosivity Index (VEI), a semi-quantitative logarithmic scale of eruptive volumes was developed (*Newhall and Self*, 1982). Considered relatively complete for moderate size eruptions (VEI>2), studies have used the catalog to assess the frequency and distribution of Holocene eruptions (e.g. *Deligne and Coles*, 2010). Minor eruptions often go unnoticed and leave little trace in the geologic record, and thus despite being potentially hazardous are underreported (*Houghton et al.*, 2013). On the other end of the scale, very large explosive "super-eruptions" (VEI>7) have never occurred in historical time and consequently their recurrence intervals must be inferred from the geologic record (*Mason et al.*, 2004). Several databases of these large caldera-forming eruptions have been created to assess global trends in these large-scale eruptions since they are extremely rare, but certainly pose a threat to the global population (*Geyer and Martí*, 2008; *Crosweller et al.*, 2012).

The Central Andes Volcanic Zone (CVZ) is a unique volcanic arc because it shows evidence for two distinct modes of volcanism: Abundant caldera-forming eruptions during the Miocene, and smaller volume eruptions of stratovolcanoes characteristic of most convergent arcs. Therefore, the CVZ is an excellent case study for the synthesis of modern instrumentation with studies of past volcanism from the geologic record. While the majority of this thesis focuses on interpreting the geophysical observations from the last several decades, I first review our current understanding of the geologic setting of the CVZ.

1.1 Central Andes Volcanic Zone

The CVZ, 14°S to 28°S, is one of four distinct segments of the volcanic arc along the western margin of South America (Figure 1.1). To the north, the Northen Andes Volcanic Zone (NVZ) consists of volcanoes in Colombia and Ecuador, and to the south, the Southern Andes Volcanic Zone (SVZ) and Austral Andes Volcanic Zone (AVZ) consist of volcanoes in Chile and Argentina. Subduction of the Nazca Plate beneath the South America Plate drives CVZ volcanism, which terminates to the north and south at the Peruvian and Chilean-Pampean flat slab segments (e.g. *Barazangi and Isacks*, 1976; *Cahill and Isacks*, 1992). High elevation, thick crust, and a high concentration of silicic calderas are unique characteristics of this volcanic region (e.g. *Isacks*, 1988; *de Silva*, 1989; *Allmendinger et al.*, 1997), which contains 69 Holocene edifices, at least 13 of which have erupted in the last century (*Siebert et al.*, 2011).

Previous analysis of the VOTW database has highlighted that the Andes altogether hosts more stratovolcanoes with Holocene eruptions (122) than any other volcanic region globally (*Tilling*, 2009). However, it is important to keep in mind that evidence for Holocene activity falls into one of six categories of varying reliability (Figure 1.2). Compared to the rest of the Andes, the CVZ contains the most volcanoes (40%), but the majority of these are included in the VOTW based on 'uncertain' and 'undated' evidence (Figure 1.3).

The VOTW also contains detailed information on over 1000 'confirmed' Holocene eruptions in continental South America, with an apparent magnitude of completeness of VEI=2 (Figure 1.4). In Figure 1.2 I show the tallies of these eruptions broken up by volcanic zone, which demonstrates the general lack of

eruptions in the CVZ. To summarize, in comparison to the other Andean volcanic segments, the CVZ contains approximately 40% of the volcanoes active during the Holocene, but less than 13% of documented eruptions (Figure 1.6).

However, synoptic geodetic observations since 1992 have so far revealed half of the 20 known uplifting volcanoes in the Andes are in the CVZ (Table 1.1). Several of these uplift signals are unique globally in that they have large spatial extents, high amplitudes, and long durations (see section 1.1.1). Furthermore, an especially high concentration of Miocene ignimbrite deposits ($>$ 10,000 km^3) suggests that in the past large volumes of eruptible magma traversed the crust in this region (*de Silva*, 1989). These observations suggest that magmatic intrusions are in fact common in the CVZ, but crustal conditions tend to favor plutonic solidification or accumulation in extremely large reservoirs that erupt infrequently.

Previous petrological studies indicate multiple viable levels of magma storage within the thick crust of the CVZ. Three principal magma storage depths have been deduced by petrologic studies of a concentration of Tertiary ignimbrites in the CVZ known as the Altiplano-Puna Volcanic Complex (APVC), 21°S to 24°S, (*de Silva*, 1989): Mantle melts initially pond and mix at 60-70km, evolve at 20-25 km depth, and evolve further at 4-8 km prior to eruption (e.g. *de Silva and Gosnold*, 2007; *Kay et al.*, 2010a). Interestingly, much of the areal extent of the APVC is underlain by a geophysically imaged layer of partial melt at 19 km below topography, known as the Altiplano-Puna Melt Body (APMB) (*Chmielowski et al.*, 1999; *Zandt et al.*, 2003; *Schilling et al.*, 2006). Two important points regarding the APMB must be made here. First, different authors prefer various names for this feature; for example, *Fialko and Pearse* (2012) refer to

it as the Altiplano-Puna Ultra Low Velocity Zone (APULVZ). Second, a recent joint inversion of ambient noise tomography and receiver functions from an expanded network of stations has drastically changed the geometric description of the APMB: It has been proposed to be a much thicker zone of ultra-low velocities ($1.9 < Vs < 2.9$ km/s) between 5 to 25 km depth, and a diameter of over 200 km (*Ward et al.*, 2014). Thus, the APMB is agreed to represent an extensive network of partial melt; however, the exact subsurface geometry of the APMB and percentage of partial melt are still debated. Evidencing the uncertainty in what this feature represents is the numerous names assigned to the 'M' in 'APMB': Magma, Melt, or Mush.

1.1.1 Uturuncu and Lazufre

Uturuncu Volcano is the only deforming volcano in the CVZ that has a clear association with the Altiplano-Puna Magma Body: It is located well within the mapped areal extent of this seismically imaged low velocity zone (Figure 2.1), and geodetic model depths coincide with the mid-crustal depth of the APMB (*Pritchard and Simons*, 2004). An array of 15 seismometers deployed between 04/2009 - 04/2010 at Uturuncu has shown a high rate of volcano-tectonic seismicity compared to other inflating volcanoes without accompanying eruptions: This seismicity is concentrated at a depth of 5km, exhibits frequent swarms, and shows evidence for dynamic triggering by 27 February 2010 Maule earthquake (*Jay et al.*, 2012). Given these observations, it is possible that the active inflation in the mid-crust is causing small earthquakes by perturbing the stresses on overlying faults (e.g. *Savage and Clark*, 1982; *Bonafede et al.*, 1986; *Sparks et al.*, 2008).

It is unclear whether the APMB is an ephemeral feature or if it is a long-lived source of the APVC eruptions. Nevertheless, previous geodetic inverse modeling places the Uturuncu deformation source between 12-25km (*Pritchard and Simons*, 2004). More recent numerical forward modeling of geodetic data may indicate that the interconnected partial melts of the APMB are currently feeding a large diapir rising beneath Uturuncu volcano (*Fialko and Pearse*, 2012). Measurement of active diapiric ascent is unprecedented and raises questions about the pervasiveness of diapir-related surface deformation (*Brooks*, 2012). In Chapter 3 we present an alternative model of magma transport between vertically-aligned reservoirs in the middle and lower crust.

Approximately 350 km south of Uturuncu, uplift at Lazufre Volcanic Center is well outside the bounds of the APMB. In this region, crustal thickness is substantially less compared to Uturuncu (45-55 km) (*Yuan et al.*, 2002; *McGlashan et al.*, 2008). P-wave tomography from a dense local array of seismometers just south of Lazufre suggests mid-crustal low velocities elsewhere, although velocity reductions are as great as those observed for the APMB (*Bianchi et al.*, 2013).

1.1.2 Summary of CVZ Deformation

The Central Andes Volcanic Zone was previously known to contain 7 volcanoes that have exhibited surface deformation since 1992: Ticsani, Hualca Hualca, Uturuncu, Lazufre, Cerro Blanco, Lastarria, and Lascar (Figure 1.10). Our analysis from Chapter 2 adds two volcanoes to the list - Putana and Cerro Overo - and we extend previous time series analyses to bring observations through 2011 (*Henderson and Pritchard*, 2013). Following publication of that study we discov-

ered uplift at Sillajhuay Volcano, which is described in (*Pritchard et al.*, 2014). Of particular note is that most deforming volcanoes in the CVZ are not thought to be active (not listed in the VOTW database). Sillajhuay in particular is intriguing because it is a Pliocene edifice (*Gonzalez-Ferran*, 1995), although recent unpublished Ar-Ar ages from summit lavas give ages of 1.4 Ma (M. Salisbury pers. comm.). Sillajhuay is also located within the 'Pica Gap' - a 100 km region of the volcanic arc with no Holocene volcanoes between Isluga and Irruputuncu (*de Silva and Francis*, 1991). Thus, Sillajhuay and Uturuncu in particular underscore the need for monitoring not only volcanoes that are considered active.

1.2 Global Volcanic Deformation

One of the many indicators of volcanic activity is displacement of the surface of the Earth induced by intrusion of magma into the subsurface. As magma ascends, it either must displace existing material or intrude into and pressurize pre-existing chambers. If the intrusion is of sufficient magnitude or located at shallow depth, resulting elastic strain at the surface is detectable with geodetic instrumentation such as leveling surveys, tiltmeters, and the Global Positioning System (GPS). The mathematical framework for models of crustal deformation is discussed in more detail in Chapter 3 and Chapter 4, or a comprehensive review is given in *Poland et al.* (2006). In this section we focus on reported historical observations of surface deformation at volcanoes.

A major effort to compile observations of volcano deformation was undertaken by *Dvorak and Dzurisin* (1997). Measurements during most of the 1900s used ground-based instrumentation, and therefore observations were biased to-

wards the most active volcanoes near population centers. Consequently, as of 1997, only 44 volcanoes globally were known to have exhibited deformation.

A major advancement in detection and analysis of volcano deformation came with the first application of Interferometric Synthetic Aperture Radar (InSAR) to Mt. Etna in 1995 using the European Remote Sensing Satellite-1 (ERS-1) Satellite (*Massonnet et al.*, 1995). InSAR satellites are capable of measuring subcentimeter relative displacements of the Earth's surface in the radar line-of-sight by converting phase shifts in two radar scenes to ground displacements. For details of InSAR sensors and data processing, we refer the reader to the following review papers: (*Rosen et al.*, 2000; *Buergmann et al.*, 2000; *Simons and Rosen*, 2007). The footprint of InSAR scenes is typically on the order of 100 km and the resolution on the ground is on the order of 10-100 m^2. Thus, InSAR enabled the first synoptic surveys of volcanic arcs at very high spatial resolution (e.g. *Lu et al.*, 2002; *Pritchard and Simons*, 2002), and the technique became a standard tool in monitoring volcanoes at different stages in the eruptive cycle (*Dzurisin*, 2000, 2003).

As of 2010, the number of volcanoes with observed deformation grew to 110, largely due to detections by InSAR (*Fournier et al.*, 2010). With this larger dataset it became apparent that deformation events lasted from days to years, with displacement rates between 1 mm/yr to 10 m/yr. With continued observation, more satellites, and more elapse time, the number of deforming volcanoes has increased to 214 as of writing. The progression of detections of volcanic deformation and availability of new monitoring technologies is illustrated in Figure 1.7.

Figure 1.8 presents a current map of volcanoes where surface deformation

has been observed. It is clear that deformation is not limited to a particular volcanic arc or tectonic setting. Furthermore, the detection of uplift events (75%) greatly exceeds subsidence events. Since volcanic subsidence is typically associated with draining of magma reservoirs during eruptions, it is possible that subsidence events are easier to miss due to temporal aliasing of observations. On the other hand the discrepancy might reflect that magmas are prone to ascend and solidify as plutons. Typically, deformation at volcanoes is categorized as Inter-Eruptive, Eruptive, or Post-Eruptive, and displacements are averaged over the time period of discrete observations. We present a global synthesis of deformation events in terms of their magnitude and duration in Figure 1.9. For an excellent review of the basic theory of InSAR and its application to volcanic studies over the last two decades we refer the reader to (*Pinel et al.*, 2014).

1.2.1 Relating Deformation and Eruption

The connection between volcanic deformation and eruption is not necessarily straightforward. Deformation is sometimes clearly observed preceding major eruptions - for example Cordon Caulle in 2010 (*Jay et al.*, 2014). However, sometimes eruptions occur without observed deformation - for example Lascar in 1993 (*Pritchard and Simons*, 2004). And furthermore, calderas have been observed to deform episodically without erupting - for example Yellowstone (e.g. *Newhall and Dzurisin*, 1989). Nevertheless, a key finding of a recent review of the 198 volcanoes systematically observed for the past 18 years is that 54 deformed, of which 25 also erupted (*Biggs et al.*, 2014). Thus geodetic monitoring provides an important forewarning of imminent eruptions at stratovolcanoes, and helps us understand magma accumulation at restless calderas.

1.3 Narrative Outline

Here I briefly outline what is discussed in the remaining chapters of this thesis. See Section 5 for a brief summary of major findings from each chapter.

Chapter 2

In order to identify decadal trends at previously identified centers of deformation, and discover new deforming regions over a large area, we perform an Interferometric Synthetic Aperture Radar (InSAR) time series analysis over most of the Central Andes Volcanic Zone (19°S - 27°S). These tracks cover over $100,000 km^2$ and cover the years 1992 through 2010. Our analysis extends observations at Cerro Blanco, Uturuncu, and Lazufre volcanic centers and uncovers two previously undocumented deformation centers Cerro Overo in Northern Chile, and Putana Volcano in Southwest Bolivia.

Chapter 3

This chapter focuses on evaluating a dual-reservoir model for the observations of deformation at Uturuncu Volcano presented in Chapter 1. Vertically-aligned 'dipole' magma reservoirs represent a physically plausible model for deformation at Uturuncu Volcano. The ratio of vertical to radial surface displacements for single inflation source is increased by adding a dipole 'source' reservoir (deflation), but decreased to a greater degree by crustal heterogeneity. Volume discrepancies of 1-10x between source and sink reservoirs are expected given known ranges of lower crustal material properties

Chapter 4

New InSAR and GPS observations at Lazufre Volcanic Center are presented, extending observations through September, 2014. Spatial and temporal patterns of deformation appear consistent with pre-2010 measurements. Previous modeling efforts have focused on inversions for sill-like sources in a homogenous elastic half-space. We present a finite element model that utilizes newly-available seismic tomography to evaluate the role of heterogeneous crustal structure.

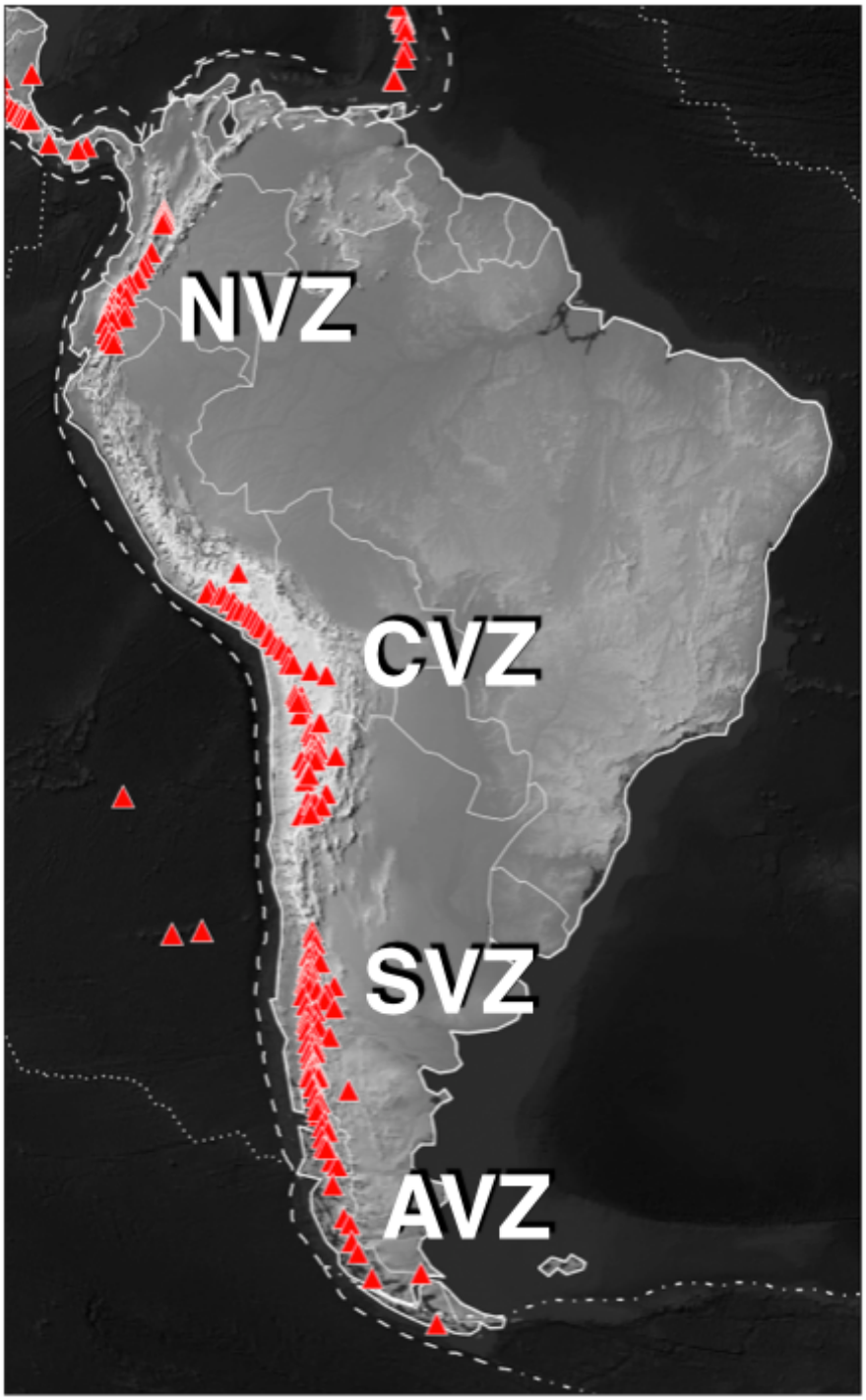

Figure 1.1: Major volcanic zones of the Andes. Red triangles are volcanoes from the VOTW database for the Northern, Central, Southern, and Austral Volcanic Zones (*Venske et al.*, 2014). Dashed white lines represent convergent plate boundaries, dotted white lines are divergent boundaries, and dash-dot lines are strike-slip boundaries.

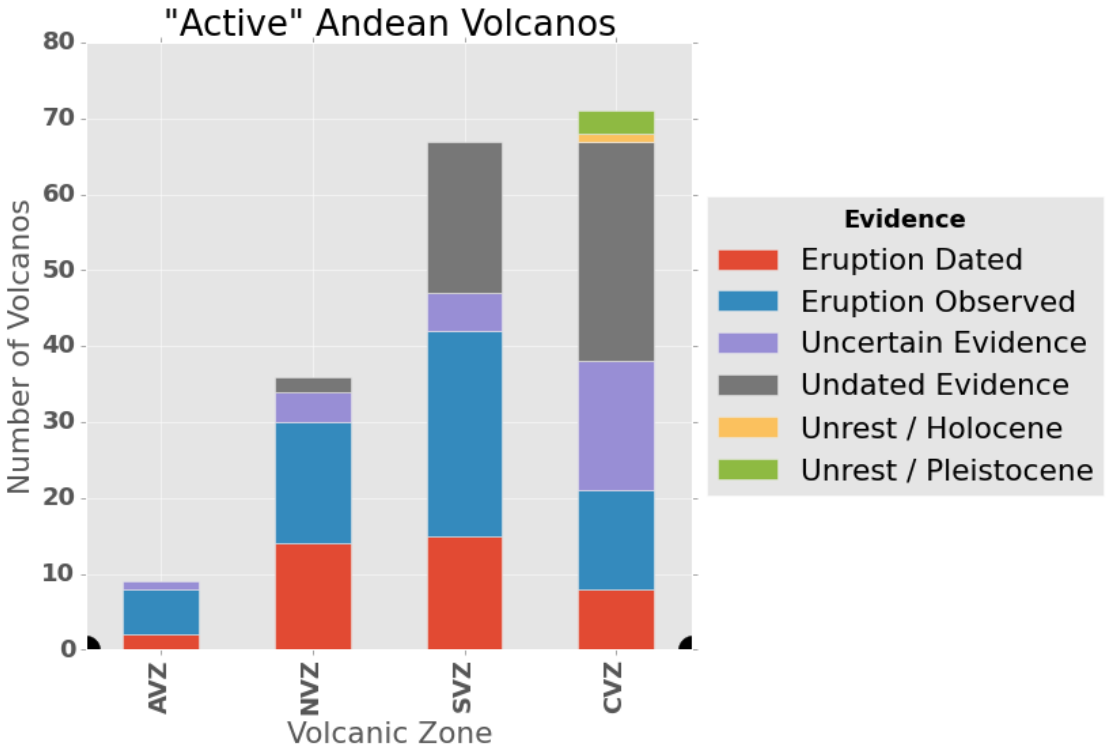

Figure 1.2: Holocene volcanic activity among Andean Volcanic Zones for volcanoes included in the VOTW. Note that while CVZ has the largest number of volcanoes, the majority of them are included on the basis of 'uncertain' or 'undated' evidence (for example apparent postglacial eruptive deposits).

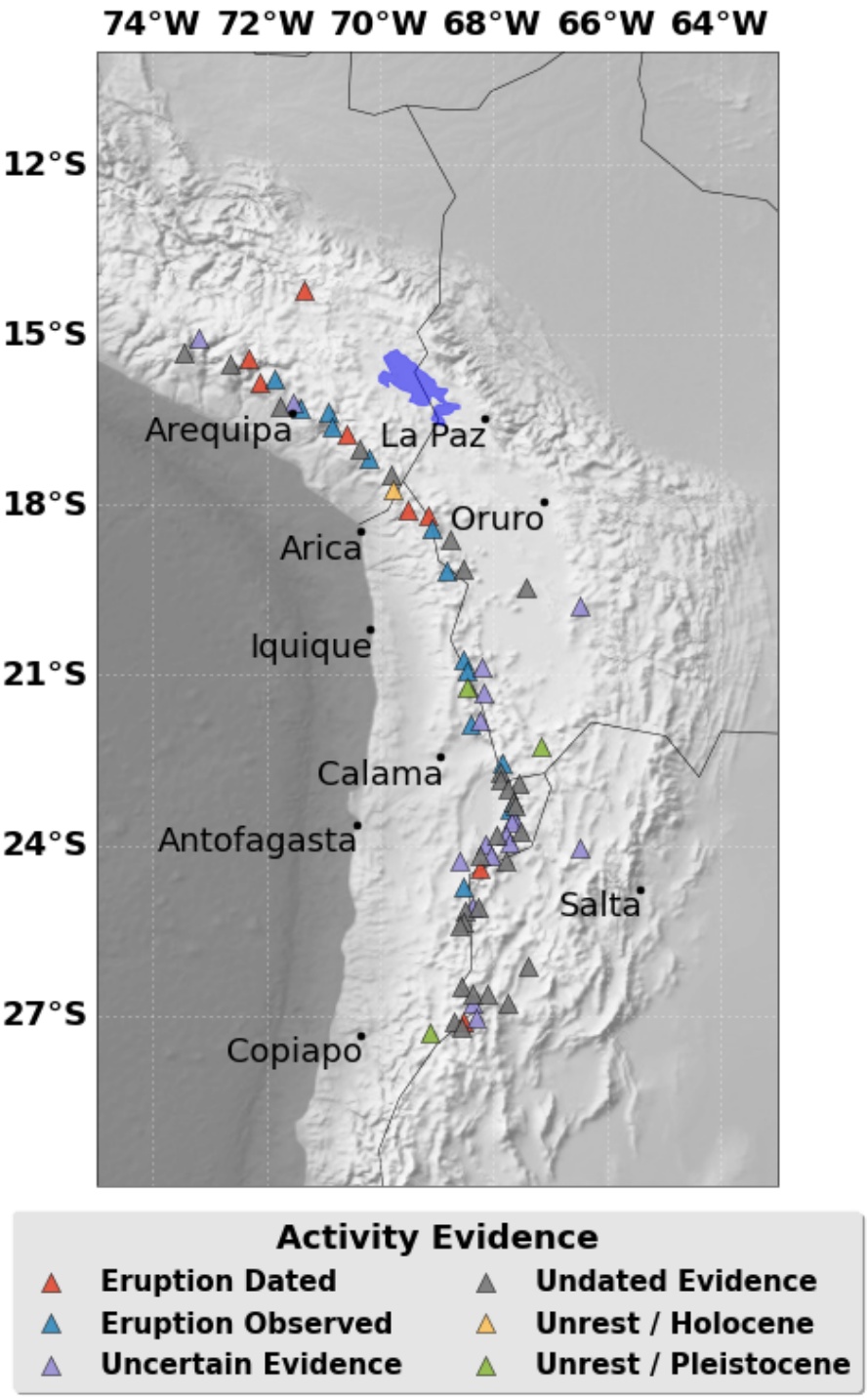

Figure 1.3: Map of volcanoes in the Central Andes Volcanic Zone (CVZ) included in the VOTW, colored by type of evidence cited for inclusion in the catalog. See Figure 1.2 for bar chart comparing evidence for other volcanic zones in the Andes.

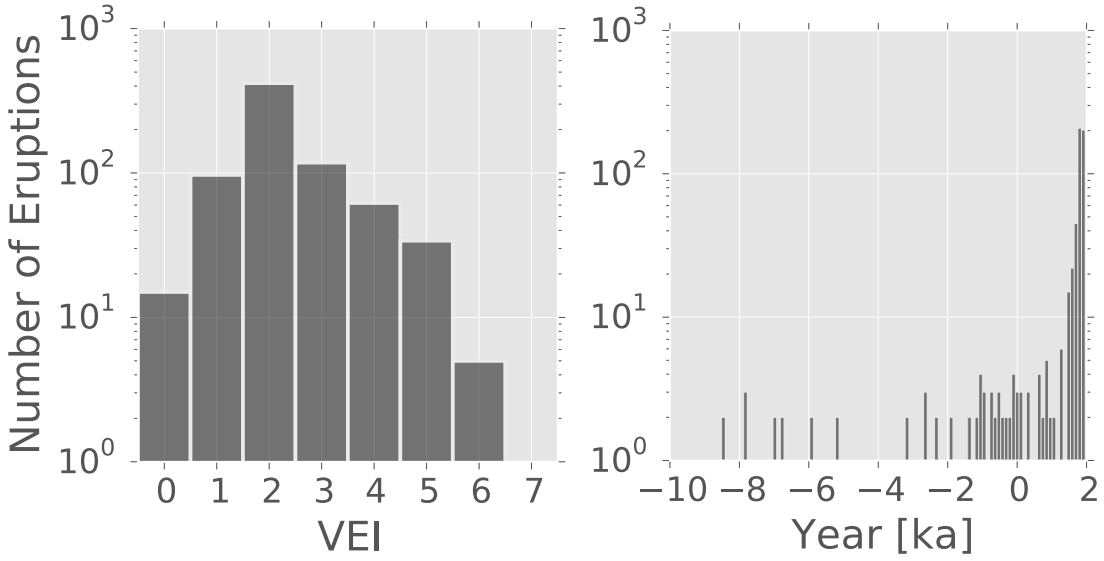

Figure 1.4: Left: Histogram of Holocene eruptions of South America binned by Volcano Explosivity Index (VEI). Right: Timeline showing recorded eruptions per year. Data from VOTW, note that magnitude of completeness appears to be VEI=2, due to the decreasing likelihood of witnessing and preserving deposits from smaller eruptions.

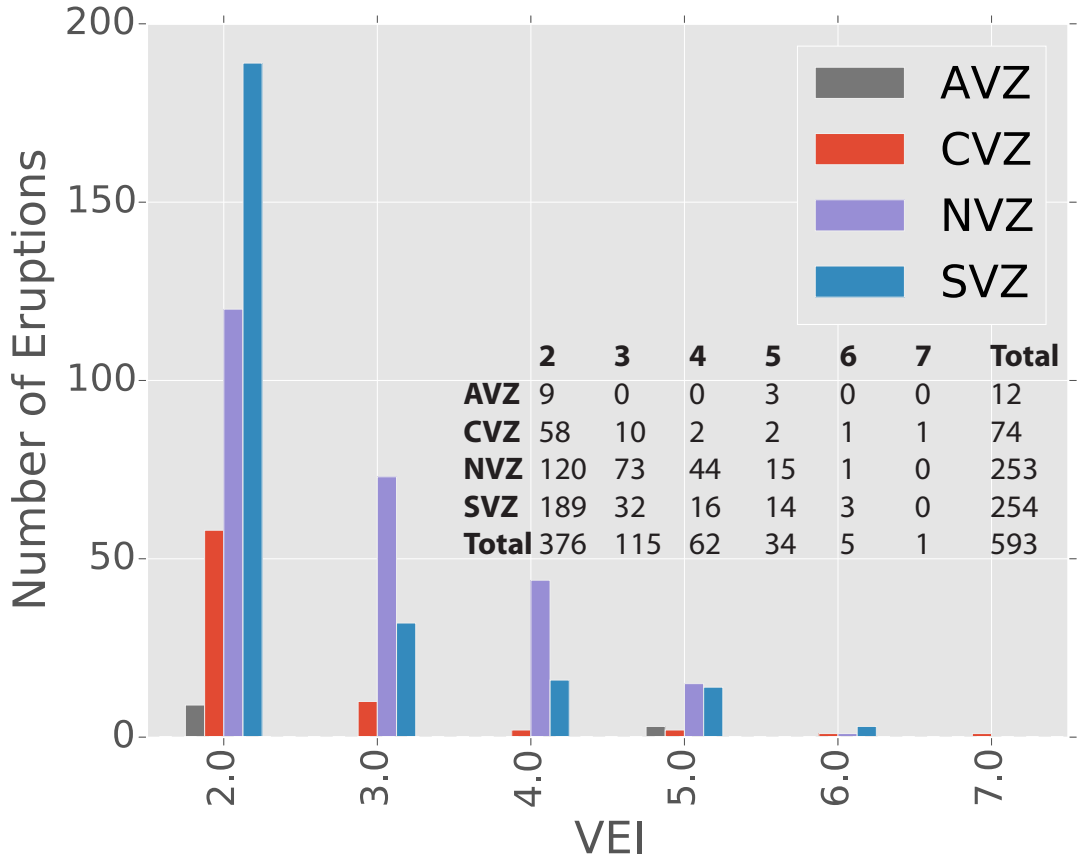

	2	3	4	5	6	7	Total
AVZ	9	0	0	3	0	0	12
CVZ	58	10	2	2	1	1	74
NVZ	120	73	44	15	1	0	253
SVZ	189	32	16	14	3	0	254
Total	376	115	62	34	5	1	593

Figure 1.5: Bar chart of Holocene eruptions in the Andes split between distinct volcanic zones. Data is from the VOTW database, using on 'Confirmed Eruptions' with a VEI of 2 or greater. Proportional to the number of volcanoes in the CVZ, the number of eruptions significantly lags behind the NVZ and SVZ.

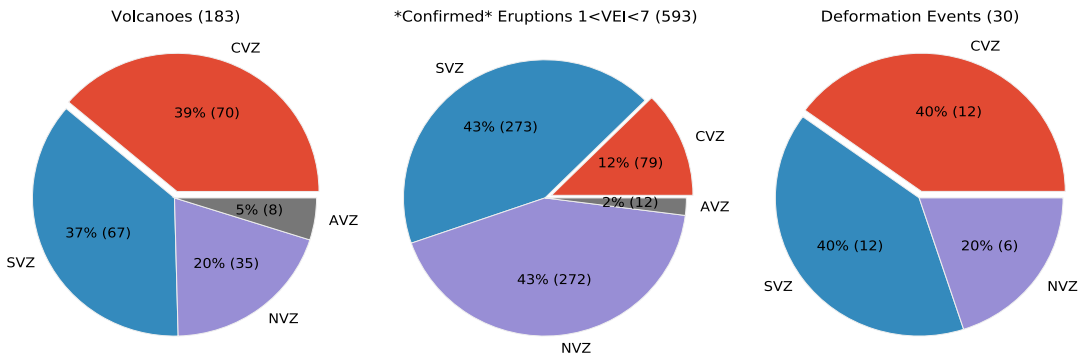

Figure 1.6: Pie charts of volcanoes, eruptions, and deformation. From left to right: Number of volcanoes included in the VOTW per volcanic zone; number of confirmed eruptions per volcanic zone; number of recorded deformation events per volcanic zone.

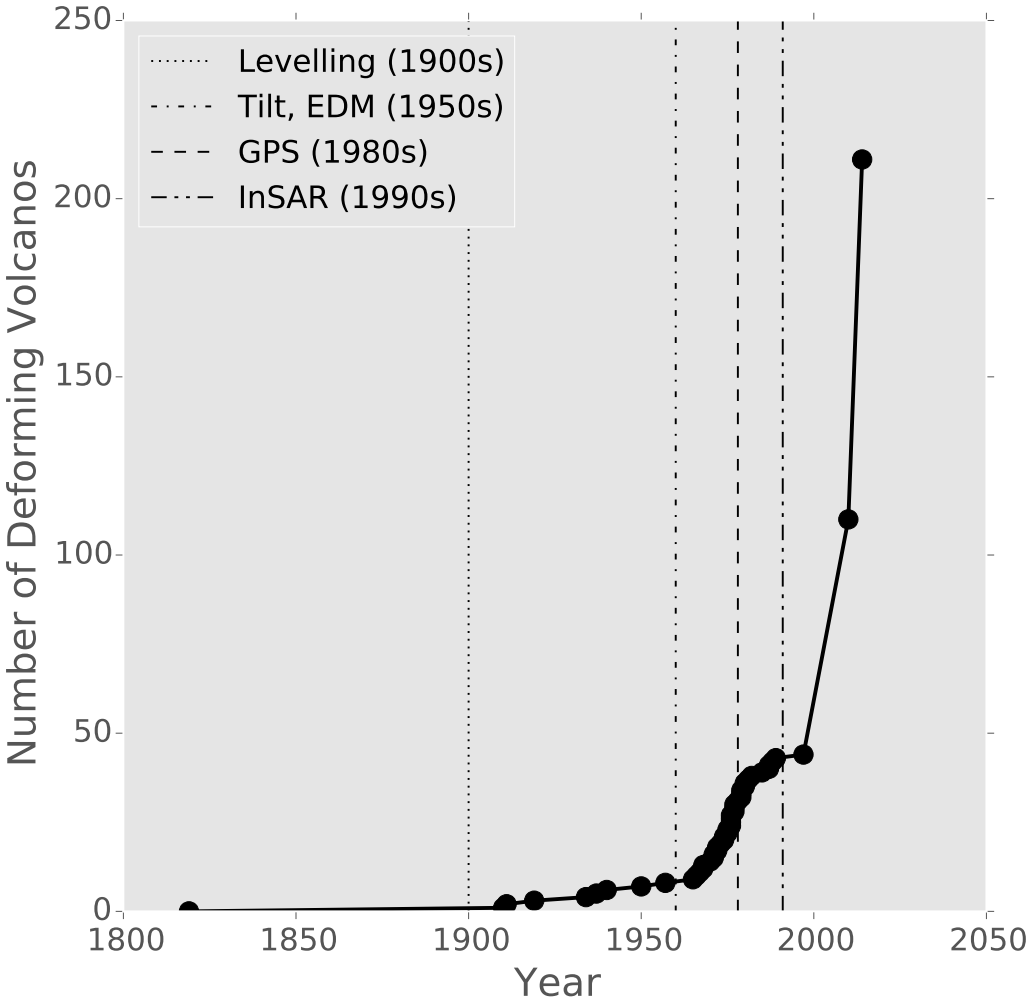

Figure 1.7: Cumulative number of volcanoes with observations of surface deformation. Vertical lines show the availability of key geodetic technologies used in monitoring.

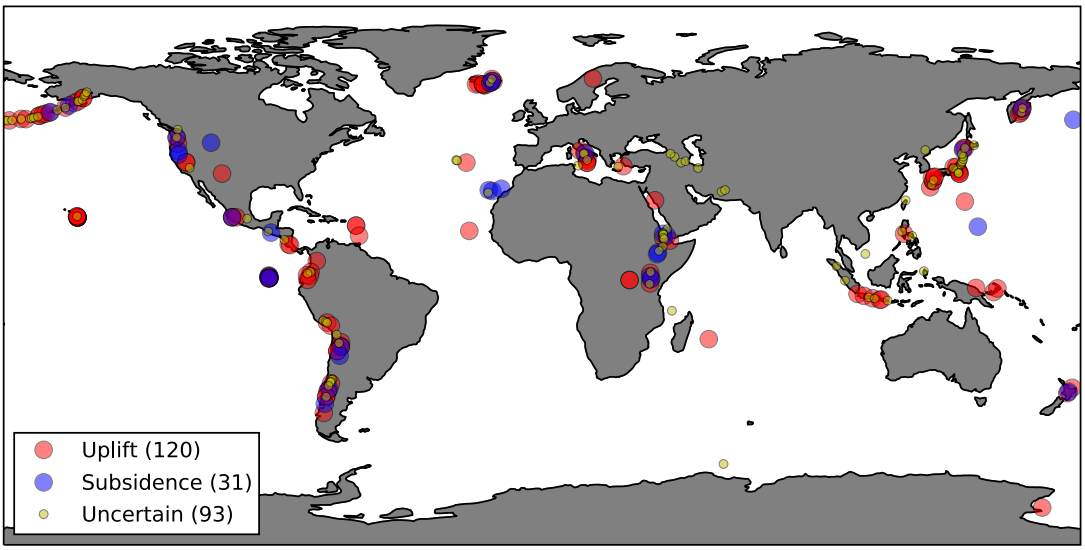

Figure 1.8: Distribution and sign of volcano deformation as of 12/2014. Note that several volcanoes are represented more than once for distinct deformation events. 'Uncertain' reflects an entry in the table for which deformation has been noted, but no quantitative measure is available.

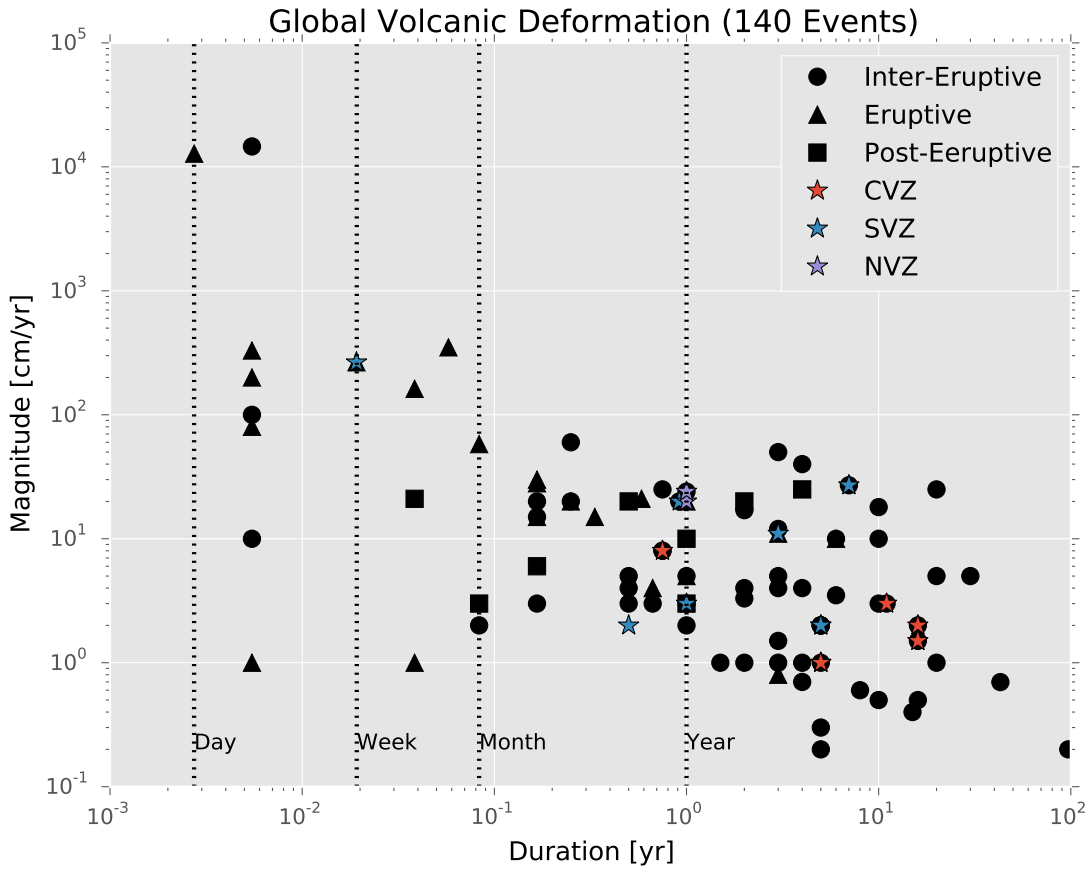

Figure 1.9: Magnitude-frequency relationship for volcanic deformation, updated since *Fournier et al.* (2010). Circles indicate deformation was observed without accompanying eruption, triangles indicate deformation was clearly associated with an eruption, and squares indicate deformation measurements were made after an eruption. Deformation episodes in the Andes are colored by volcanic zone. Caution should be taken interpreting this plot since many reports of duration can be temporally aliased. Also note that I have not distinguished causes of deformation, which are typically hypothesized as due to hydrothermal, magmatic, or compaction of surface deposits.

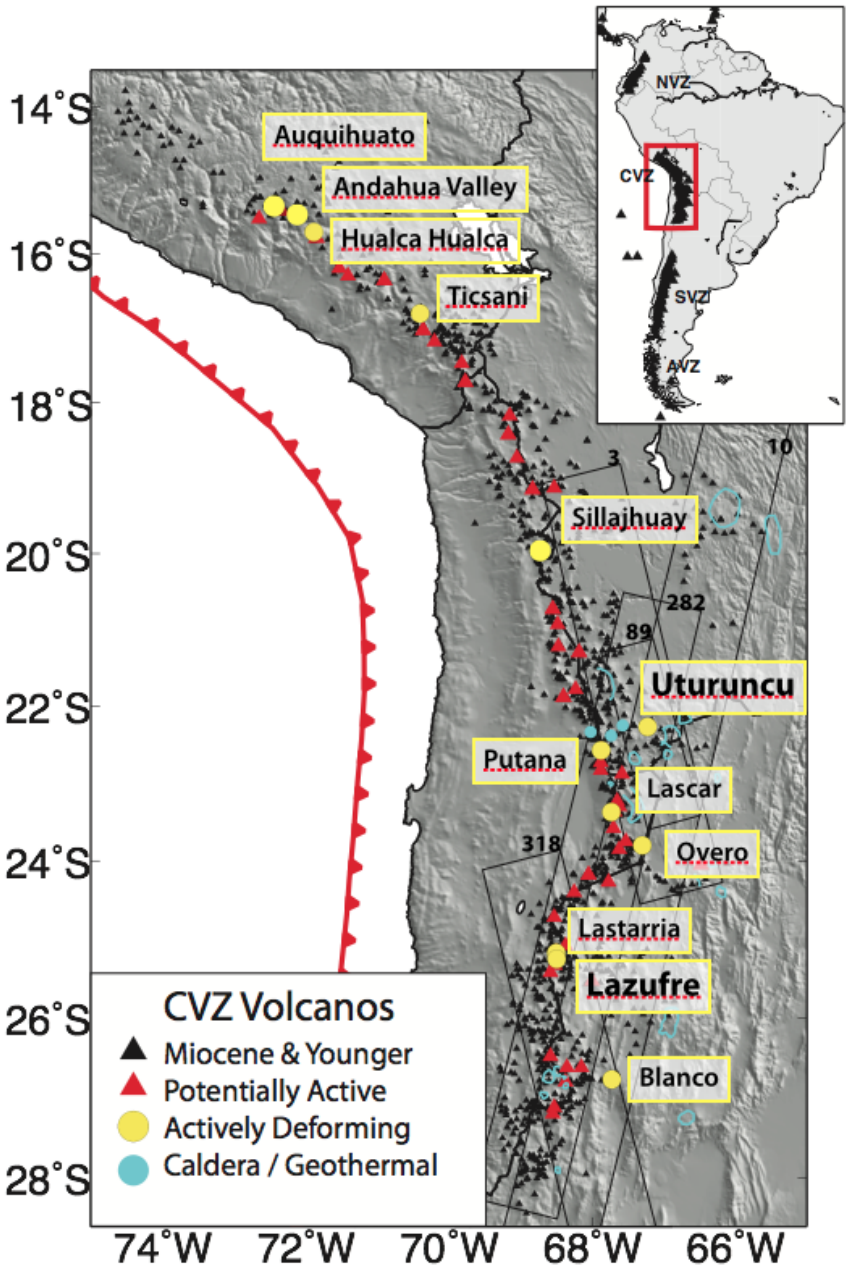

Figure 1.10: Map of volcanic activity in the Central Andes. Black triangles represent volcanic edifices (*de Silva and Francis*, 1991). Red triangles are volcanoes with Holocene activity from the Smithsonian Global Volcanism Database (*Siebert et al.*, 2011). Blue outlines are silicic calderas and geothermal zones (*Riller et al.*, 2001). Yellow circles mark locations of known volcanic deformation [this study, (*Pritchard and Simons*, 2004; *Pavez et al.*, 2006; *Ruch et al.*, 2009; *Holtkamp et al.*, 2011)]. Black rectangular outlines represent the extents of ERS and Envisat InSAR data used in Chapter 2 with track numbers in upper right corner.

Volcanic Arc	Active Volcanoes	Historical Eruptions	Eruptions/Year	Deforming Volcanoes
Northern (NVZ)	35	16	0.7	6
Central (CVZ)	69	13	0.3	12
Southern (SVZ)	63	27	1.0	12
Austral (AVZ)	8	6	0.05	0

Table 1.1: Comparison of basic characteristics of volcanic arcs of the Andes. Eruption rate is determined from set of 411 historical eruptions (Defined as 'confirmed eruptions', VEI2>2, since the year 1800) compiled from (*Venske et al.*, 2014).

CHAPTER 2

DECADAL VOLCANIC DEFORMATION IN THE CENTRAL ANDES VOLCANIC ZONE REVEALED BY INSAR TIME SERIES

2.1 Introduction

Here we present two decades of geodetic observations of volcanic deformation within the CVZ using InSAR.[1] This survey has two principal goals: First, to better understand the distribution, frequency, and geometry of deformation throughout the arc; and second, to improve individual volcano hazard assessments by determining background deformation rates. Deformation patterns have been shown to sometimes precede volcanism (e.g. *Voight et al.*, 1998), in other cases deformation ceases without eruption (e.g. *Poland*, 2010; *Moran et al.*, 2011). Therefore, in order to evaluate the implications of deformation at a particular volcano it is important to rigorously sample surface deformation in both space and time (e.g. *Dzurisin*, 2003). Furthermore, whether or not future eruptions occur, these InSAR measurements place important constraints on the volume of intruding material (e.g. *Delaney and McTigue*, 1994; *Johnson et al.*, 2000), which are of interest to the debate surrounding the emplacement and eventual fate of plutons (e.g. *Glazner et al.*, 2004; *Bachmann et al.*, 2007; *Lipman*, 2007; *Menand et al.*, 2011).

Decadal trends of volcanic deformation in the Central Andes Volcanic Zone are identified with Interferometric Synthetic Aperture Radar (InSAR) stacks and time series velocity maps covering an area $19-27°$S and $66-69°$W. We combine over 750 ERS and Envisat interferograms from 2 descending and 3 ascending

[1] A slightly modified version of this chapter is published in *Henderson and Pritchard* (2013)

tracks. These tracks cover 100,000 km^2 and span 1992 to 2011. Our analysis extends observations at Cerro Blanco, Uturuncu, and Lazufre volcanic centers and uncovers two previously undocumented deformation centers; Cerro Overo in Northern Chile, and Putana Volcano in Southwest Bolivia. Cerro Overo exhibits a transition from steady -0.4 cm/yr deflation to 0.5 cm/yr inflation over several years. Putana Volcano underwent a short-lived episode of uplift between 13 September 2009 and 31 January 2010, with a maximum uplift of 4.0 cm. Cerro Blanco continues -1.0 cm/yr deflation since 1995. Uplift at Lazufre began between 1997-2000 and has gradually accelerated to 3.5 cm/yr since 2005. Uturuncu volcano continues 1.0 cm/yr monotonic uplift since 1992, and shows evidence for a broad moat of subsidence surrounding the uplifting region. Four of the nine deformation events in the CVZ are not obviously associated with a particular volcanic edifice. Furthermore, there is significant spatial and temporal variability of these deformation events within a small geographic area.

In this chapter we present evidence that the deformation signal at Uturuncu is unique among the other deforming volcanoes in the CVZ. We first describe our method for surveying large regions of a volcanic arc with InSAR, and we report on the spatial and temporal variation in surface deformation from 1992 to 2011 for a large subregion of the CVZ ($19°$S to $27°$S). We also provide order of magnitude estimates of source parameters based on standard inverse models. The five major deformation centers discussed in this paper are shown in Figure 2.1.

2.2 InSAR Observations

We generated 757 interferograms from five different tracks, spanning 1992 through 2011 and covering over 800 km along the volcanic arc (Table 2.1). All radar scenes are acquired from C-band ERS1, ERS2, and Envisat satellites. Full details of our processing steps are covered in Appendix A, and in the following sections we briefly outline the essential methodology.

We use Radar Orbit Interferometry Package (ROI_PAC) software (*Rosen et al.*, 2004) to process interferograms, pairing individual radar scenes with maximum baselines between 200-500 m (depending on the satellite track) to minimize spatial decorrelation. We use precise ODR orbital information when available from the Delft Institute for Earth-oriented Space Research (*Scharroo and Visser*, 1998; *Doornbos and Scharroo*, 2005), otherwise we use precise PRC orbits from the German Space Agency. To account for topographic signal, we utilize Shuttle Radar Topography Mission (SRTM) data at 90 m resolution (*Farr et al.*, 2007). Many interferograms contain residual ramps resulting from the incomplete removal of orbital phase signals, which we remove by fitting a linear or quadratic surface. Interferograms are unwrapped with Statistical-cost Network-flow Algorithm for Phase Un-wrapping (SNAPHU) (*Chen and Zebker*, 2001), and downsampled to 720 m per pixel (*Rosen et al.*, 2000). Downsampling filters short wavelength signals and decreases computational requirements, which is desirable for surveying large areas for volcanic deformation signals with surface footprints greater than several kilometers. Finally, interferograms are co-registered onto a common grid in radar coordinates.

2.2.1 Sources of Noise

The dominant source of noise in single interferograms is attributed to phase delays as the radar signal propagates through the atmosphere (e.g. *Goldstein*, 1995; *Zebker et al.*, 1997). Owing to the large relief on volcanic edifices, atmospheric phase delays can sometimes be misconstrued as uplift or subsidence signals, and therefore care must be taken to separate these signals (*Delacourt et al.*, 1998).

In the CVZ, both descending and ascending interferograms regularly show correlated noise that varies with atmospheric water vapor concentrations (*Fournier et al.*, 2011). Ascending tracks, which are acquired at approximately 10pm local time in the CVZ, can have additional large ionospheric signals that are related to variability in electron density (e.g. *Gray et al.*, 2000; *Xu et al.*, 2004). Ionospheric signals are easily identified as SW-NE trending, high amplitude streaks that are roughly parallel to the Earth's magnetic field at this latitude (*Loveless et al.*, 2010; *Fournier et al.*, 2010). We note that for ascending track 318, four dates between 03/2008 and 03/2010 have strong ionospheric signals, which represents 22% of all acquisition dates for the track. In track 3, four dates between 04/2002 and 11/2009 have strong signals, representing 18% of acquisition dates (Table 2.1). While some methodologies have been proposed to mitigate ionospheric signals for L-band data (e.g. *Rosen et al.*, 2010), we choose to omit these dates from our analysis since we have sufficient scenes without ionospheric effects.

2.2.2 Interferogram Stacks

By combining many interferograms spanning different dates, temporally variable noise is partially cancelled out, improving the accuracy of deformation rate measurements (e.g. *Wright et al.*, 2004a; *Fialko*, 2006; *Biggs et al.*, 2007). Stacking of rectified interferograms is a standard way to improve signal-to-noise by a factor of $\sqrt{N}$ where N is the number of independent interferograms being combined. However, the theoretical gain in signal-to-noise assumes constant velocity deformation over the time span of N observations, and Gaussian noise with a mean of zero. Both of these assumptions are likely false for InSAR data. Nevertheless, we find that this simple approach to stacking does produce smoothly-varying spatial deformation patterns that are not correlated with topography (Figure 2.1).

2.2.3 Time Series Inversion

InSAR time series inversion is another post-processing technique that can enhance the precision of surface deformation measurements to sub-centimeter levels (*Casu et al.*, 2006; *Ferretti et al.*, 2007; *Hooper et al.*, 2011). In addition, time series analysis extracts a cumulative deformation history for each pixel in a set of interferograms. There are many versions of time series algorithms in use (e.g. *Lauknes et al.*, 2011; *Hetland et al.*, 2011), but most are based on Persistent Scatter (PS) (*Ferretti et al.*, 2001) or Small-Baseline Subset (SBAS) (*Berardino et al.*, 2002) algorithms. PS techniques are generally favorable in areas of low radar signal coherence, but given the high coherence in the CVZ we employ an SBAS-based algorithm in our inversion.

All SBAS inversion schemes assume only that velocity is constant between consecutive dates, instead of over the total elapsed time of observations. Therefore, any function may be applied as a best-fit regression to the time series output of cumulative deformation versus time, potentially improving the accuracy of ground velocity measurements. Our time series inversion algorithm closely follows procedures outlined in *Lundgren et al.* (2001) and *Berardino et al.* (2002), which have been applied successfully in several extended-area surveys (*Tizzani et al.*, 2007; *Casu et al.*, 2008).

For a combined set of unwrapped ERS and Envisat Interferograms we solve the following linear inverse problem pixel-by-pixel using singular value decomposition (SVD):

$$Bv = \delta\phi \tag{2.1}$$

Where B is the mxn design matrix for a set of m interferograms containing $n+1$ dates, and the nonzero entries of B are the timespans between consecutive dates; v is a column vector of pixel velocities for each date interval; and $\delta\phi$ is the data vector containing unweighted deformation values extracted from individual interferograms. For most pixels the system of equations is over-determined and v contains the velocities that minimize the L_2 residual.

We integrate output velocities to produce plots of cumulative deformation versus time. The deformation history can then be fit with another linear regression to produce ground velocity maps over the analyzed time period. We assume a functional form $y = mx + b$ in our regression, and consequently nonlinear rates will be obscured on this velocity map product. However, we note

that maps of the L_2 residual are useful for identifying regions that deviate from linear deformation.

2.2.4 Validation

In order to quantify uncertainties in measured surface deformation rates, previous InSAR time series studies compare results to independent datasets such as leveling data (*Pepe et al.*, 2005; *Casu et al.*, 2006), or GPS measurements (*Finnegan et al.*, 2008). Unfortunately, there are no GPS measurements in our study region that overlap in sufficient time with InSAR observations (Figure 3.3). One approach to validate time series results in the absence of ground-based measurements is to compare velocities obtained via an independent processing chain (*Casu et al.*, 2008). Since the major deformation centers in the CVZ (Uturuncu, Lazufre, and Cerro Blanco) have been observed to be monotonically inflating or deflating over the past two decades, we expect close agreement between time series best-fit velocities and average velocities derived from simple stacking. In Figure 2.2 we compare velocity maps based on these two processing techniques to demonstrate the agreement in amplitude and spatial pattern of deformation signals.

We also follow the procedure outlined by *Finnegan et al.* (2008) to compare velocities derived for the same ground pixels in overlapping descending tracks 10 and 282 covering the same time period (1995-2010). Direct comparison of pixel velocities is complicated by the fact that actual displacement values are projected into different Line Of Sight (LOS) vectors, whose incidence angles vary both between tracks and up to 9° across a single track. These discrepancies

lead to a subtle skewing of values about the 1:1 line, but the general agreement in velocities is clear. The spread of noise can be characterized following *Finnegan et al.* (2008) as a uniform distribution of velocities between -1 and 1 mm/yr and Gaussian white noise with a standard deviation of 4 mm/yr (Figure 2.2). While the dominant source of noise in interferograms is not white, this simplifying assumption gives us an approximate bound on the uncertainty in velocities derived through stacking and time series analysis.

Finnegan et al. (2008) makes the assumption that InSAR measurements are mostly vertical, but in the case of volcanic deformation signals, radial displacements can be significant. In order to isolate the contribution of geometric distortion in our validation procedure we took forward models of uplift at Uturuncu from *Pritchard and Simons* (2004) and projected the noiseless synthetic displacements into LOS for tracks 282 and t10. Plotting the agreement of the projected synthetic data results in a unique distribution about the 1:1 line. We note that for an expansion point source (*Mogi*, 1958), track 282 shows systematically higher velocities compared to track 10, whereas the stack and best-fit velocities derived from actual data show slightly higher velocities in track 10. This effect is more pronounced for the high-amplitude signal of Uturuncu, and could be due to different acquisition dates in tracks 282 and track 10. Another possible explanation is that the radial and vertical deformation vectors predicted by elastic half-space models of a spherical point source are not representative of the actual deformation source underlying Uturuncu. Consequently, more complicated source shapes or heterogeneous crustal material should be explored in future modeling studies.

2.3 Results and Discussion

The diameter of volcanic deformation signals in the CVZ ranges from 5 to 150 km, which implies a large range in source depths based on the classic model of a pressure source embedded in a homogeneous elastic crust (*Mogi*, 1958). While the assumptions of this simplified model likely violate the subsurface conditions in the hot, thick crust of the CVZ, it serves as an order of magnitude estimate of source depth and volume. Therefore, in order to provide a direct comparison of source parameters for the centers discussed in this paper and to compare values with previously published studies, we performed a Levenberg-Marquardt inversion for point expansion source parameters with our dataset. The results are summarized in Table 2.3 and show depths ranging from 1-24 km below local topography and changes in volume on the order of $0.1 - 30 \times 10^6 \mathrm{m}^3/\mathrm{yr}$.

In the following sections we present the InSAR time series results for individual volcanic centers, and we discuss possible source models that explain the observed deformation signals.

2.3.1 Uturuncu Volcano

Uturuncu Volcano (22.27°S, 67.22°W, 6008 m) is a dacitic stratovolcano in southwest Bolivia that has likely not erupted for 270 ka (*Sparks et al.*, 2008). *Pritchard and Simons* (2002) identified Uturuncu as a 70 km diameter region uplifting at a maximum rate of 1-2 cm/yr. A follow-up study in 2004 analyzed 12 interferograms between May 1992 to December 2000 to confirm constant uplift rate at

1-2 cm/yr (*Pritchard and Simons*, 2004). *Sparks et al.* (2008)confirmed the uplift continued in the same region through 2006. Recently, it has been suggested that there is evidence for a moat of subsidence surrounding uplift at Uturuncu resulting from lateral transport of melt to a rising diapir (*Fialko and Pearse*, 2012). We confirm that uplift at Uturuncu has been relatively constant through 2011, and that the moat of subsidence is a robust signal.

Our time series extends coverage of Uturuncu through 2011 in four separate tracks (descending tracks 282 and 10, ascending tracks 89 and 3) with hundreds of new interferograms. The velocity maps for each of these tracks clearly show uplift of the same spatial extent (Figure 2.3), which appears to stay constant through 2011 at a maximum rate of up to 1.1 cm/yr in radar line-of-sight (Figure 2.4). There is a hint of deceleration in recent years; however, the limited number of interferograms that use recent dates means the apparent deceleration could be due to uncanceled noise.

Moat of Subsidence

In order to constrain the full extent of 100km+ deformation signals it is essential to stitch multiple frames of InSAR data along a single track, or to use the Envisat ScanSAR wide-swath mode. While *Fialko and Pearse* (2012) include ScanSAR data over Uturuncu to extend East-West coverage, we use long tracks of InSAR data to better-constrain the North-South dimensions of subsidence around Uturuncu.

The moat of subsidence is not as symmetric as the uplift pattern, but this is potentially due to the lower amplitude of subsidence (up to -4 mm/yr), which

is on the order of estimated uncertainties in individual pixel velocities. As a result, the continuity of the broad signal is prone to disruption by regions of correlated atmospheric noise. Nevertheless, multiple profiles taken through the center of uplift at Uturuncu show that the subsiding region has a diameter of approximately 150 km (Figure 2.5), and we have confirmed that measured subsidence is not correlated with topography. Several cartoon models of physical models that can fit these observations are given in Figure 2.6.

We note that stacked Mogi sources can reproduce both the uplift and peripheral subsidence seen in descending data if the inflation source is located at 25km depth and the deflation source is located near the moho at 75km depth (Table 3). However, the assumption of elasticity is questionable at such depths. Furthermore we observe a significant offset in maximum LOS uplift of 6 ± 2 km in descending tracks 282 and 10 compared to ascending track 3 (Appendix A). The peak deformation offset reflects the ratio of horizontal to surface surface. This ratio is a function of source geometry assuming expansion sources in an elastic or maxwell viscoelastic half-space (*Fialko and Pearse*, 2012). At Uturuncu, a separation of 6 km could be due to prolate source geometry (*Fialko and Pearse*, 2012), crustal anisotropy (*Rubin*, 1992), or increasing shear modulus with depth (*Fialko et al.*, 2001a).

Laguna Colorado

A 20 km region centered on the Laguna Colorado ignimbrite (22.01°S, 67.68°W, 5000 m) appears as a heterogeneity within the moat of subsidence surrounding Uturuncu (Figure 2.1 and Figure 2.2). The time series from track 282 shows coherent subsidence at up to -4 mm/yr across a 20 km diameter region. This area

is not clearly associated with an active volcanic edifice; however, its perimeter appears associated with the Laguna Colorado deposits named in *de Silva and Francis* (1991). This deposit was studied earlier by *Baker and Francis* (1978), and *Salisbury et al.* (2011) estimate the age at 1.98 Ma with a dense rock equivalent (DRE) volume of 60 km^3. The location of enhanced subsidence within the larger moat of subsidence may indicate heterogeneous vertical or lateral motion of material towards the source of uplift.

2.3.2 Lazufre

Surface deformation at Lazufre (25.25°S, 68.49°W, 4900 m) was first described by *Pritchard and Simons* (2002) as a 70km axisymmetric 2-2.5 cm/yr uplift between the Holocene volcanoes Lastarria and Cordón del Azufre. Since then, studies have shown that the areal extent and uplift rate have been increasing in time, and likely perturbing the hydrothermal system underlying Lastarria Volcano (*Froger et al.*, 2007; *Ruch et al.*, 2008, 2009; *Ruch and Walter*, 2010). While the broad uplift at Lazufre can be well fit by an inflating sill at 10 km depth, it is difficult to separate the contributions of lateral growth of the sill, increasing pressurization, or other processes which can explain the increasing areal extent of uplift (*Anderssohn et al.*, 2009).

Whereas *Ruch et al.* (2009) performed separate analyses on ERS and Envisat data, we combine these datasets into a single inversion that extends coverage through 2011 (Figure 2.7). Surface deformation at Lazufre is comparable in spatial extent and uplift rate to Uturuncu, although it is important to note that the uplift is less symmetrical and profiles through the deformation do not show evi-

dence for a moat of subsidence. Our analysis confirms no deformation between 1995 and 1997, acceleration to cm/yr rates between 1997 and 2005, followed by uplift after 2005 at a constant rate of 3.5 cm/yr (Figure 2.8). The exact onset time of uplift at Lazufre is difficult to pin down given the absence of InSAR scenes between 26/10/1997 and 19/03/2000.

By examining the separation of uplift maxima in interferogram stacks from descending track 282 and ascending track 318, we find an offset of 4 ± 2 km (Appendix A), which is within the maximum range of predicted separation for sills shallower than 12 km in elastic host rock (*Fialko et al.*, 2001a). Both Uturuncu and Lazufre have been modeled as magmatic intrusions; however, additional geophysical datasets acquired in this region will help distinguish the subsurface conditions or temporal evolution of intrusions that lead to larger maximum uplift offsets and subsidence moats versus the deformation pattern observed at Lazufre.

2.3.3 Cerro Blanco

This caldera and rhyolitic dome complex in Northwest Argentina (26.77°S, 67.72°W, 4400 m) is called Cerro Blanco on some Argentinian maps, but referred to as Robledo in other studies (*Siebert et al.*, 2011). Recent dating of extensive rhyolitic ash deposits to the East suggest that Cerro Blanco was the site of the largest known Holocene eruption in the CVZ 4200 years BP (*FernandezTuriel et al.*, 2013).

Pritchard and Simons (2004) reported a subsidence rate of -2.5 cm/yr between 1992-1997, and a lesser rate of -1.8 cm/yr from 1996-2000. Our time series re-

sults indicate that a linear subsidence rate of -1.0 cm/yr throughout the entire period of observation 1992-2011 fits the data well (Figure 2.9). However, a faster rate would indeed be calculated using only data between 1992 and 1997. These observations are consistent with the independent analysis of the same ERS and Envisat dataset by *Brunori et al.* (2013).

The deflation has a much smaller footprint (20km diameter) compared to Uturuncu and Lazufre, and preliminary elastic modeling suggests a deflation source at 10km depth. Subsidence at calderas could be due to several mechanisms including solidification of cooling magma, and removal of hydrothermal fluids followed by compaction (e.g. *Newhall and Dzurisin*, 1988). *Pritchard and Simons* (2004) explored one dimensional magma chamber cooling models and concluded that an additional source of subsidence must be present to explain the observed subsidence. One possible explanation is the lateral migration of hydrothermal fluids from the section of crust overlaying deeper crystallizing melt.

2.3.4 Cerro Overo

Our analysis shows a previously undocumented 20 km diameter deformation pattern near Cerro Overo (23.76°S, 67.41°W, 5365 m) on the border of Chile and Argentina that shows a clear transition from -4 mm/yr subsidence to 5 mm/yr uplift between 2003 and 2005 (Figure 2.10). The similarity in deformation magnitude and spatial extent before and after 2003 are suggestive of a reversible process at the same source depth occurring over a 20 year timescale.

A map in *Gonzalez-Ferran* (1995) labels Cerro Overo near the SE terminus of

the NW trending Cordón Puntas Negras, although no individual description of Cerro Overo is given (Figure 2.11). Cordón Puntas Negras is a 70 km long collection of lava flows, domes, maars, and andesitic cones erupted throughout the Holocene (*Deruelle*, 1982). Volcan Puntas Negras (-23.73, -67.53, 5852m) lies about 10 km to the West of Cerro Overo, and has produced many post-glacial flows. Ten kilometers to the southwest is the El Laco volcanic complex (-23.80, -67.5, 5482m) known for its unique magnetite-bearing lavas (e.g. *Gonzalez-Ferran*, 1995). Field evidence at El Laco points to metasomatic alteration of volcanic rocks by circulating hot brines in the shallow crust (*Sillitoe and Burrows*, 2002). Thus, although there are no published reports of active fumarole fields or hot springs at Cerro Overo, it is possible that the subsidence and uplift are due to the draining and refilling of a distributed shallow crustal reservoir related to Cordón Puntas Negras.

Preliminary elastic modeling places the sources of inflation and deflation at approximately 10km depth (Table 2.3, Figure in Appendix A). If the deformation source is due to fluid evacuation followed by re-entry, it is possible that an earthquake caused a change in stress state large enough to reverse flow. From our time series inversion, we know subsidence at Overo occurred through 2003 and sometime between 2003 and 2005 uplift initiated. A candidate earthquake is the Mw 7.8 Tarapacá earthquake of June 13, 2005. However, the epicenter for this earthquake is approximately 450 km from Cerro Overo. Therefore it is possible the earthquake played a role in the transition from subsidence to uplift, but the large distance could require a dynamic triggering mechanism.

2.3.5 Putana

Putana Volcano (22.55°S, 67.85°W, 5890 m) is part of a 600 km^2 cone-and-flow complex with no historic eruptions but extensive fumarolic activity (e.g. *de Silva and Francis*, 1991). Fumarole measurements taken in 2007 at Putana showed emission temperatures of 82-88°C, source temperatures of 500°C, and relatively high concentrations of magmatic gases (*Tassi et al.*, 2011). f The volcano exhibited a short-lived episode of uplift sometime between 13 September 2009 and 31 January 2010. We note that if volcanic deformation occurs over scales shorter than several months it can easily be dismissed in a time series plot as an outlier related to atmospheric noise. Consequently, we did not detect deformation at Putana in our time series analysis, but rather from examining independent interferograms from track 282 (Figure 2.12).

The circular deformation pattern at Putana has a maximum uplift of 4 cm centered on the volcanic edifice, and a diameter of 5 km (Figure 2.13). The USGS PDE catalog shows no magnitude 4 or greater events within 500 km of Putana during the deformation timespan, and therefore the uplift does not seem to be triggered or accompanied by large earthquake nearby. However, a reconnaissance vertical component 1-10 Hz seismometer located 4 km northwest of the summit, from August 2009 to February 2011, showed local swarm-like activity on 3 October, 12-13 October, and 9-31 December 2009 (*Pritchard et al.*, 2014). We suspect that these swarms could be related to the observed deformation. Finally, we note that the Sol de Mañana geyser field, 20 km northeast of Putana, shows some evidence of broad uplift in several interferograms, although no persistent deformation is found via stacking or time series analysis (Figure 2.12).

Due to the small spatial footprint of deformation at Putana, the source is

likely a shallow hydrothermal reservoir and therefore a simple Mogi source linear elastic model should provide a good first-order estimate of depth (e.g. *Amelung et al.*, 2000). We calculate a best-fitting volume addition of 0.3×10^6 m^3 at 1 km depth to explain the deformation at Putana, although there is some hint that the deformation is slightly elongated to the East and West (Appendix A).

2.3.6 Selected Non-detection

Due to the downsampling of our dataset to 720 m pixels, previously observed deformation on the scale of 1-10 km^2 at Lastarria and Lascar was not resolved. Uplift at Lastarria Volcano ($25.17°$S, $68.50°$W, 5697 m) on the NW edge of Lazufre deformation was detected with high-resolution InSAR data (*Froger et al.*, 2007). The uplift had a rate of approximately 1 cm/yr above background, and was detected in Envisat data acquired between April 2003 to January 2008 (*Anderssohn et al.*, 2009; *Ruch et al.*, 2009). Despite the frequent eruptive activity at Lascar Volcano ($22.37°$S, $67.73°$W, 5592 m) (*Matthews et al.*, 1997), there have been limited detections of ground deformation, most notably co-eruptive subsidence in the crater in 1995 (*Pavez et al.*, 2006) and compaction of pyroclastic flow deposits (*Whelley et al.*, 2011) (Table 2.2).

2.4 Conclusion

We have presented results of a decadal (1992 to 2011) InSAR time series survey of the Central Andes Volcanic zone from a combination of ERS and Envisat interferograms. Such surveys of large volcanic regions are important for

identifying trends in background deformation that can inform future hazard assessments. Our analysis has uncovered deformation at two volcanic areas not thought to be deforming (Putana and Cerro Overo), and has detected unique temporal trends at known deformation centers (Uturuncu, Lazufre, and Cerro Blanco).

Interestingly, of the 9 known volcanic deformation events in the CVZ, only one is associated with an eruption, and 4 are not clearly associated with any of the 69 active volcanoes in the CVZ. Only the deforming area surrounding Uturuncu volcano shows a broad moat of subsidence, suggesting that if such a signal is characteristic of diapiric ascent, only under the Altiplano-Puna plateau are subsurface conditions currently amenable to observable active diapir formation. Overall, there is significant variation in deformation rates throughout the arc, implying a variety of detectable hydrothermal and magmatic transport mechanisms occur over 20-year time periods.

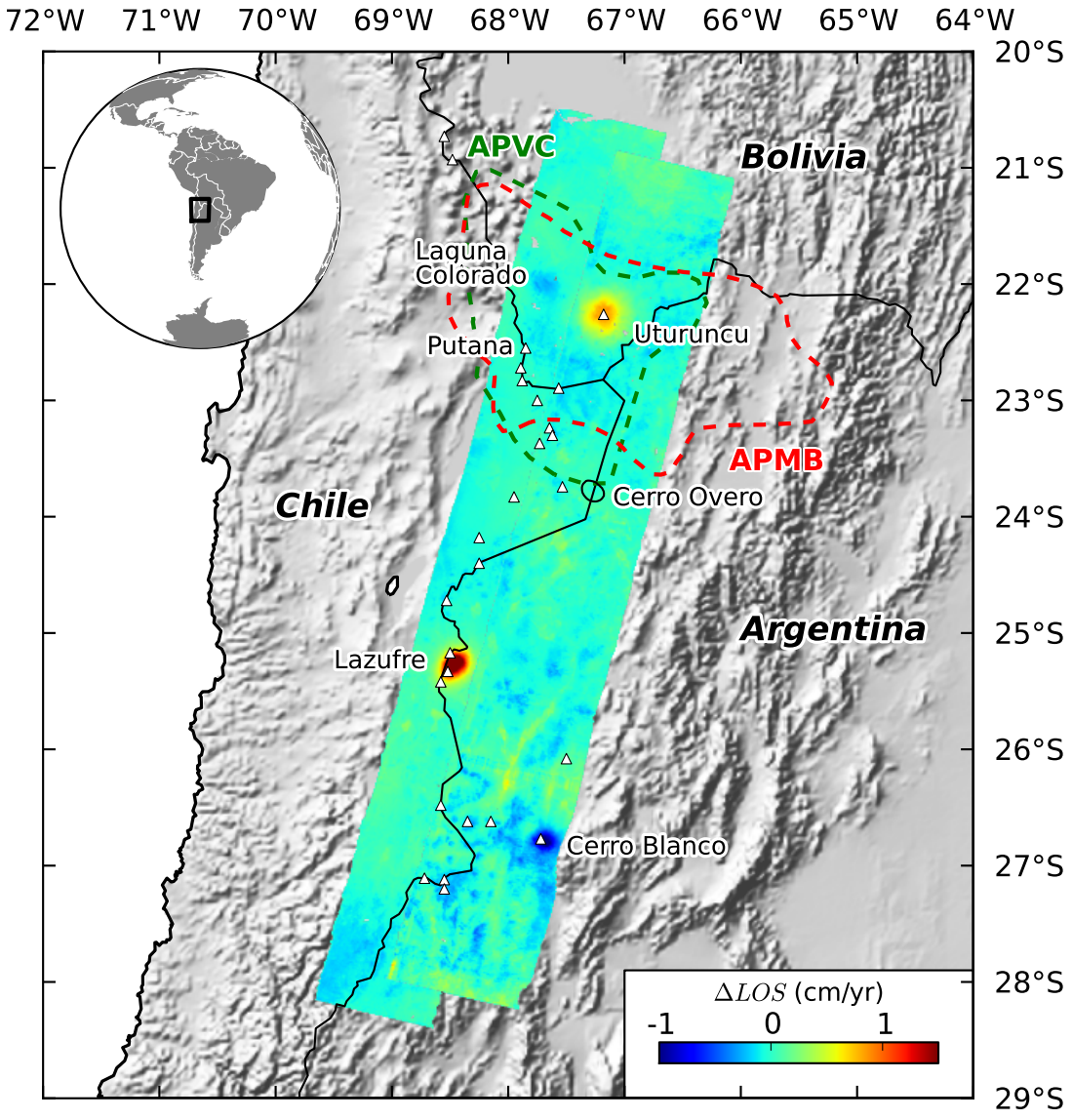

Figure 2.1: InSAR surface velocity map of CVZ. Descending tracks 282 (west) and 10 (east) cover the 5 major deformation centers in this study: Uturuncu, Lazufre, Cerro Blanco, Putana, and Cerro Overo. Red triangles are volcanoes with Holocene activity from the Smithsonian Global Volcanism Database (*Siebert et al.*, 2011). The red outline shows the maximal extent to the Altiplano-Puna Magma Body (*Zandt et al.*, 2003). The green outline approximates the extent of deposits related to the Altiplano-Puna Volcanic Complex (*de Silva*, 1989).

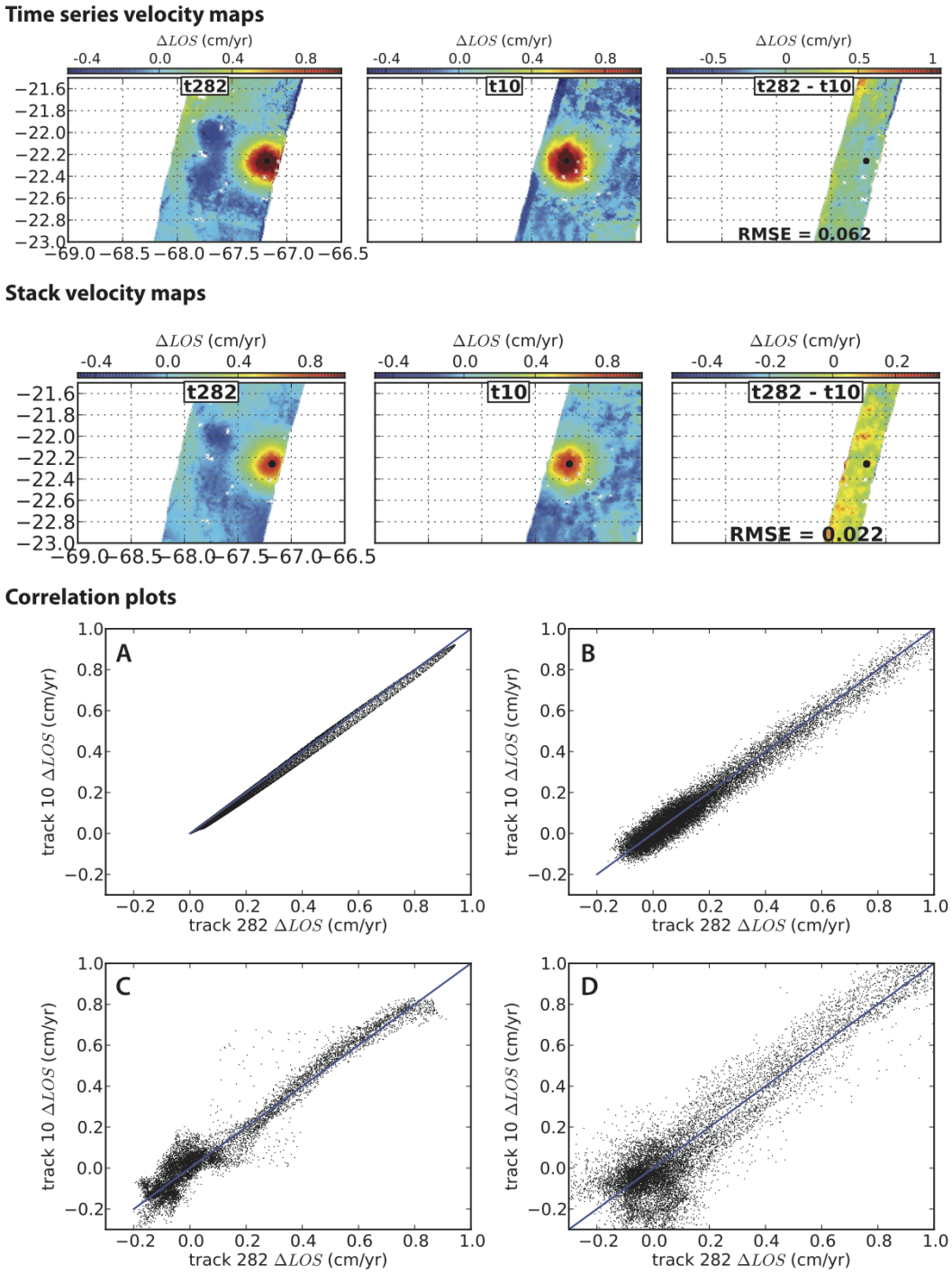

Figure 2.2: Correlation plots show agreement of pixel velocities in overlapping region of descending data: A. Best-fitting Mogi source synthetic; B. -1 to 1 mm/yr uniform distribution of velocities and Gaussian noise with standard deviation of 4 mm/yr imposed on synthetic Mogi source signal; C. Comparison of velocities obtained by stacking. D. Comparison velocities derived from time series analysis.

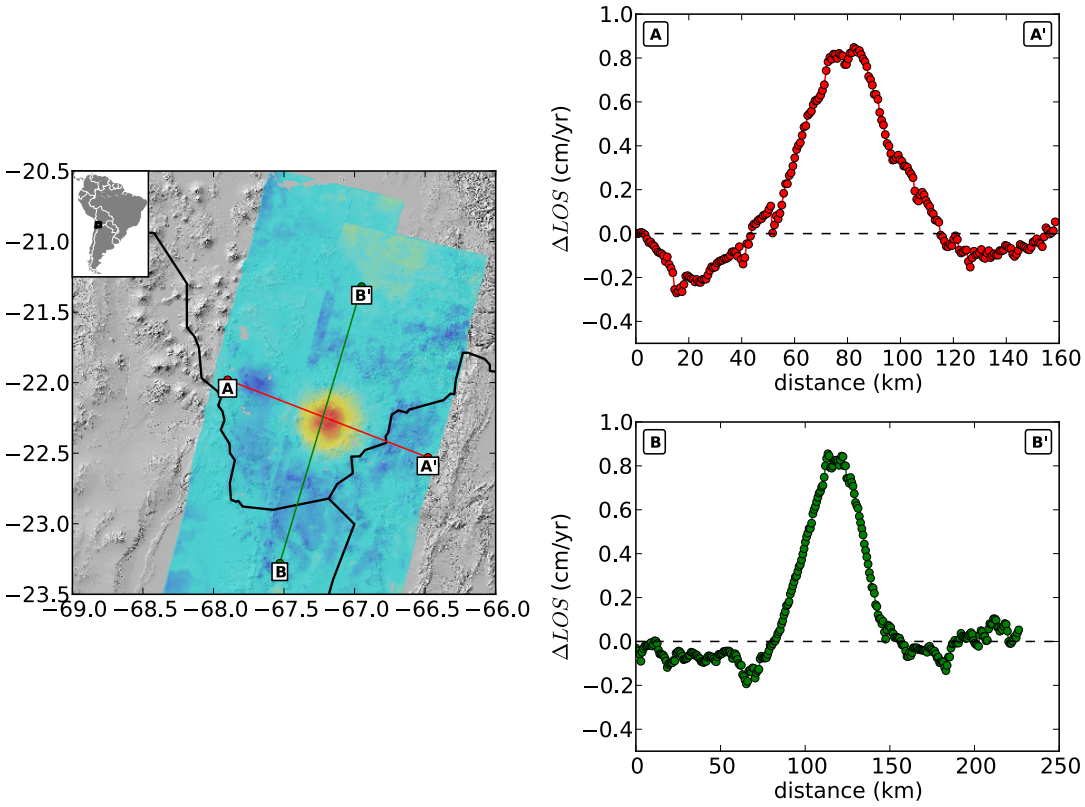

Figure 2.3: Profiles through uplift at Uturuncu volcano based on descending stacks of track 282 (left) and track 10 (right). Uplift is axis-symmetric with a diameter of approximately 70 km.

Track	Beam	# IFGs	# Dates	Dates	Orbit	Platform(s)	volcanoes
282	2	429	72	1995 - 2011	desc	ERS, Envisat	U, LC, P
10	2	107	39	1992 - 2010	desc	ERS, Envisat	U, B, O
89	6	73	20	2004 - 2010	asc	Envisat	U
3	2	15	22	1997 - 2010	asc	ERS, Envisat	U
318	2	133	19	2005 - 2010	asc	Envisat	L, B

Table 2.1: Features of the 5 tracks of InSAR data used in this analysis. For spatial extents refer to 2.1. Volcano abbreviations are the following: U=Uturuncu, LC=Laguna Colorado, P=Putana, B=Cerro Blanco, O=Cerro Overo, L=Lazufre. Deformation at Cerro Blanco is also seen in descending track 239, Laguna Colorado in track 53, and Lazufre in track 404.

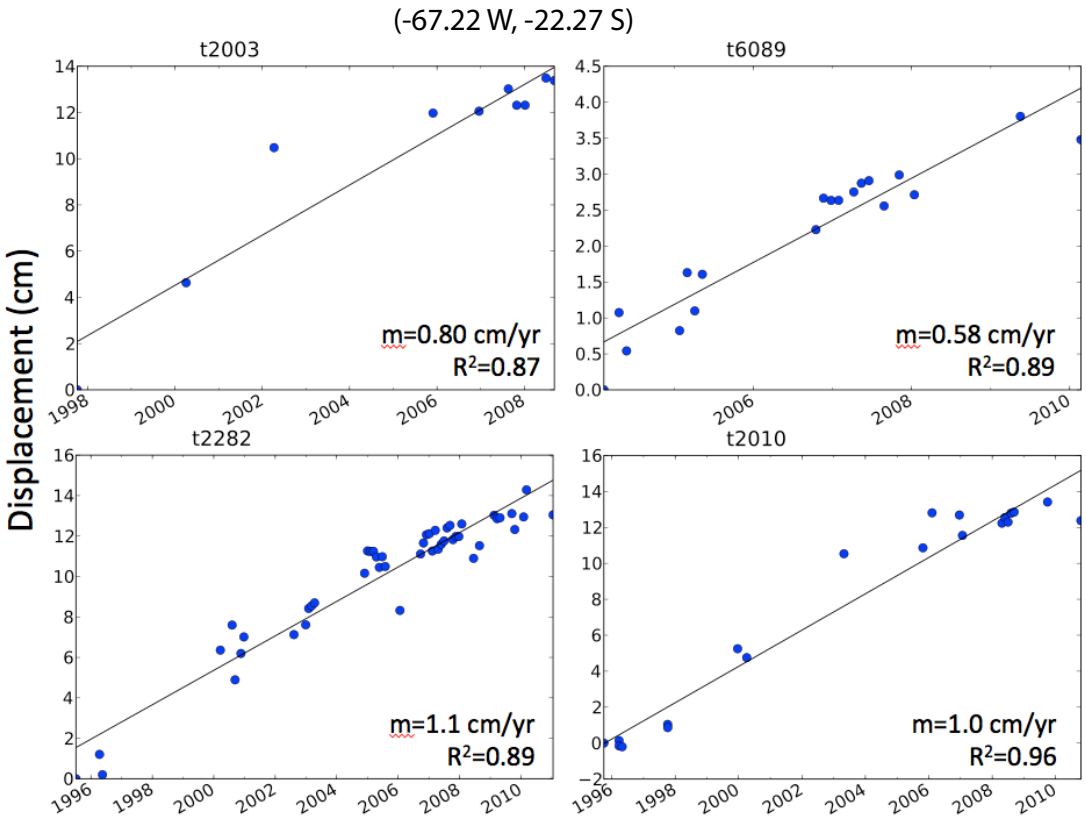

Figure 2.4: Time series deformation history for pixels near the region of maximum uplift at Uturuncu from 4 different InSAR tracks. Descending tracks 2010 and 2282 show good agreement for constant 1 cm/yr uplift since 1995. The slightly lower uplift rate in track 3 can be attributed to fewer dates and therefore greater sensitivity to the outlier in 2002. Uplift rate in track 6089 is significantly lower due to the shallower incidence angle of beam 6 compared to beam 2.

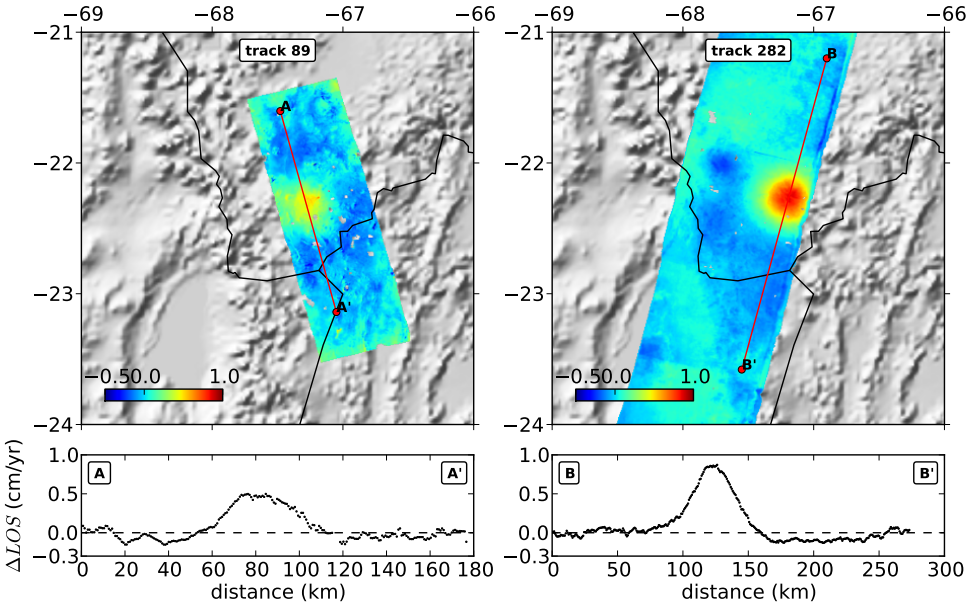

Figure 2.5: The moat of subsidence around uplift at Uturuncu is a persistent feature in both ascending and descending stacks, suggesting it is in fact a real deformation feature. Subtle linear features are associated with the edges of large subsets of interferograms used in the stack. Uplift appears to be broader and of lower magnitude in track 6089 because of a the shallow incidence angle of beam 6

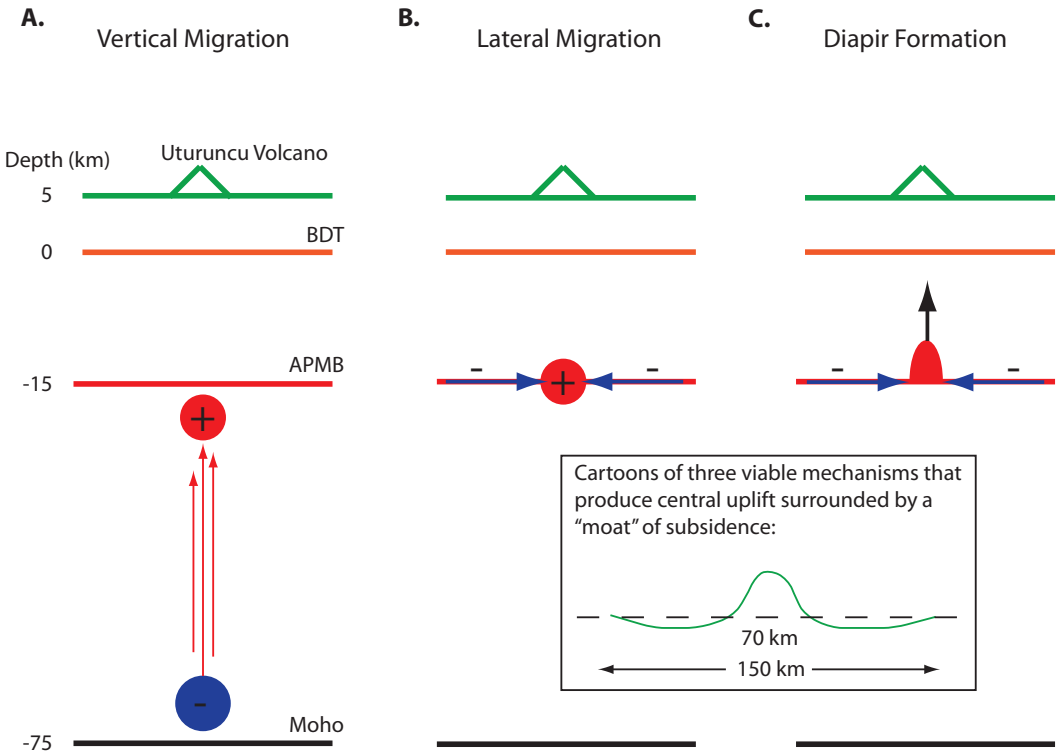

Figure 2.6: Cartoons of potential mechanisms for moat signal at Uturuncu. A) The dipole model involves vertical movement of melts from a source in the lower crust to a stalling level in the mid-crust. B) Lateral flow of melt toward a central chamber in the mid-crust (after *Fialko and Pearse* (2012)). C) Passive entrainment of APMB partial melt by a central rising diapir (after *Fialko and Pearse* (2012)).

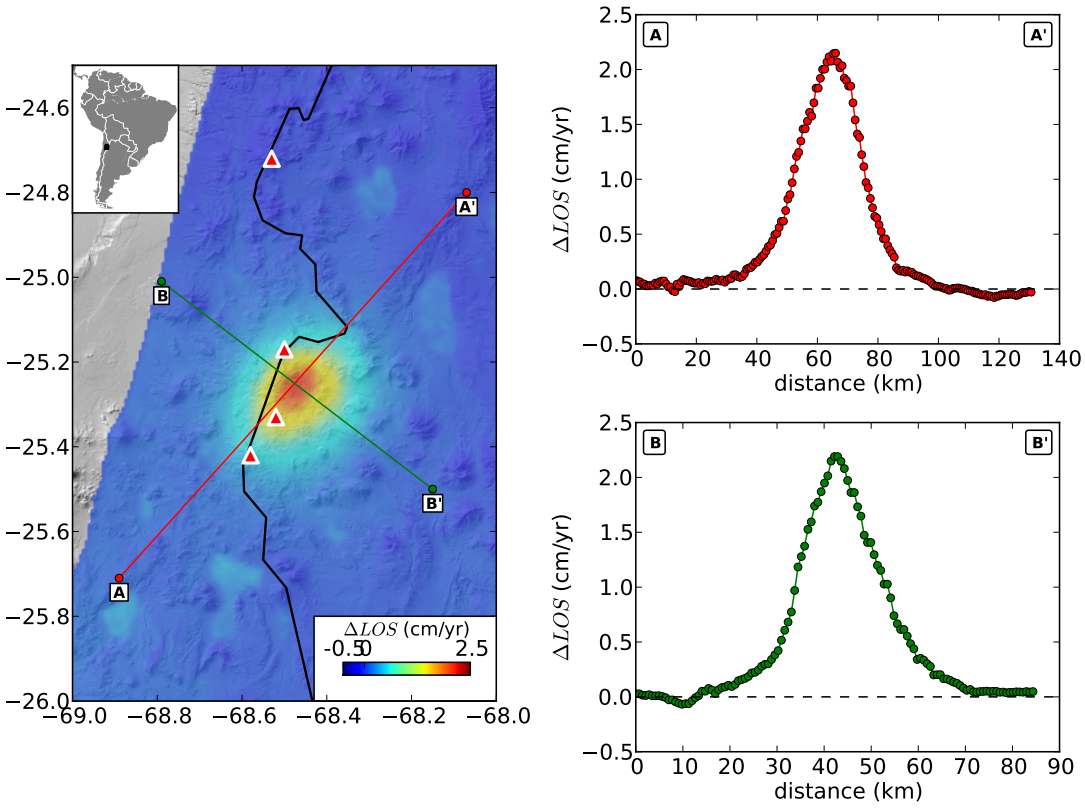

Figure 2.7: Stack of track 282 interferograms showing average LOS uplift at Lazufre between 1995 and 2011. Profiles along the approximate semi-major and semi-minor axis of the surface uplift pattern show the diameter of uplift varies between 50 to 70 km, with no evidence for a moat of subsidence.

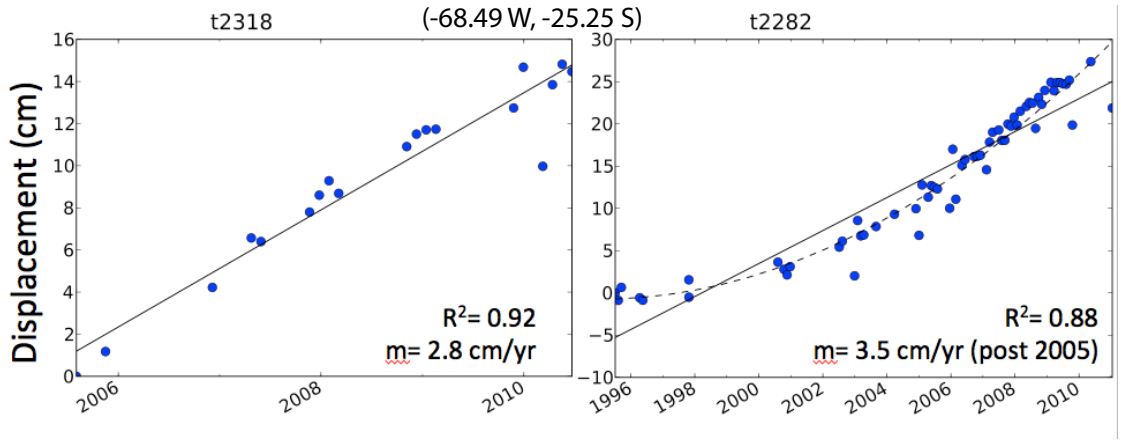

Figure 2.8: Deformation time series for pixel near the maximum uplift at Lazufre. Best-fit rates are given for data between 2005 to 2010. Ascending data (track 318) shows a lower deformation rate compared to descending data (track 282) due to different viewing geometries. Track 282 data is shown with both a linear fit and quadratic fit over the entire time period.

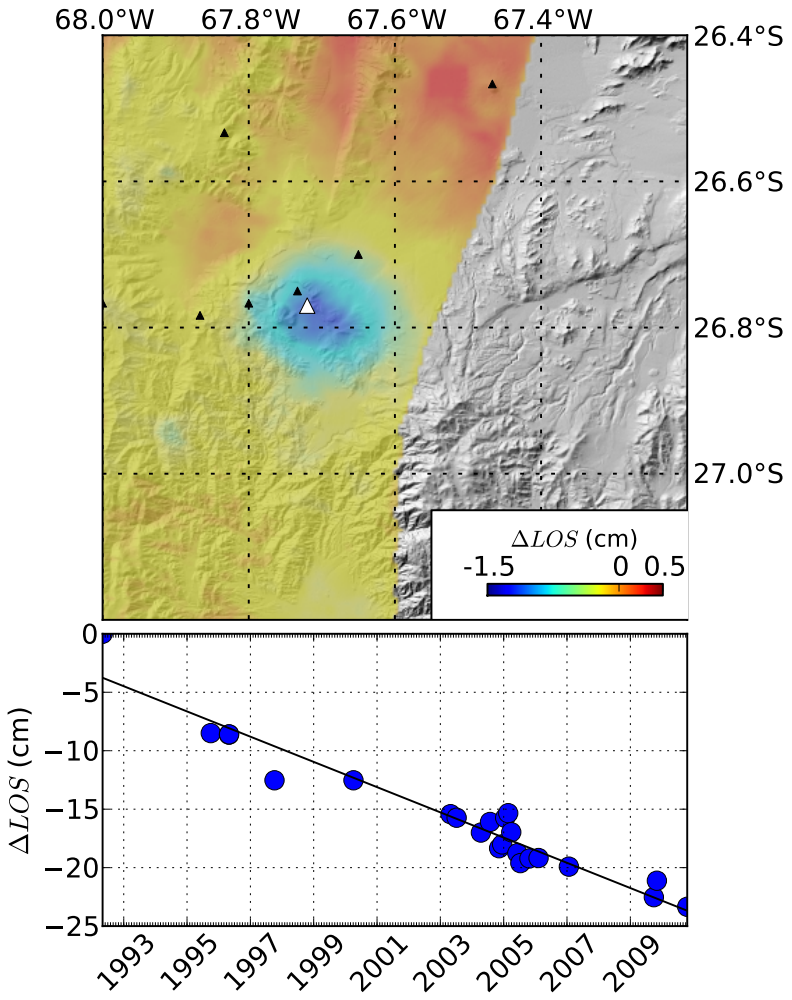

Figure 2.9: Deformation at Cerro Blanco. Top: Stack of track 10 interferograms overlain on SRTM hill shade. Black triangles represent volcanic edifices (*de Silva and Francis*, 1991). Bottom: Time series deformation history for a point (-67.72 W, -27.20 S) in the center of the subsiding zone.

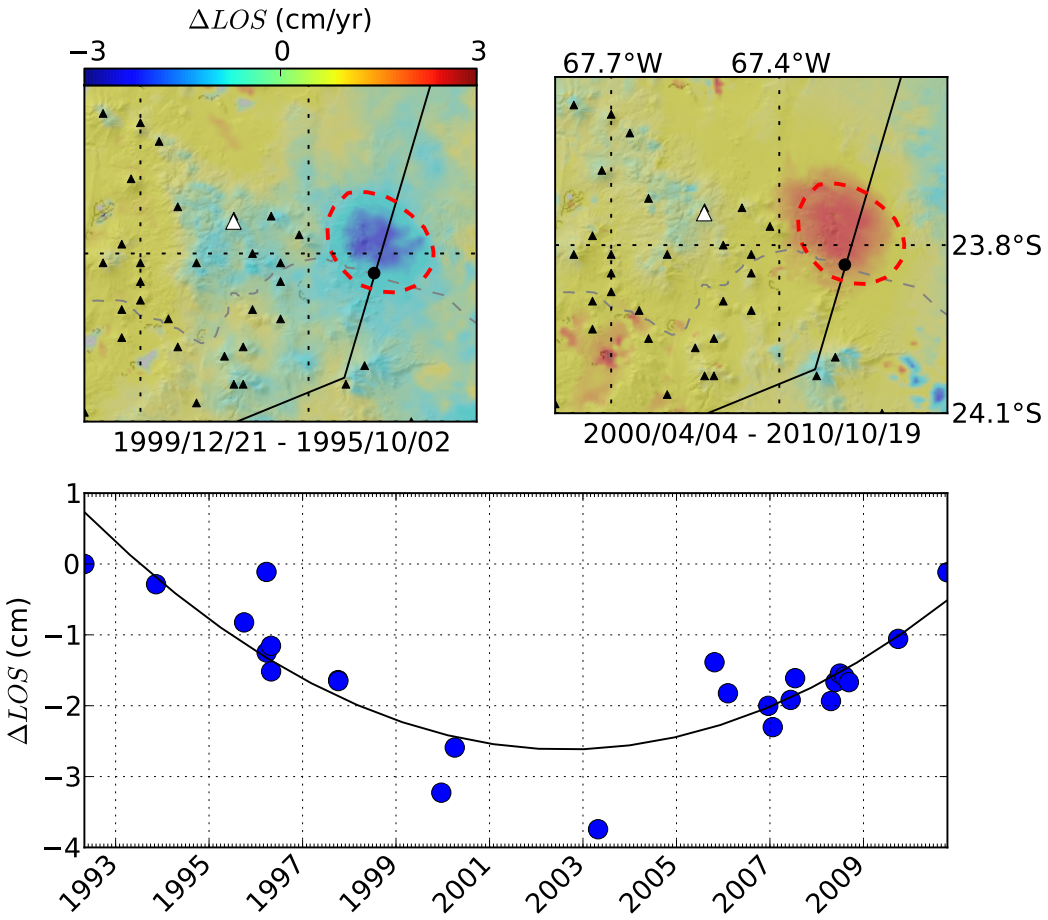

Figure 2.10: Deformation at Cerro Overo. Maps showing collocated subsidence and uplift from individual interferograms spanning different dates. Black triangles are from *de Silva and Francis* (1991), the white triangle marks the location of Cordon Puntas Negras from *Siebert et al.* (2011). The gray dotted line is a major international route between Argentina and Chile known as "Paso Sico". The diameter of the deforming region is approximated by the red dashed outline. Time series deformation history from track 10 is shown at the bottom, with -4 mm/yr average subsidence between 1992 and 2003, followed by 5 mm/yr uplift through 2010.

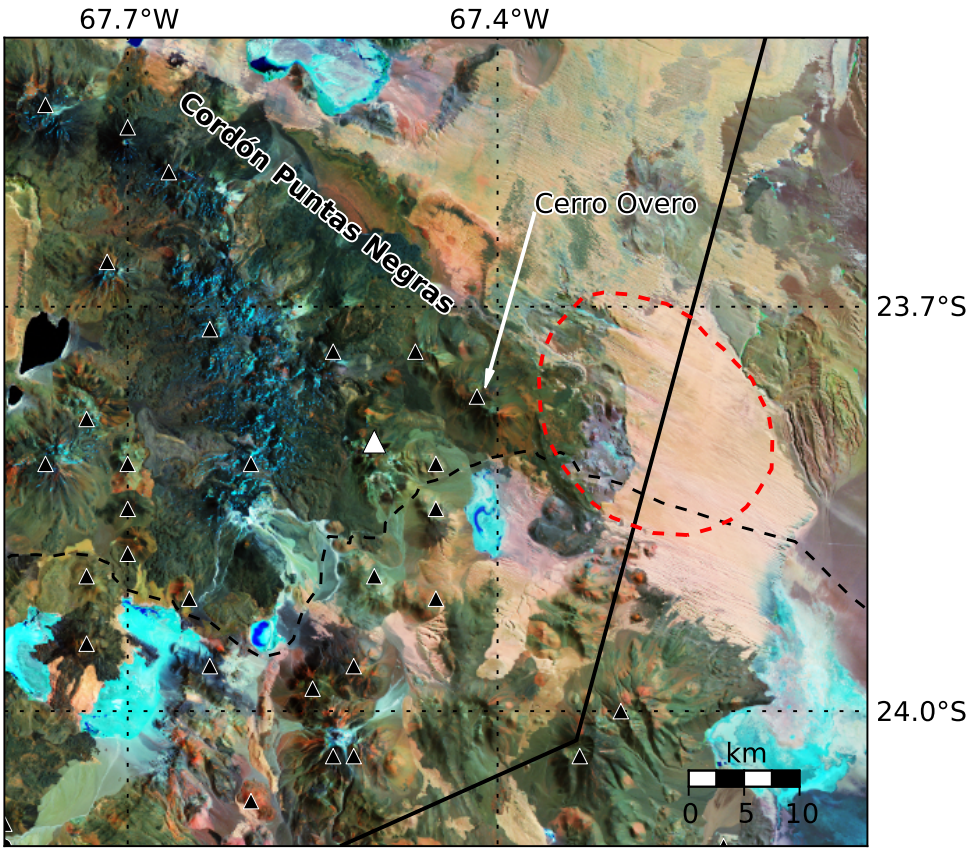

Figure 2.11: Outline of deforming region near Cerro Overo shown with a Landsat Thematic Mapper Mosaic background. The deforming zone is clearly offset to the East of the volcanic chain. Black triangles are volcanic edifices from (*de Silva and Francis*, 1991), many of them associated with the Holocene Cordon Puntas Negras volcanic chain (*Deruelle*, 1982). The location of Cerro Overo is taken from *Gonzalez-Ferran* (1995), page 185. The white triangle marks the location of the El Laco lava flows discussed in the text.

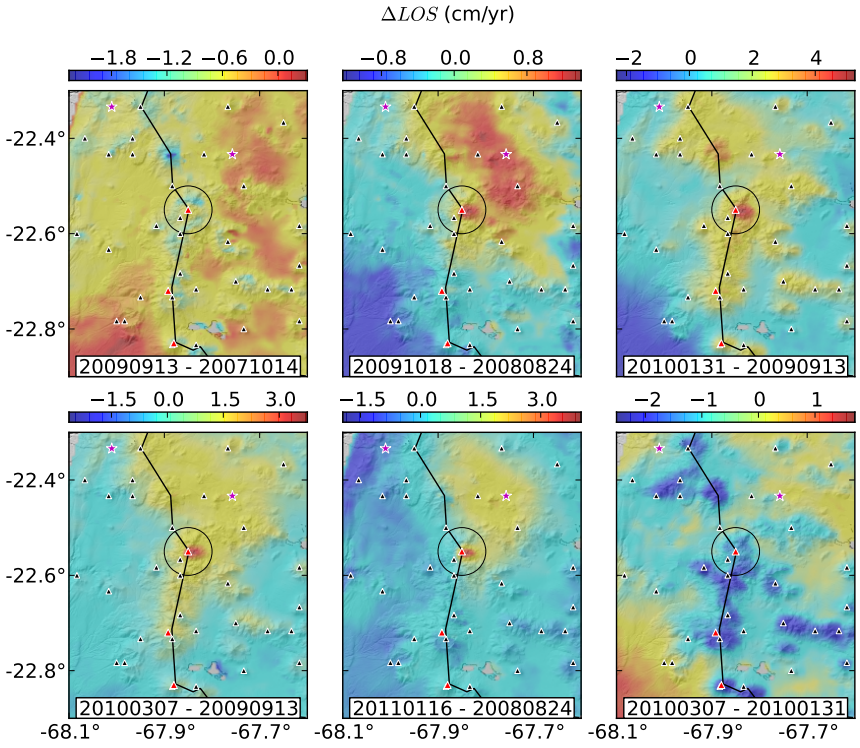

Figure 2.12: Selection of interferograms showing uplift at Putana Volcano (located within the black circular marker). Black triangles are volcanic edifices from (*de Silva and Francis*, 1991), red triangles are Holocene volcanoes from (*Siebert et al.*, 2011), and purple stars mark the location of geyser fields. The deformation is persistent on various dates and similar amplitude uplift signals are not apparent on neighboring edifices, suggesting non-atmospheric origin. Based on this collection of interferograms, and local seismic data, we ascertain the deformation was short-lived and occurred sometime between 13/9/2009 and 31/1/2010

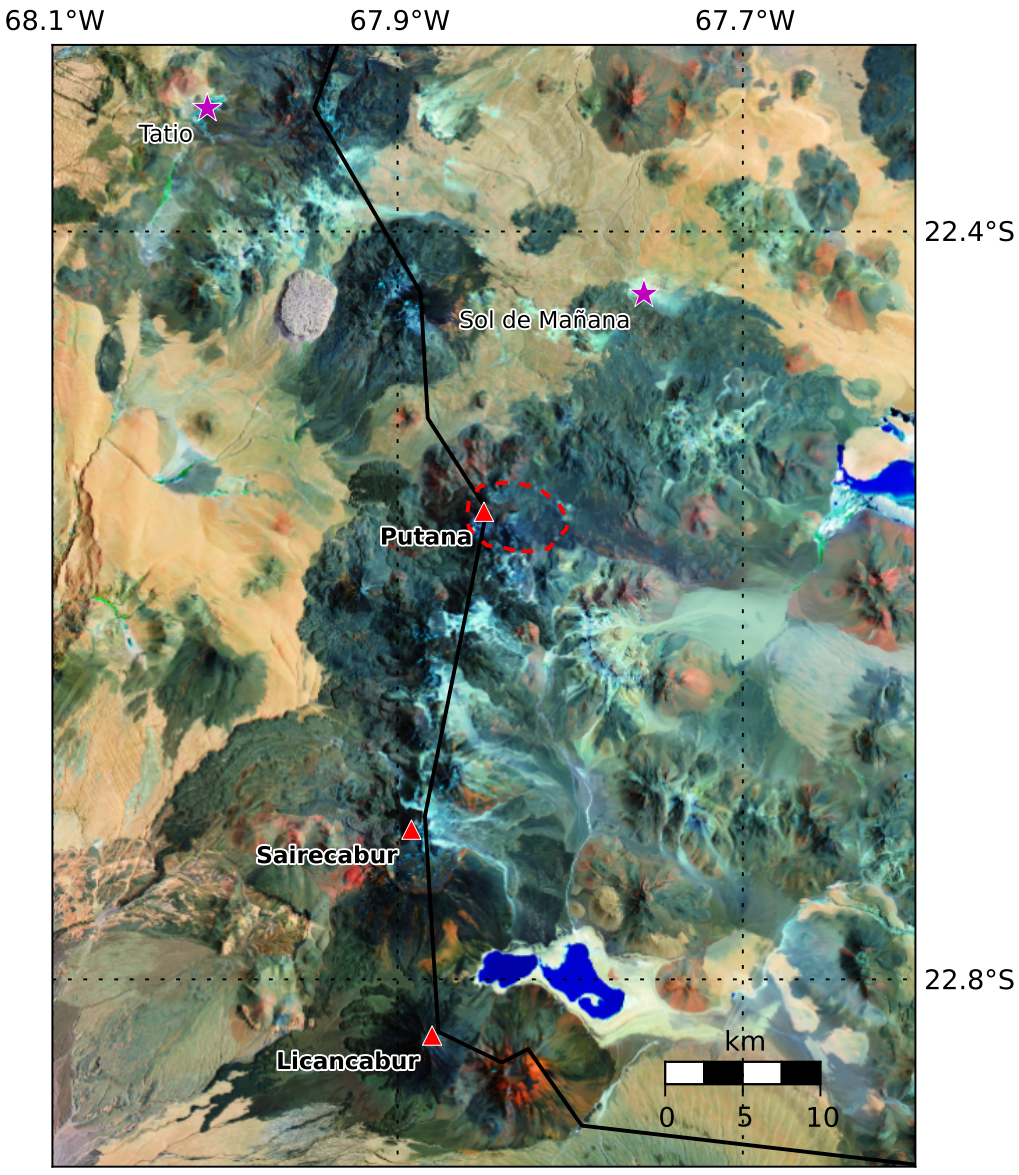

Figure 2.13: Outline of deforming region at Putana volcano shown with a Landsat Thematic Mapper Mosaic background. Red triangles are Holocene volcanoes from (*Siebert et al.*, 2011). Geyser fields are labeled by purple stars. The 5 km diameter region encircled by the red dashed line uplifted up to 4 cm between 13/09/2009 and 31/01/2010.

Volcano	V_{los} (cm/duration)	Duration	dV/dt	SA (km^2)	Center ($^\circ S, ^\circ W$)	Track
this study						
Uturuncu	1.1	1992 - 2011	constant	15,000	(22.27, 67.22)	282
Lazufre$_1$	2.0	1998 - 2005	acceleration	10,000	(25.25, 68.49)	282
Lazufre$_2$	3.5	2005 - 2011	constant	13,000	(25.25, 68.49)	282
Cerro Blanco	-1.0	1992 - 2010	constant	1,200	(26.77, 67.72)	10
Putana	4.0	09/2009 - 01/2010	impulse	120	(22.57, 67.87)	282
Cerro Overo$_1$	-0.4	1992 - 2003	constant	1,000	(23.76, 67.41)	10
Cerro Overo$_2$	0.5	2003 - 2010	constant	1,000	(23.76, 67.41)	10
previous studies						
Lastarria[a]	1.0	2003 - 2008	constant	100	(25.17, 68.50)	282
Lascar[b]	-2.0	07/1995 - 10/1995	impulse	1	(23.37, 67.73)	282
Lascar[c]	-1.0	1994 - 2009	deceleration	10	(23.37, 67.73)	282
Hualca Hualca[d]	2.0	1992 - 1997	constant	11,000	(15.71, 71.89)	454
Tiscani[e]	-23.0	06/2005 - 09/2005	impulse	600	(16.75, 70.60)	411

Table 2.2: Volcanic deformation in the CVZ compiled from this dataset and previous studies. 'LOS rate' is the maximum radar line-of-sight deformation rate over the time period listed under 'Duration'. All rates are derived from descending interferograms (see 'Track' column), which record approximately 90% of vertical displacements, and 40% of horizontal displacements. In the case of nonlinear deformation, such as Cerro Overo where constant subsidence is followed by constant uplift, we divide the deformation episode into two table lines. Surface area is calculated based on the formula for an ellipse.

[a] (*Froger et al.*, 2007)
[b] (*Pavez et al.*, 2006)
[c] (*Whelley et al.*, 2011)
[d] (*Pritchard and Simons*, 2004)
[e] (*Holtkamp et al.*, 2011)

Volcano	Center ($^\circ S, ^\circ W$)	X (km)	Y (km)	Z (km)	ΔV ($10^6 m^3/yr$)	RMSE (cm/yr)
Uturuncu	(22.27, 67.22)	-2	0	24	29	0.04
Lazufre	(25.25, 68.49)	-1	-2	13	17	0.08
Cerro Blanco	(26.77, 67.72)	1	-1	10	-6	0.07
Laguna Colorado	(22.01, 67.70)	-2	0	15	-3	0.04
Cerro Overo (uplift)[a]	(23.76, 67.30)	3	-1	13	20	0.33
Cerro Overo (sub)[b]	(23.76, 67.30)	0	-1	9	-10	0.28
Putana[c]	(22.25, 67.85)	0	-1	1	0.3	0.18

Table 2.3: Model parameters are based on an implementation of the Matlab™ $nlinfit$ routine that uses a Levenberg-Marquardt algorithm weighted by data covariance. Inversions based on descending track 282 stack unless otherwise noted. The inversion assumes poisson's ratio $\nu = 0.25$, and depths are with respect to average local topography ($\approx 4 - 5$ km).

[a] Cerro Overo uplift data from 04/04/2000 - 19/10/2010 (Envisat t10)
[b] Cerro Overo subsidence data from 02/10/1995 - 21/12/1999 (Envisat t10)
[c] Putana uplift data from full resolution interferogram 16/01/2011 - 24/08/2008 (Envisat t282)

CHAPTER 3

FEASIBILITY OF VERTICALLY STACKED MAGMATIC RESERVOIRS CAUSING SURFACE DEFORMATION AT UTURUNCU VOLCANO

3.1 Introduction

The dynamics of magmatic ascent (e.g. *Petford*, 1996; *Brown*, 2007) and the locations of ephemeral melt reservoirs in the crust (e.g. *Annen et al.*, 2006; *Menand*, 2011) are major questions in volcanology. In the Central Andes, petrological determination of lava ages and pre-eruptive conditions imply that the ascent process is not steady-state, and instead magma accumulates at specific depths for varying periods of time (e.g. *Hildreth and Moorbath*, 1988; *Kay et al.*, 2010b). Mechanical models of crustal response to magmatic intrusion constrained by geodetic and other measurements can help determine intrusion depths and timescales by probing magmatic processes as they occur (e.g. *Dzurisin*, 2000). Here we investigate a model of crustal response to vertical transport of magma between coupled reservoirs in lower and middle crust, referred to as a ”magmatic dipole”. We define the ”source” reservoir as a deflating reservoir in the lower crust and the ”sink” reservoir as the inflating reservoir at shallower depth. This model is constrained by two decades of spatial and temporal observations of surface displacements at Uturuncu Volcano in Southwest Bolivia (-67.18 °W, -22.26 °S, 6008m), but it offers insight into magmatic ascent in general.

Uturuncu is a Pleistocene stratovolcano situated in the high elevation Altiplano-Puna Plateau (e.g. *Sparks et al.*, 2008). The uplift footprint at Uturuncu has an exceptionally broad 35 km radius and has been steady at 1-10 mm/yr for nearly two decades (Figure 3.1). In order to reproduce the broad

extent of surface displacements, standard models of crustal deformation require pressurization occurring at greater than 15 km depth (*Pritchard and Simons*, 2004). However, recent Interferometric Synthetic Aperture Radar (InSAR) studies combining data from 05/1992 to 01/2011 have demonstrated that the uplift is surrounded by an approximately concentric ring of 1-4 mm/yr subsidence out to 75 km (*Fialko and Pearse*, 2012; *Henderson and Pritchard*, 2013). In an effort to explain this unique "sombrero" pattern (axis-symmetric uplift surrounded by subsidence), *Fialko and Pearse* (2012) explored a magmatic dipole model, but ultimately favored a model of diapiric ascent occurring in the middle crust. We present arguments in this paper that suggest the dipole model is physically plausible at Uturuncu and deserves further consideration.

The dipole model at Uturuncu is consistent with a lower crustal reservoir of basalt-to-andesite melt associated with 'MASH zone' processes (*Hildreth and Moorbath*, 1988), and a middle crustal reservoir where the melt undergoes evolution from andesite to dacite composition. Petrological analysis of Uturuncu dacite lavas indicate mineral assemblages and melt inclusions that are consistent with parental andesitic magma at mid-crustal P-T conditions (*Sparks et al.*, 2008; *Muir et al.*, 2014b). Geophysical evidence for reservoirs at these depths includes an extensive seismically-imaged ultra low velocity zone at 19 km depth interpreted as a 1 km thick sill of partial melt known as the Altiplano-Puna Magma Body (APMB) (*Chmielowski et al.*, 1999), and the Moho imaged at 70 km depth (*Yuan et al.*, 2000) (Figure 3.2). Note that all depths in this paper will be with respect to average surface elevation, which in the vicinity of Uturuncu is approximately 4.9 km. Finally, the geological record in this region indicates that vast volumes of eruptible magma have accumulated here in the past. Indeed, Uturuncu is centrally located within a dense concentration of Late Miocene

calderas and over 10,000 km^3 of silicic ignimbrites known as the Altiplano-Puna Volcanic Complex (APVC) (e.g. *de Silva*, 1989; *Salisbury et al.*, 2011). It is important to point out however that the current deformation footprint at Uturuncu does not appear spatially correlated with any APVC caldera.

Considering the evidence for mid-crustal melt, observed deformation at Uturuncu was previously hypothesized to be caused by magmatic intrusion into or out of the APMB (e.g. *Pritchard and Simons*, 2004; *Hickey et al.*, 2013). However, these studies were undertaken prior to the discovery of co-located subsidence and therefore considered uplift only. Additionally, an updated seismic velocity model using both receiver functions and ambient noise tomography has significantly altered the APMB geometry to a thickened low velocity ($V_s < 2.9$ km/s) zone ranging between 5 to 25 km depth (*Ward et al.*, 2014). This finding calls into question the thin sill-like nature of the APMB - a geometry which is relied on by the diapir model of *Fialko and Pearse* (2012). Furthermore, a recent study by *Walter and Motagh* (2014) describes a 'fracture girdle' surrounding Uturuncu that is consistent with depressurization at APMB-depths (and consequently subsidence at the surface) over longer timescales. Finally, continuous GPS data presented in this study indicate surface uplift occurring at a nonlinear and reduced rate since 04/2010 compared to earlier InSAR measurements. Importantly, abrupt changes in uplift rate are easy to miss due to temporal aliasing in InSAR data, and if real, may be at odds with the steady-state process of buoyant en-masse ascent.

In the following sections we present new InSAR and GPS observations at Uturuncu. We also address following questions related to the magmatic dipole model:

- For the timescale of observation, are elastic models valid for deep crustal reservoirs?
- Assuming mass balance between the dipole reservoirs, what volume discrepancies are expected?
- What is the influence of 1D and 3D crustal heterogeneity on model predictions?
- What is the the most likely transport mechanism of magma between reservoirs?

In order to address these questions we explore a variety of inverse models, and we implement a finite element model to investigate the effects of 3D heterogeneity and viscoelastic material properties at depth.

3.2 Geodetic observations

3.2.1 InSAR

Henderson and Pritchard (2013) and *Fialko and Pearse* (2012) present independent analyses of all available C-band InSAR data for Uturuncu from the ERS and Envisat satellites, spanning 05/1992 to 01/2011. Observations from other SAR satellites (ALOS, Radarsat-2, TerraSAR-X, and COSMOSky-Med) operating after 2010 either do not have sufficient acquisitions or have not yet been able to resolve deformation at Uturuncu. Between 10/2010 and 04/2012, the Envisat satellite operated in a 'drifting orbit' phase until it stopped working. Consequently, few interferograms could be created after 10/2010. Models in this

paper are therefore compared against stacked InSAR data from two ascending tracks (89 and 3), and two descending tracks (282 and 10). This dataset provides a map of average surface ground velocities at $\approx 1\mathrm{km}^2$ resolution with estimated uncertainties of ± 4 mm/yr (*Henderson and Pritchard*, 2013). Each velocity measurement is in the radar line-of-sight, which is sensitive to predominantly vertical, but also horizontal ground motions (Table 3.1).

Decomposing InSAR line of sight measurements into three cartesian displacement vectors can help distinguish between reservoir geometries in the subsurface (*Dieterich and Decker*, 1975). The vertical or radial displacement profile alone is insufficient to identify reservoir geometry because the aspect ratio and depth of ellipsoidal sources can be varied such that profiles are indistinguishable, given typical noise levels in geodetic data (*Fialko et al.*, 2001a). We therefore attempted to decompose the four different line-of-sight observations of deformation at Uturuncu into three (east-west, north-south, and vertical) components of deformation following the procedure in *Wright et al.* (2004b). However, due to the near-polar orbits of SAR satellites, north-south deformation is poorly constrained. Multiple Aperture Interferometry (MAI) (*Bechor and Zebker*, 2006) or pixel offset tracking (*Fialko et al.*, 2001b) can constrain the north-south displacements only if displacements are $>1/20$ of a pixel. These techniques are not currently viable for Uturuncu where cumulative displacement since 1992 is < 20 cm. However, by assuming that surface displacements are radially symmetric we are able to extract a representative profile along an east-west transect (where north-south displacements are assumed to be zero). We believe this assumption is valid based on the fact that the spatial pattern of deformation appears axially symmetric in four different viewing geometries. Estimates of how line-of-sight uncertainties get mapped into uncertainties for each component of deformation

are reported in (Table 3.1). For the four viewing geometries at Uturuncu, ± 1 mm RMSE in line-of-sight displacement translates to a very large uncertainty in the north-south displacement vector of ± 20 mm.

Figure 3.5 shows a profile of vertical and radial displacements constrained in the region where all four InSAR tracks overlap. We note that the peak eastern radial displacement 3.5 mm/yr and peak vertical displacement is 9.1 mm/yr, corresponding to a ratio of $u_r/u_z = 0.38$. Remarkably, this calculation does not assume source properties, but is in perfect agreement with the analytic solution for a Mogi source ($u_r/u_z = 0.38$) that is invariant with source depth. However, the radial displacements show asymmetry to the west, with a peak of -2.8 mm/yr ($u_r/u_z = 0.30$). Both of these values are less than 0.5, the minimum expected for prolate reservoir geometry, which has been invoked in previous studies (*Fialko and Pearse*, 2012; *Hickey et al.*, 2013).

3.2.2 Continuous GPS

We installed three continuous GPS stations in April 2010 named UTUR, COLO, and QUET to help constrain the temporal deformation at Uturuncu (Table 3.2). Sufficient time has now elapsed to derive ground velocities from the time series data for UTUR and COLO, but QUET was vandalized after just one year. Gipsy/Oasis software from JPL was used to process the data. JPL's fiducial-free orbits (not firmly constrained to a reference frame) were used and daily solutions were then transformed into the International Terrestrial Reference Frame 2008 (ITRF08). Velocities relative to the motion of the South America plate as estimated by the REVEL model (*Sella*, 2002). Timeseries data was also processed

relative to the COLO station, where we anticipate vertical component subsidence of -2 mm/yr based on InSAR analysis between 1992 and 2011 (*Henderson and Pritchard*, 2013).

While the horizontal velocity vectors match the regional interseismic velocity field, vertical displacements are negligible (3.1 ± 2 mm/yr) at the UTUR station near the Uturuncu summit (Figure 3.6). If the uplift rate inferred from InSAR data were holding constant, we anticipate 7 mm/yr uplift at this station since it is offset several kilometers from the uplift maximum. Seasonal signals in the vertical uplift contribute to the standard deviation of the velocity fit. These signals appear on most regional stations and therefore appear to be related to long wavelength seasonal loading of the Amazon Basin (*Davis*, 2004).

The lack of observed deformation may provide a test to the hypothesis in *Jay et al.* (2012), which suggests that enhanced levels of seismicity at Uturuncu (3 local events per day from 04/2009 to 04/2010) is attributable to ongoing inflation imposing stress on upper crustal faults. If inflation has abruptly dropped to undetectable levels, seismic activity is also expected to decrease since 04/2010.

3.3 Homogeneous Halfspace Inverse Models

We use two inversion strategies to systematically estimate the depth and volume of dual point reservoirs (*Mogi*, 1958), discussed in detail below. Both methods require a initial guess for reservoir parameters (depth, volume change, map position), and are susceptible to local minima. Therefore, we test a variety of initial conditions and data resampling to determine a range of feasible source parameters. Both models assume the crust is a Poissonian elastic half-space.

3.3.1 Least Squares Inversion

We use stacks of interferograms from track 282 and 10, which contain over 400 and 100 individual interferograms respectively. Applying the inversion strategy described in (*Fournier et al.*, 2010), which utilizes a Levenberg-Marquardt non-linear least squares algorithm, we estimate an inflation source at $25 < Z < 35$ km depth with $0.02 < \Delta V < 0.06$ km^3/yr and a deflation source at $55 < Z < 80$ km depth with $0.05 < \Delta V < 1.6$ km^3/yr. The map position of the best-fit source (-67.22 °W, -22.27 °S) is shifted approximately 5 km to the southwest relative to the summit of Uturuncu (-67.18 °W,-22.26 °S). We emphasize that a fixed map position of the sources is not enforced, yet results indicate the sources are vertically-aligned to within 5km. Figure 3.8 shows both a map view and profile view comparing descending data with a best-fit model prediction.

3.3.2 Neighborhood Algorithm Inversion

In an attempt to place further bounds on inverted parameters we also employed the Neighborhood Algorithm, a nonlinear inversion scheme designed for multi-parametric geophysical inverse problems (*Sambridge*, 1999). For comparison with the previously discussed inversion strategy, we use the same descending data and find that results are in general agreement: an inflation source with epicenter=(-67.235, -22.277), depth=35.8 km, dV=0.059 km^3, and a deflation source with epicenter=(-67.204, -22.293), depth=52.2 km, dV=0.087 km^3. Comparison of model results with data is shown in Figure 3.9, and the range of model parameters searched is shown in Figure 3.10. It is immediately apparent that for the deflation source in the lower crust most parameters have broad

minimum and are therefore not well constrained. The reservoir centers may be offset by up to 10 km, and low-residual models exist for a source reservoir in the range of 50-70 km depth. Ascending InSAR data over Uturuncu is less abundant than descending data, but additional line-of-sight observations changes the inversion result for source parameters. Results obtained by equally weighting all four stacks result in residuals of the same magnitude, but significantly different source parameters: The surface coordinates of the inflation source are identical, but the depth is 3.4 km shallower at 32.4 km. The depth to the subsidence source is deeper at 60.0 km.

3.3.3 Summary of homogeneous models

Inversions for multiple sources in a half-space must be interpreted with caution since the presence of a second source violates the assumption of homogeneity. *Pascal et al.* (2014) quantified the conditions under which multiple source inversions are valid by numerically modeling a suite of dual reservoir configurations. They report that as long as the source separation is 8 times the largest source radius, inversion results are not significantly biased. Thus, there are three main criteria for evaluating the validity of the dipole reservoir parameters: One, the reservoir depth should be at least five times the reservoir radius for the Mogi source equations to be valid (*Dzurisin*, 2007). Two, for a physically-reasonable radius, the corresponding overpressure should not exceed rock strength of approximately 10 MPa (e.g. *Gudmundsson*, 2012). Three, multiple sources should be separated by at least 8 times the largest radius. The results of our Neighborhood Algorithm inversion meet these criteria as long as the upper crustal reservoir has a radius less than 3 km.

Interestingly, the ratio of u_r/u_z is increased for a magmatic dipole compared to the ratio for a single reservoir. This is due to the superposition of components of deformation for each source. Previous studies have shown that for prolate sources $u_r/u_z > 0.5$ and for oblate sources $u_r/u_z < 0.3$ in a homogeneous medium (*Dieterich and Decker*, 1975). For Uturuncu, superimposing the solutions for reservoirs at 20 km and 70 km, the ratio *increases* to 0.46, potentially biasing monopole inversions toward more prolate geometries. Forward modeling indicates that u_r/u_z increases as the source and sink reservoirs move closer together, and as the ratio of source to sink volume increases. Importantly, the presence of a source reservoir does not decrease u_r/u_z below 0.3, and therefore monopole inversions should not be biased toward sill-like geometries. While informative, this simple analysis is restricted in that both reservoirs are well approximated as point sources, vertically aligned, and embedded in homogeneous Poissonian crust.

3.4 Heterogeneous Finite Element Forward Model

In order to investigate the role of 3D heterogeneity and anelastic material properties, we constructed a Finite Element Model (FEM). Our model mesh consists of a quarter cylinder with a radius of 300 km and a depth of 200 km (Figure 3.11). Previous finite element modeling at Uturuncu utilized an axis-symmetric formulation to explore 1D subsurface layering (*Hickey et al.*, 2013). The quarter cylinder design permits exploration of 3D subsurface heterogeneity while maintaining reduced computational expense by taking advantage of mirror plane symmetry. A sink reservoir is located at 20 km depth and the source reservoir at 70 km depth along the cylinder axis. We chose these depths because they are

coincident with observed seismic anomalies, and permit assessment of heterogeneity within the entire crustal column. Boundary conditions include outward normal traction applied to the reservoir surfaces, the upper surface is free, no displacement is allowed normal to the cut-out cylinder sides, and zero displacement is enforced on the outermost curved surface. The mesh was generated with CUBIT software and consists of $\approx 10^6$ linear tetrahedral elements. Numerical solutions of the mechanical response are performed with Pylith software (*Aagaard et al.*, 2013). Solutions are benchmarked against superimposed semi-analytical Mogi solutions for a Poissonian half-space (Vp=5773 m/s , Vs=3333 m/s, ρ=2700 kg/m^3, E=75 GPa, G=30 GPa, ν=0.25), and also evaluated against spatial and temporal InSAR observations of surface deformation (Figure 3.13).

Finite element modeling is an especially useful tool if strong constraints on either properties of the pressurizing reservoir (e.g. hypocenter, geometry, volume of intruding material), or properties of the crustal column (e.g. rheology, stiffness) are well determined. For example, precisely located earthquakes can help pinpoint reservoir location and shape, and then a variety of crustal rheological responses can be tested (e.g. *Got et al.*, 2013). Alternatively, if crustal heterogeneity is known from tomography, a variety of plausible reservoir locations and geometries can be tested (e.g. *Hautmann et al.*, 2010). In the case of Uturuncu, seismicity tends to concentrate in the upper crust and at the slab interface (*Jay et al.*, 2012), and consequently hypocenters do not appear to outline magma reservoirs in the mid and lower crust. We therefore used available seismic imaging data in order to constrain material properties in the finite element model.

Anomalously thick crust of over 70 km and low seismic velocities (Vp=6.2,

Vs=3.45 km/s) underlaying the Altiplano Plateau have been known about for decades (*James*, 1971). More recently, receiver function analysis described a 1 km thick feature at 19 km depth with the following properties: Vp=4 km/s, Vs=1 km/s, ρ=2400 g/cm3 (*Chmielowski et al.*, 1999; *Zandt et al.*, 2003; *Leidig and Zandt*, 2003). A roughly coincident low resistivity layer has led to the hypothesis that this feature is a sill of 5-10% andesitic partial melt known as the Altiplano-Puna Magma Body (APMB) (e.g. *Schilling et al.*, 1997; *Unsworth et al.*, 2013). The APMB has figured strongly into previous geodynamical studies (e.g. *Babeyko et al.*, 2002; *de Silva and Gosnold*, 2007; *Fialko and Pearse*, 2012). However, recent joint inversion of ambient noise tomography and receiver functions has drastically changed the geometric description of the APMB: It is now believed to be a much thicker zone of ultra-low velocities ($1.9 < Vs < 2.9$ km/s) between 5 to 25 km depth, and a diameter of over 200 km (*Ward et al.*, 2014). These contrasting seismic velocity models are synthesized in Figure 3.15. The new characterization of the APMB partly results from incorporating additional data from an array of 28 broadband seismometers deployed between 2010 and 2013 with 50 km of Uturuncu. *Ward et al.* (2014) assume a Poissonian crust (Vp/Vs=1.73), although recent local body wave tomography shows perturbations of Vp/Vs on the order of $\pm 5\%$ within a 50 km radius of Uturuncu (*West et al.*, 2013). Such decreases in the Vp/Vs ratio are expected to slightly increase depths to particular layers.

3.4.1 Assignment of material properties

On elastic timescales, a weak subsurface layer is known to amplify radial and vertical strain disproportionally from pressurization at depth (e.g. *Geyer and*

Gottsmann, 2010). We therefore investigated models with a three dimensional weak zone defined by the low velocities of the APMB. We used the tomographic velocity model in *Ward et al.* (2014) to directly assign material properties within the finite element mesh. Each element is assigned elastic moduli defined by direct conversion of Vp, Vs, and density. The primary measurement from *Ward et al.* (2014) is Vs, and Vp is obtained given the Poissonian assumption (Vp/Vs=1.73). Finally, density is assumed constant at $2700 g/cm^3$ throughout the crust. Figure 3.12 shows the heterogeneous material properties embedded in the FEM mesh.

We remark that 'dynamic moduli' derived from seismic velocities are generally higher than the 'static moduli' derived from laboratory rock deformation experiments. Since these discrepancies can be attributed to micro-crack density (e.g. *Cheng and Johnston*, 1981), better agreement is anticipated with increasing depth due to crack closure. Reductions to dynamic moduli have been proposed in some volcano deformation studies as a means to artificially simulate more realistic longer duration anelastic crustal response (e.g. *Trasatti et al.*, 2005). Therefore we believe the elastic material properties in our model are reasonable as upper bounds.

3.4.2 Heterogeneous Results

While we have explored 3D heterogeneity in material properties based on seismic tomography, we note that the observed variation is effectively 1D (velocity gradient with respect to depth). In fact, the extent of the APMB low velocity zone exceeds the deformation footprint observed at Uturuncu, and the charac-

teristic length scale of lateral variation in seismic velocities is tens of kilometers.

Including this broad weak zone between the inflating reservoir and the surface causes the ratio u_r/u_z to *decrease* to 0.30, representing a significant 35% decrease compared to the homogeneous benchmark (Figure 3.14). Maximum uplift is also increased by over 3x, such that the inferred volume from homogeneous inversions may be overestimated by the same amount. The effect is amplified if the layer is thicker, made of weaker material, and closer to a pressurizing reservoir. For example, moving the inflation source to a depth of 30 km decreases the ratio u_r/u_z by 25% compared to the homogeneous case, demonstrating how the effect of the weak layer on surface deformation diminishes for reservoirs of increasing depth. Most importantly, the APMB weak zone produces a greater reduction in u_r/u_z compared to the increase in u_r/u_z generated by inclusion of a source reservoir in a homogeneous space. The ratio observed when including the APMB, u_r/u_z =0.30, is in close agreement with observations west of maximum uplift. However, we observe a higher value of 0.38 to the east.

It is important to note that on elastic timescales, a weak layer amplifies both vertical and radial strain from underlaying sources, but vertical displacements are effected to a greater extent. In general, homogeneous half-space inversions for reservoirs with a pervasive overlaying weak layer will be biased towards more oblate geometries and will overestimate intrusion volume (or underestimate depth).

3.5 Discussion

3.5.1 Applicability of elastic models below the Brittle-Ductile Transition

A common criticism of the use of elastic models in volcano geodesy, is that the crust deforms anelastically below the Brittle-Ductile Transition (BDT) (e.g. *Carter and Tsenn*, 1987). However, it is important to realize that viscous creep processes taking place at depth do so over timescales determined by temperature, strain rate, and composition. Consequently, if a material deforms nonlinearly according to a powerlaw constitutive law, short-term elastic responses should be expected for $t << \tau$ where τ is the effective relaxation time for the material. The thermal structure of the crust is therefore critical in determining the appropriate rheology for Uturuncu.

Geodynamic models examining the evolution of geotherms in the vicinity of Uturuncu have suggested that quasi-steady intrusion of high temperature magmas inferred from surface volcanism create persistent high temperatures in the mid crust (*de Silva and Gosnold*, 2007). Additional geodynamical modeling has even suggested that the lower crust must undergo bulk convection in order to supply sufficient heat to the mid crust, which is only possible if the lower crust behaves according to powerlaw constitutive law for a wet granite composition (*Babeyko et al.*, 2002). Finally, *Fialko and Pearse* (2012) proposed a geotherm bounded by the solidus for granite in the mid crust and basalt in the upper mantle. These geotherms are summarized in Figure 3.16.

Given a geothermal gradient and laboratory derived constitutive powerlaw

parameters, it is possible to estimate viscosity and relaxation time with depth (e.g. *Kirby and Kronenberg*, 1987). Using the geotherm proposed by *Fialko and Pearse* (2012) and parameters for a range of compositions we plot effective relaxation times versus depth for Uturuncu (Figure 3.16). There are several important points to take away from this figure. First, the range of possible viscosities (and corresponding relaxation times) span many orders of magnitude depending on composition. Second, assuming a single representative composition for the crust, the viscosity surrounding a mid crustal reservoir is predicted to be at least several orders of magnitude greater compared to lower crustal reservoir. Quartzite and wet granite compositions proposed in *Babeyko et al.* (2002) seem incompatible with the geotherm proposed by *Fialko and Pearse* (2012) because predicted viscosities below 15 km depth are comparable to fully molten magmas (e.g. *Giordano et al.*, 2008).

While weak felsic rheology predicts a shallow brittle, ductile transition in agreement with seismicity (*Jay et al.*, 2012), a more intermediate middle and lower crustal composition may be justified given the andesitic and dacitic composition of eruptive products. Indeed, a diorite flow law predicts a crustal viscosity on the order of 10^{18} Pa s for the lower crust. Independent constraints on the viscosity of the lower crust in the Central Andes are limited, but one study of lake loading indicates viscosities less than 10^{20} Pa s below 40km depth (*Bills et al.*, 1994). Other studies of post-seismic relaxation (e.g. *Freed and Buergmann*, 2004) also cite probable viscosity ranges of $10^{18} - 10^{21}$, but may only be applicable to specific tectonic settings.

3.5.2 Mass balance between dipole reservoirs

We must reconcile the fact that elastic inverse dipole models estimate the volume of the deeper reservoir to be 1-8x greater than the shallow reservoir. A similar 1:10 sink to source volume mismatch was pointed out for the dual reservoir model at Soufriere Hills Volcano (*Foroozan et al.*, 2010). Owing to changing reservoir compliance, magma compressibility, and crustal rheology with depth, volume discrepancies in geodetic inversions should be expected. For example, volume ratios of approximately 5:1 have been observed for shallow dyke inflation compared to adjacent chamber deflation (e.g. *Wright et al.*, 2006). This ratio has been convincingly explained by compressibility arguments (*Rivalta and Segall*, 2008); however, the inverse ratio is observed for the dipole model. Under what conditions might this ratio arise?

Following notation in (*Segall*, 2010), incremental mass in an intrusion is found by applying the chain rule to $m = \rho_m V$:

$$\delta m = \rho_m \delta V + \delta \rho_m V \tag{3.1}$$

Equating incremental mass between source (δm^-) and sink (δm^+) reservoirs, it is possible to solve this for a volume ratio. We incorporate the relations for magma compressibility $\beta_m = \frac{1}{\rho_m}\frac{\partial \rho_m}{\partial p}$, spherical chamber compressibility is $\beta_c = \frac{3}{4\mu}$ (*Tiampo et al.*, 2000), and reservoir volume change due to inflation $\delta V = \pi a^3 \delta p / \mu$. As a result, for connected source and sink reservoirs the volume ratio becomes:

$$\frac{\delta V^-}{\delta V^+} = \left(\frac{\rho_m^+}{\rho_m^-}\right)\left(\frac{1+\beta_m^+/\beta_c^+}{1+\beta_m^-/\beta_c^-}\right) \tag{3.2}$$

In general, as depth increases, magma density increases ($\frac{\rho_m^+}{\rho_m^-} > 1$), magma compressibility decreases ($\frac{\beta_m^+}{\beta_m^-} < 1$), and reservoir compressibility also decreases ($\frac{\beta_c^+}{\beta_c^-} < 1$). The theoretical volume ratio critically depends on the ratio of magma compressibility to chamber compressibility ($\frac{\beta_m}{\beta_c}$) at a given depth. Interestingly, if shear modulus, density, and magma compressibility remain relatively constant, vertically-aligned source and sink reservoirs separated by a sufficiently small distance would produce equal and opposite strain fields and no surface deformation would be expected. As a corollary, subsidence moat signals from vertically-aligned sources would only appear if the ratio of volume changes is sufficiently large. These two points are very important, since they may factor into the lack of deformation observed to-date in some arcs (*Ebmeier et al.*, 2013), or the general scarcity of subsidence signals accompanying episodes of volcanic uplift.

Application to Uturuncu

Inversion of geodetic data at Uturuncu suggests $\frac{\delta V^-}{\delta V^+} \approx 4$. Assuming andesite magma, the density should decrease as it ascends such that $\rho_m^+/\rho_m^- \approx 1.1$ (*Spera*, 2000). Therefore, compressibility changes must offset the density effect. To determine compressibility values we have a single equation and four unknowns, so we must rely on estimates from independent datasets. We estimate chamber compressibility from the Vs velocity model of *Ward et al.* (2014) (see Figure 3.15), such that $\mu^- \approx 12$ GPa and $\mu^+ \approx 40$ GPa, corresponding to $\beta_c^- = 6.3\text{x}10^{-11}\text{GPa}^{-1}$ and $\beta_c^+ = 1.9\text{x}10^{-11}\text{GPa}^{-1}$ respectively. If we assume these values for rigidi-

ties, and a lower bound source magma compressibility of $4\text{x}10^{-11}\text{GPa}^{-1}$ (*Spera*, 2000), the corresponding sink compressibility is required to be $1.1\text{x}10^{-9}\text{GPa}^{-1}$. This relatively high compressibility could possibly be explained by exsolution of volatiles, which is discussed in the next section.

Volatile Exsolution

We seek to answer the question, can compressibility account for volume discrepancies between the lower crustal and mid crustal reservoir at Uturuncu? Other studies report that even for < 1 wt% CO_2 and H_20, magma compressibility can increase by an order of magnitude (> 10 GPa^{-1}) in the upper crust (*Rivalta and Segall*, 2008). Common lavas typically have < 5 wt% dissolved H_20 and CO_2, which can drastically reduce magma density and other physical properties such as viscosity (e.g. *Richet et al.*, 1996). Furthermore, once bubbles form by exsolution of dissolved volatiles magma properties are further effected (e.g. *Sparks*, 1978). *Huppert and Woods* (2002) outline a simple quantitative model for estimating compressibility of a magma with a single volatile phase ($\beta_m = \frac{1}{\rho_m}\frac{\partial \rho_m}{\partial p}$), where:

$$\rho_m = \left[\frac{n}{\rho_g} + (1-n)\left(\frac{x}{\rho_g} + \frac{1-x}{\rho_l}\right)\right]^{-1} \tag{3.3}$$

Where x is the mass fraction of crystals, n is the mass fraction of exsolved volatiles, and the density of gas is determined from the ideal gas law $\rho_g = p/RT$. The quantity n is estimated by Henry's Law, $n = N - sp^{\beta}(1-x)$, in which N is the total volatile mass fraction, and s and β are empirical constants that depend on the combination of volatile and melt compositions. For H_2 in rhyolite, $\beta = 0.5$,

and $s = 4.1\text{x}10^{-6}$ Pa$^{-\beta}$ (*Burnham*, 1975).

Lavas at Uturuncu erupted between 690 and 271 ka are predominantly dacitic (64-68% SiO_2) with melt inclusions of rhyolite composition 68 - 77% SiO_2 and water H_2 contents ranging between 1.5 and 5.3 wt% (*Sparks et al.*, 2008). Assuming the melt inclusions were trapped at H_2 saturation, this implies pre-eruptive *minimum* storage depth of 6.5 km. Consequently, all volatiles should be dissolved in the melt for 6.5 km and deeper and compressibility is constant ($\approx 10^{-10}\text{GPa}^{-1}$). Therefore, a compressibility value required to explain the geodetic volume discrepancy (10^{-9}GPa^{-1}) is not achieved until tens of kilometers above the inferred intrusion depth. However, lower melt compressibility in the mid crust could be achieved by assuming a larger solid crystal fraction. For example, a crystal mass fraction of 0.5 predicts a saturation depth of 27 km all else being equal.

The presence of other volatiles (CO_2, SO2, Cl) could also be important in determining mid-crustal compressibility. In particular, CO_2 exsolves at greater depth than H_2, lowers H_2 solubility, and may be up to 1.5 wt% in lower crustal silicic melts (e.g. *Blundy et al.*, 2010). A more recent study of melt inclusions in Uturuncu dacites confirms previous H2O measurements (3.2 ± 0.7 wt%), but also low CO_2 ($<$ 160 ppm) (*Muir et al.*, 2014a). Furthermore, volatile-saturated Uturuncu andesite at 20km depth could contain 9-11 wt% H_2 and 0.1-0.2 wt% CO_2 (Muir 2014 personal communication), which is at the upper end of maximum water content in parental arc magmas (*Wallace*, 2005). To assess the role of CO_2, constants in equation 3.3 for CO_2 are modified to $\beta = 1$, and $s = 2.4\text{x}10^{-3} Pa^{-\beta}$ (*Parfitt and Wilson*, 2009). Assuming an end-member concentration of 1.5 wt% CO_2 yields a minimum saturation depth of 26km for full melt. Again, the satu-

ration depth is lowered for increasing crystal content.

In summary, once saturation of either CO_2 or H_2 is reached, compressibility changes by orders of magnitude over tens of kilometers of ascent (Figure 3.17), but saturation depths in the lower crust are difficult to rationalize. Therefore, this phenomenon may explain volume discrepancies for shallow systems (e.g. Soufriere Hills), but is an unlikely candidate to explain the volume discrepancy observed at Uturuncu. That being said, further analysis could consider more complex solubility laws that quantify the nonlinear interdependence of two or more volatile species (e.g. *Baker and Alletti*, 2012).

Viscoelastic shells

An alternative explanation of the volume discrepancy is that country rock rheology differs significantly between the lower crust and mid crust. Weak felsic rheology in the lower crust of $10^{11} Pas$ imply relaxation on the order of seconds (Figure 3.16). If these low viscosities are restricted to a shell surrounding a reservoir, stress relaxation would transfer pressures out to the shell radius within minutes. Due to temporal aliasing in geodetic observations, such an event would appear as the elastic response of a larger reservoir. More specifically, following the derivation of *Segall* (2010), $\frac{\delta V2}{\delta V1} = \left(\frac{R2}{R1}\right)^3$ for $t << \tau$. An eight-fold increase in inferred volume change from geodetic data would require a viscous region of 2x the source chamber radius.

Based on Figure 3.16, the relaxation time is on the order of minutes with weak felsic rheology in both the lower crust and mid crust. Consequently, the observed volume discrepancy suggests that a shell be much larger for the lower

crustal chamber. Alternatively, a diorite rheology predicts 1 yr relaxation times in the lower crust compared to 1 Ma relaxation times in the mid-crust. Geodetic observations would therefore only be sensitive to viscous effects in the lower crust, offering another possible explanation for the dipole model volume discrepancy.

3.5.3 Time dependence and transport mechanisms

Time dependence for elastic models is achieved exclusively via the time dependence of reservoir pressurization. In other words, to match cm/yr uplift rates at Uturuncu requires that pressure in our models also increase at a constant rate of $\approx$ 1-10 MPa/yr. The cessation of uplift in 2010 inferred from GPS measurements suggests that either the reservoir has maintained its cumulative overpressure, or. This may be considered unrealistic given that fluid transport models suggest a decelerating intrusion rate as pressures equilibrate between coupled reservoirs. An alternative explanation is that the reservoir grows outward at a linear rate, such that the imposed increasing pressure is a proxy for incremental fixed displacements.

3.6 Conclusions

Co-located uplift and subsidence at Uturuncu volcano in Southwest Bolivia may result from transient magmatic transport from the lower to mid crust.Geodetic inverse models of dipole reservoir pressurization provide a complementary constraint on storage depths with best-fitting depths of 15 - 35 km for a sink

reservoir and 55 - 80 km depth for a source reservoir.

The timescale of intrusion is difficult to distinguish from time-dependent inelastic crustal response; however, continuous GPS data shows an abrupt cessation of uplift since April 2010. This observation is suggestive that surface uplift may be an elastic response.

Homogeneous half-space models suggest that the volume of the source reservoir in the lower crust is 1-10x greater than the volume change in the mid-crustal sink reservoir. For an elastic crust, this discrepancy could arise from a disproportionate decrease in magma compressibility with depth compared to an increase in crustal shear modulus. For a viscoelastic response, the volume discrepancy may arise due the anticipated powerlaw decrease in viscosity with depth, creating distinct rheological conditions surrounding each reservoir.

Deep magmatic reservoir pressurization provides an impulse that can be used to query the integrated rheological response of tens of kilometers of overlaying crust. A finite element model was employed to evaluate effects of known mechanical heterogeneities, such as the Altiplano-Puna Magma Body, and various possible inelastic crustal responses at depth. Assigning elastic properties from seismic tends to weaken the crust compared to homogeneous models, requiring deeper source depths, or less volume change. Furthermore, a sill-like or oblate week zone such as the APMB disproportionately effects radial and vertical surface displacements, potentially biasing inferred source geometry from homogeneous models.

At present there are multiple viable mechanisms to explain the unprecedented deformation field at Uturuncu Volcano. Continued and more frequent

geophysical observations are required to further refine the temporal sampling of these transient deformation events. The potential intrusion of magma to shallower depths will prove an important contribution for hazard assessments since geodetic models imply current magmatic activity is much deeper than regional pre-eruptive chambers.

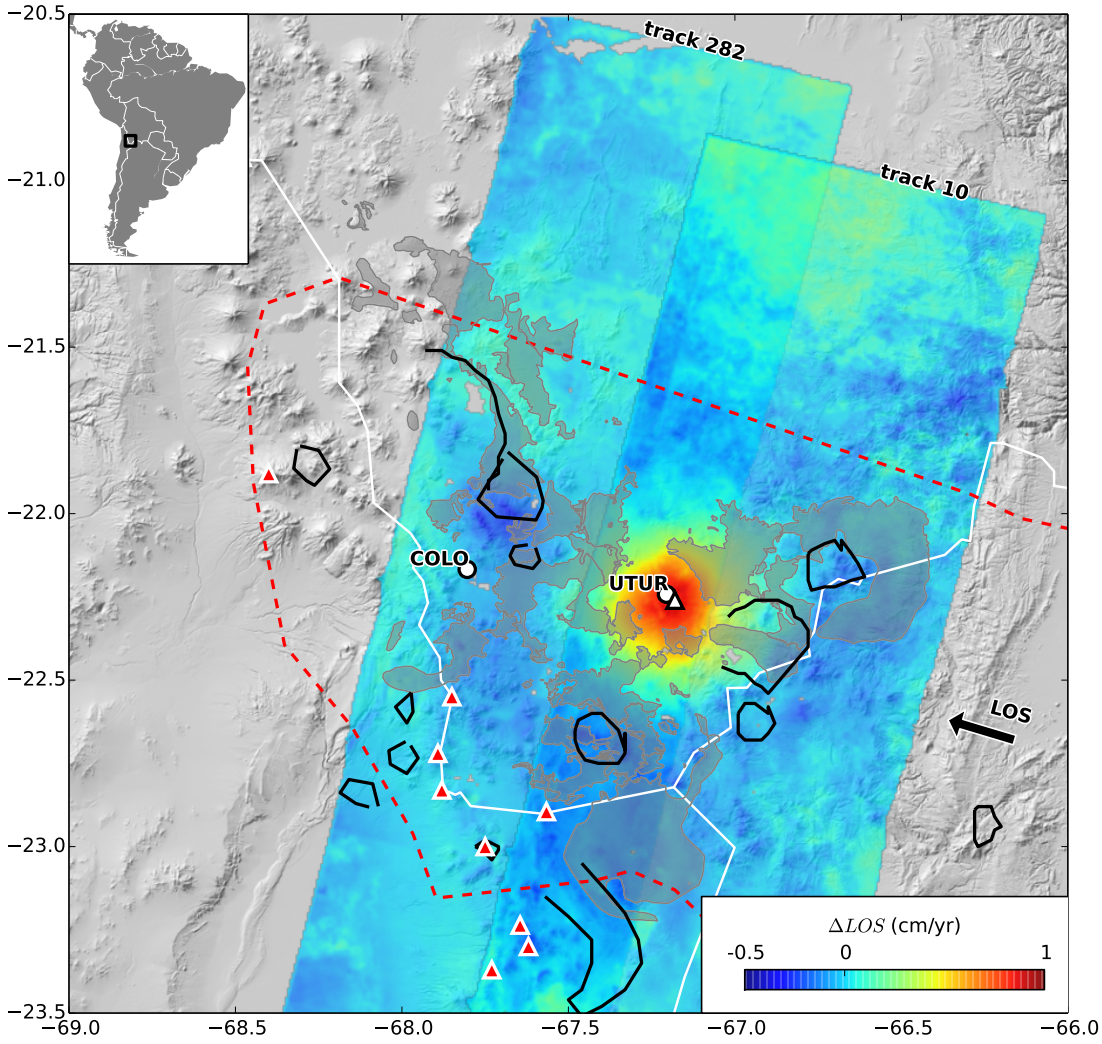

Figure 3.1: Uturuncu deformation in the context of the Altiplano-Puna Volcanic Complex. Two descending InSAR stacks are overlain on a SRTM digital elevation model. White triangle marks the location of Uturuncu summit, white circles mark continuous GPS stations. Solid black lines represent major calderas and hatched polygons are major ignimbrites of the APVC (*Salisbury et al.*, 2011). Red triangles are active Holocene volcanoes from the Smithsonian Global Volcanism Catalog (*Siebert et al.*, 2011). Red dashed outline marks the extent of the APMB (*Zandt et al.*, 2003).

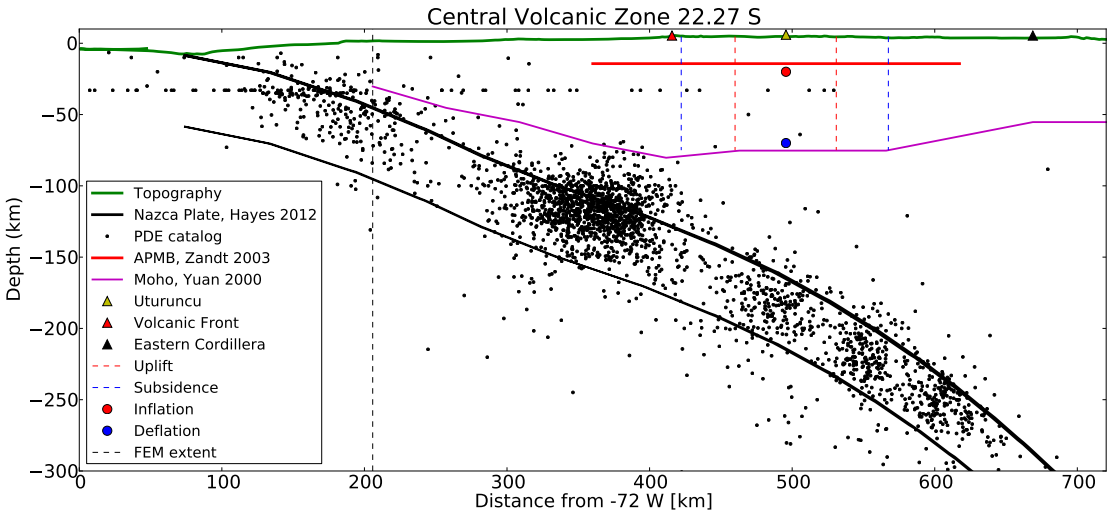

Figure 3.2: To-scale subsurface cross section at 22.27°S constrained by previous geophysical studies. Earthquake depths from USGS PDE catalog taken through through 01/2013, between 21°S and 23°S. Abbreviated references for features listed in legend.

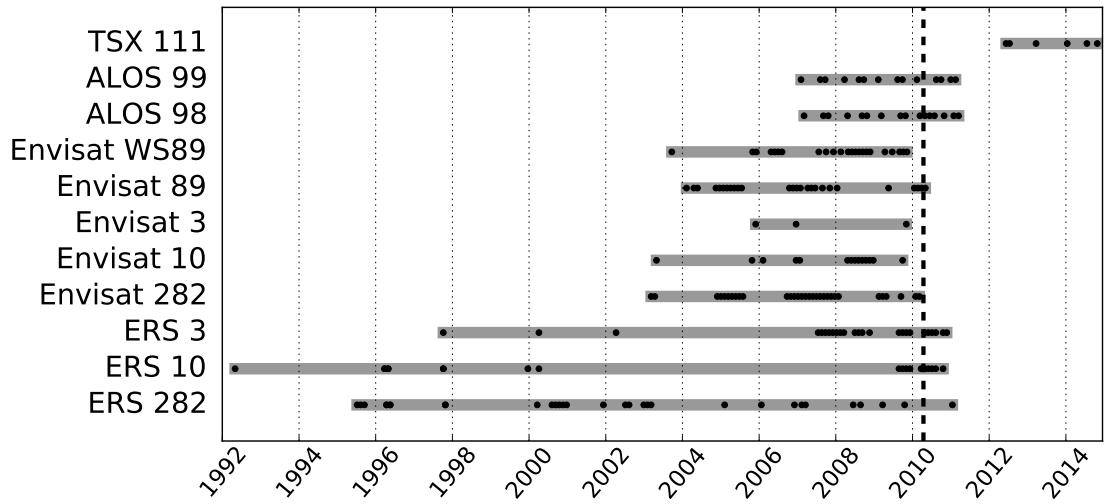

Figure 3.3: Timeline of InSAR data at Uturuncu. Dots represent acquisitions used in forming interferograms. Gray bars represent the span from earliest to latest acquisition (not necessarily usable in forming interferograms). The dashed vertical line corresponds to the installation of local continuous GPS sites UTUR and COLO.

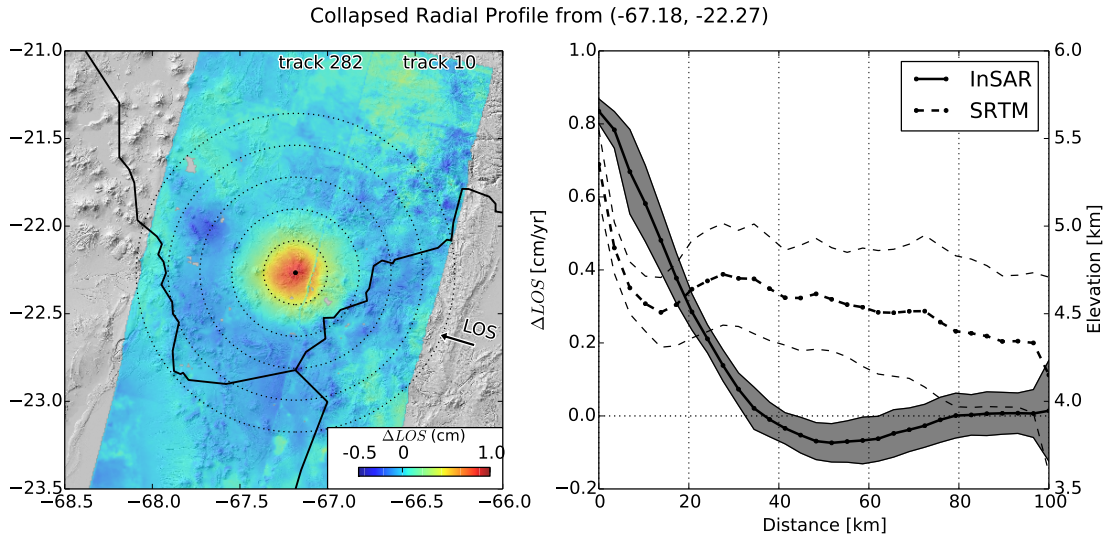

Figure 3.4: Left: Map of descending InSAR data showing center of deformation in relation to Uturuncu Summit (marked by black dot). Dashed circles correspond to equal incremental 20km radial distance. Right: Radially-averaged LOS displacement profile (solid black line) for 40 bins out to 100 km from the summit. Shaded grey region corresponds to 1 standard deviation bounds. Dashed lines show SRTM mean elevation and one standard deviation bounds. Note the uplifting and subsiding regions are not correlated with topography.

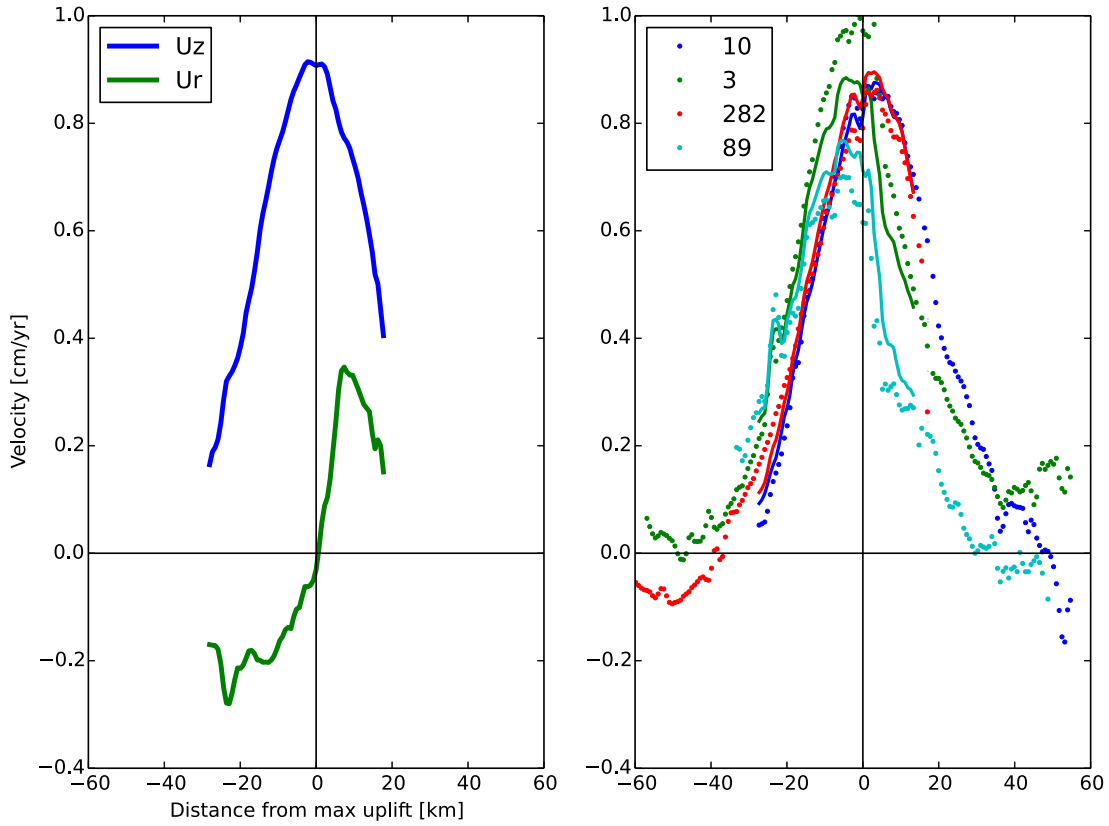

Figure 3.5: Left: Vertical and radial components of surface velocities derived from four InSAR stacks with the method of (*Wright et al.*, 2004b). Right: East-west profiles of data (colored points), based on a 10-pixel wide swath through the center of deformation. Solid colored lines correspond to the derived vertical and radial components (left) re-projected into each track's line of sight.

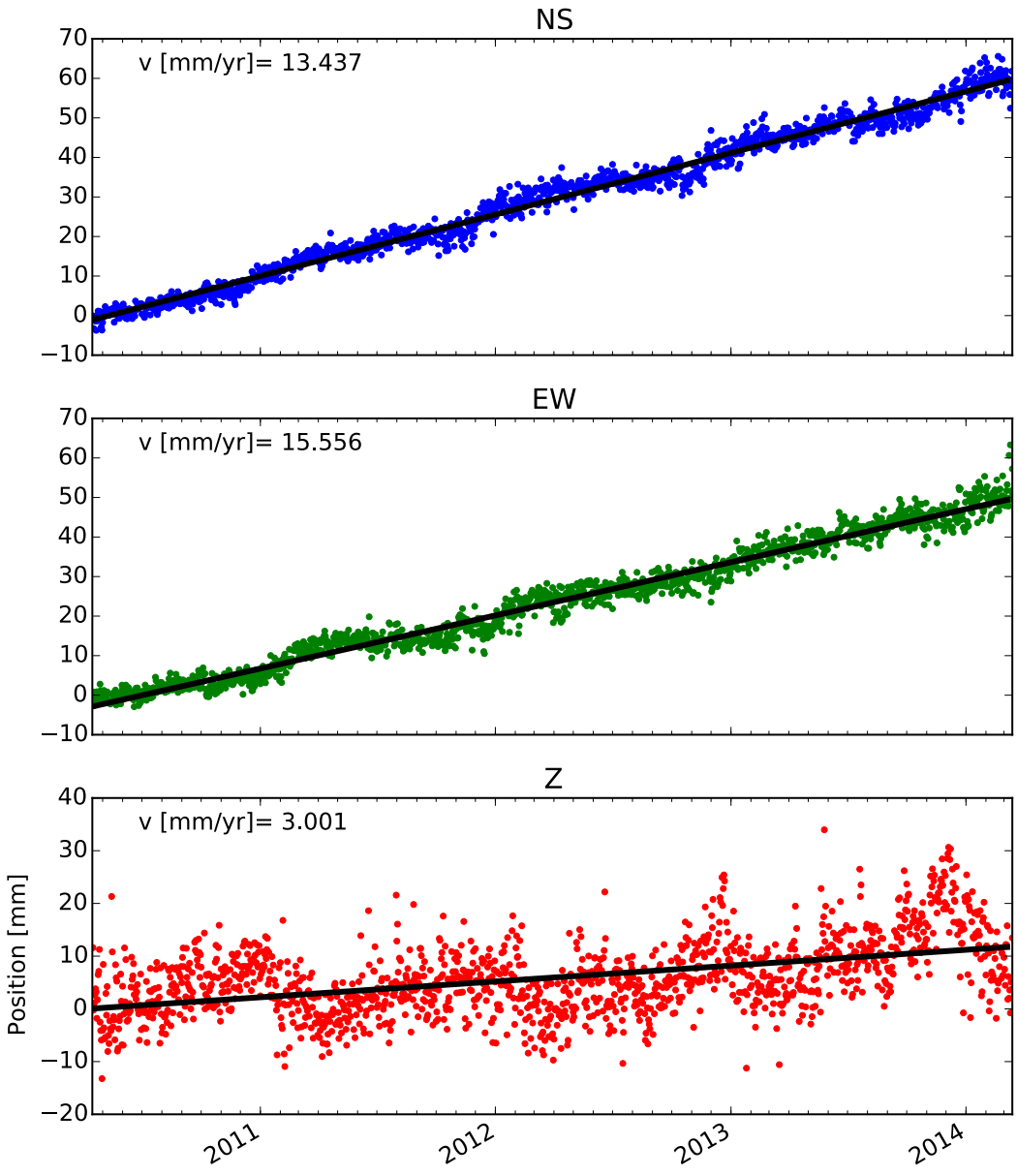

Figure 3.6: UTUR station timeseries. Blue is north-south component (positive north), green is east-west component (positive east), and red is vertical component. Rates [mm/yr] are calculated from least squares regression of daily IGS08 positions without removing a seasonal signal. Data has been processed by the University of Nevada Geodetic Laboratory (*Blewitt et al.*, 2013).

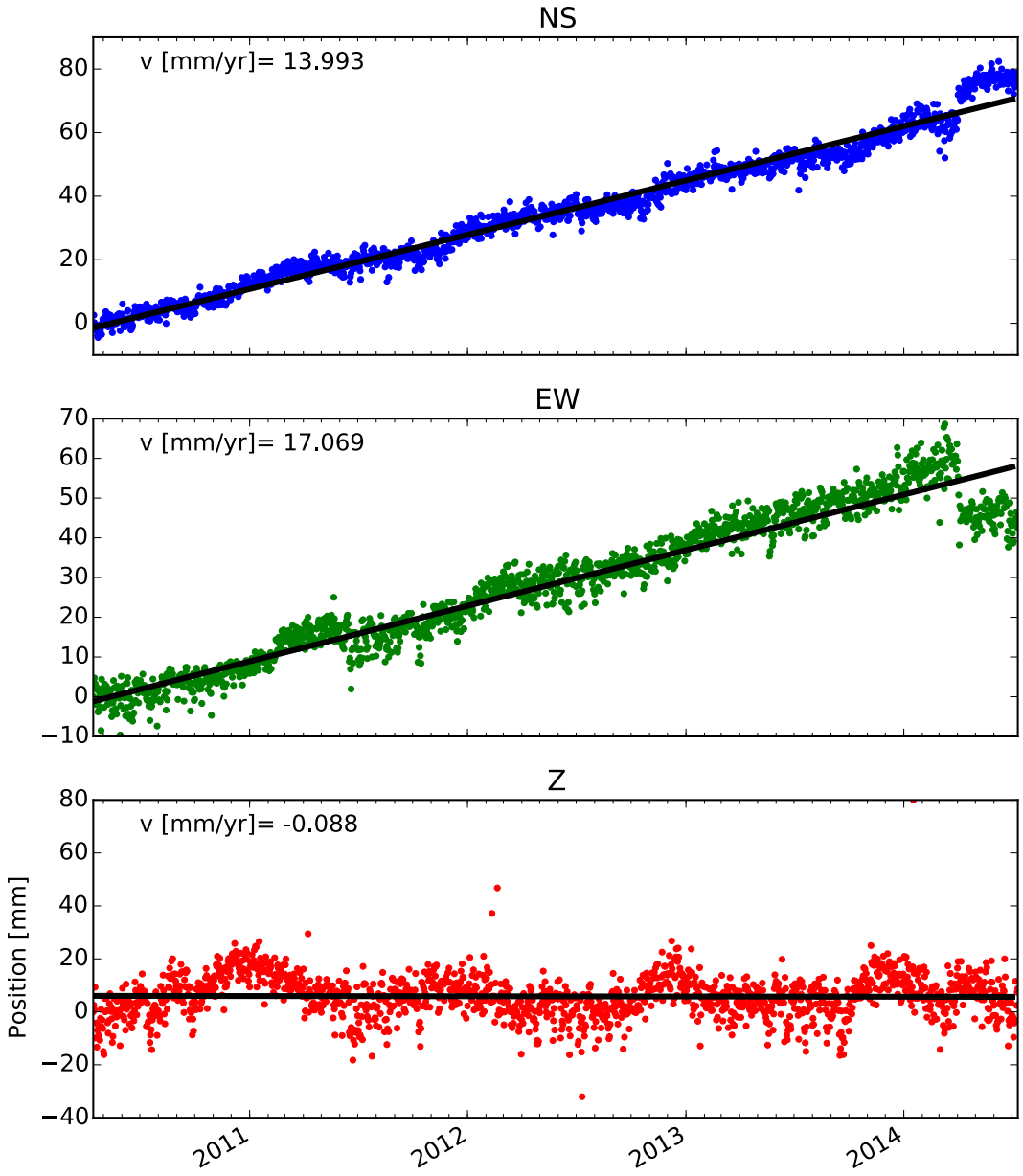

Figure 3.7: COLO station timeseries. Blue is north-south component (positive north), green is east-west component (positive east), and red is vertical component. Rates [mm/yr] are calculated from least squares regression of daily IGS08 positions without removing a seasonal signal. Data has been processed by the University of Nevada Geodetic Laboratory (*Blewitt et al.*, 2013).

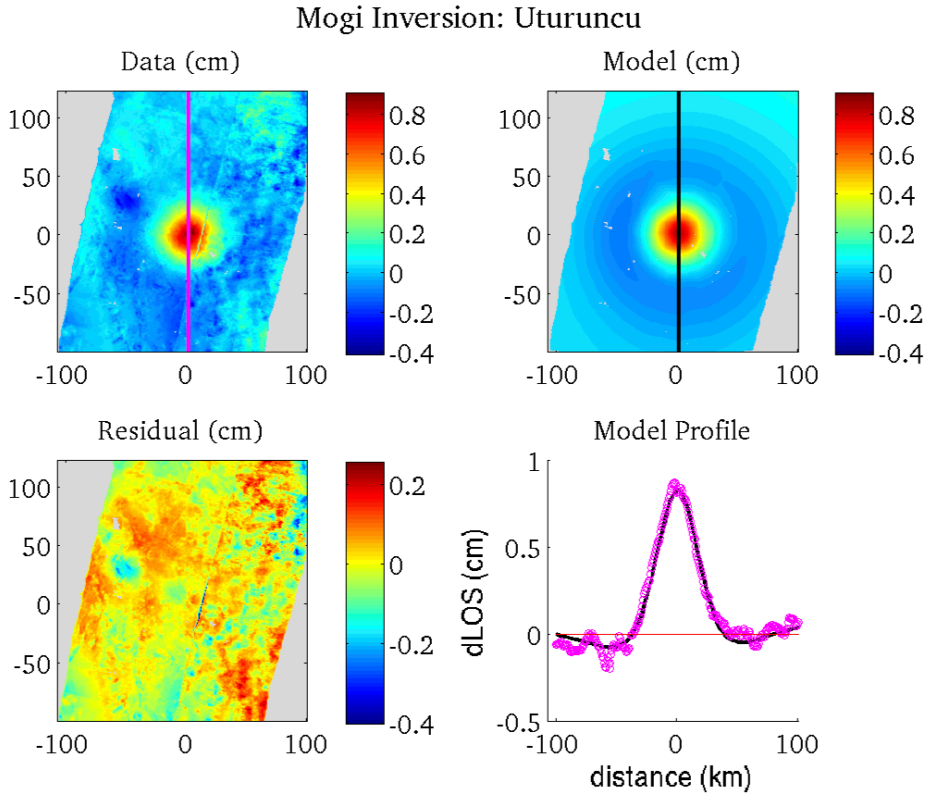

Figure 3.8: Dipole source solution based on Levenberg-Marquardt nonlinear least squares inversion for a Poissonian half-space. The source reservoir is located at 51 km with dV=0.3 km^3, and the sink reservoir is at 26 km with dV=0.03 km^3. Data points are marked in magenta and model prediction by a black line, showing reasonable agreement with both uplift and peripheral subsidence.

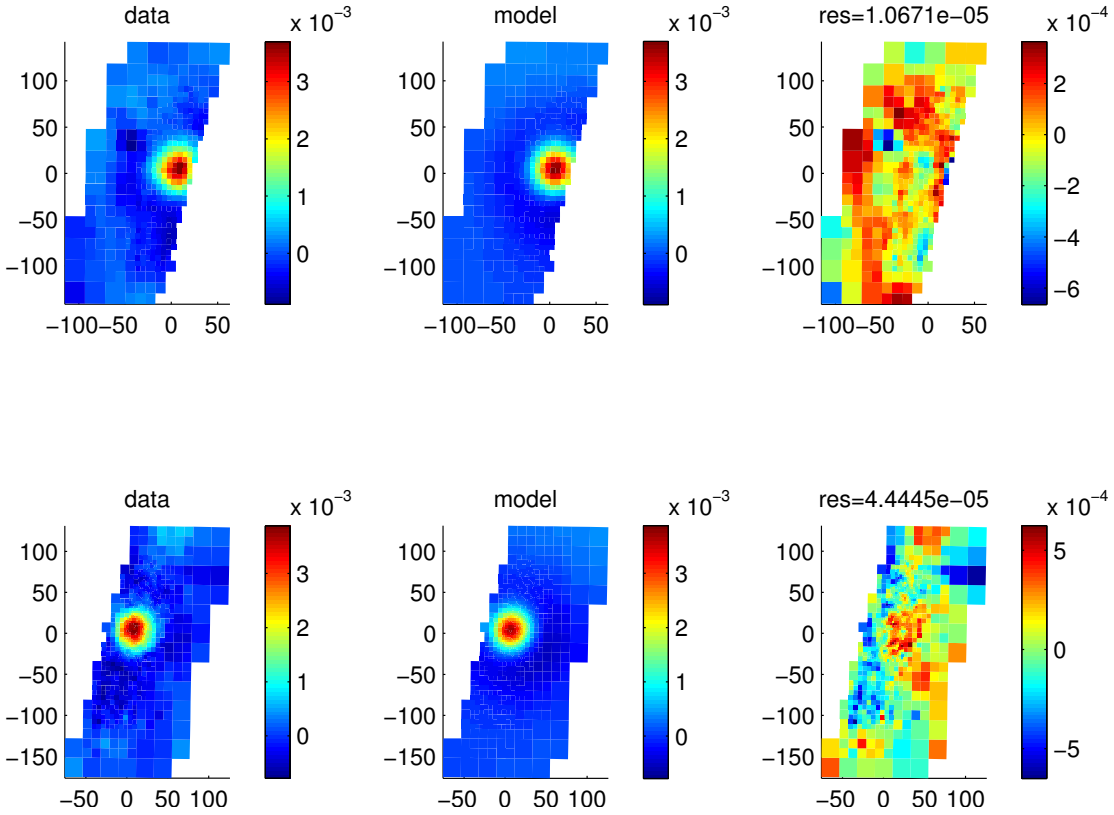

Figure 3.9: Best-fit model from Neighborhood Algorithm (*Sambridge*, 1999) inversion compared to stacks of descending data. Uplift source at (-67.235, -22.277), depth=35.8 km, dV=0.059 km^3, subsidence at (-67.204, -22.293), depth=52.2 km, dV=0.087 km^3. For range of model parameters searched see Figure 3.10. Figures for ascending data are included in Appendix B

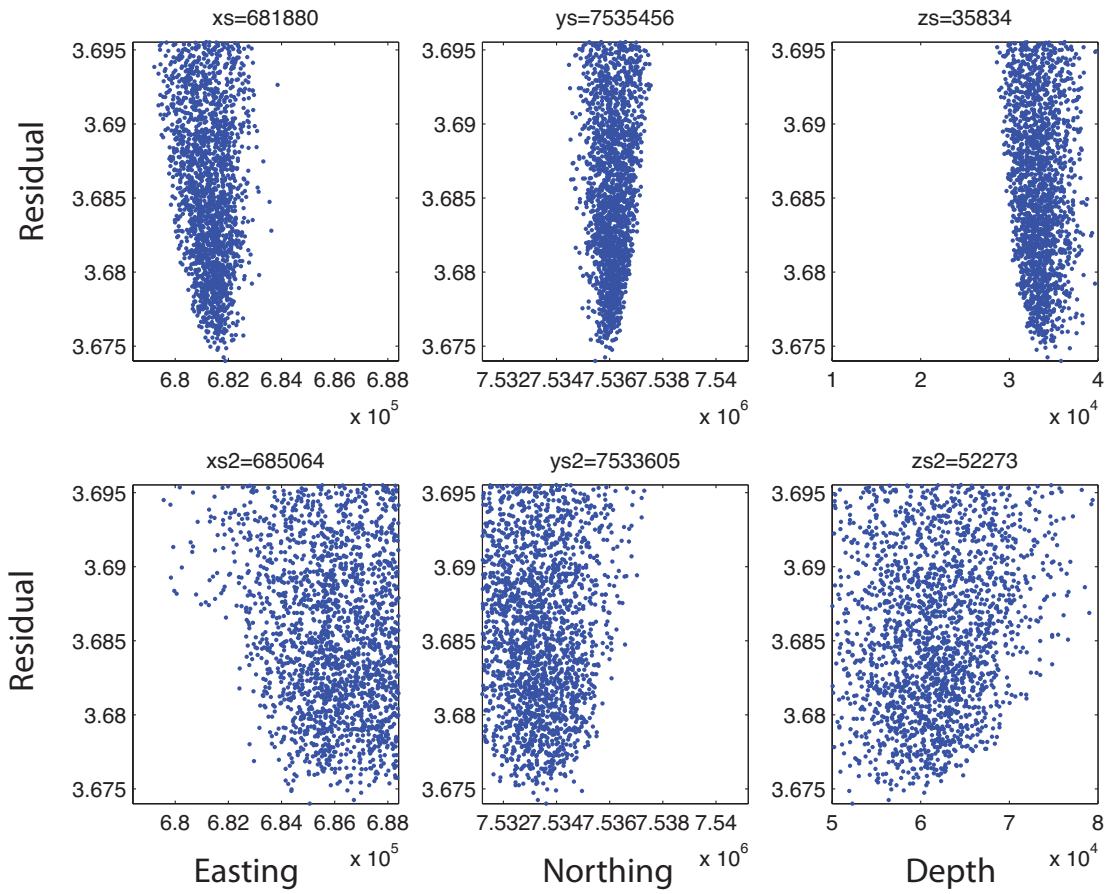

Figure 3.10: Parameter space queried in Neighborhood Algorithm inversion to determine best fit solution shown in Figure 3.9. Note that the position of the mid-crustal inflation source is much better constrained than the deeper deflation source, based on the fact that a wider range of depths produce comparable residuals.

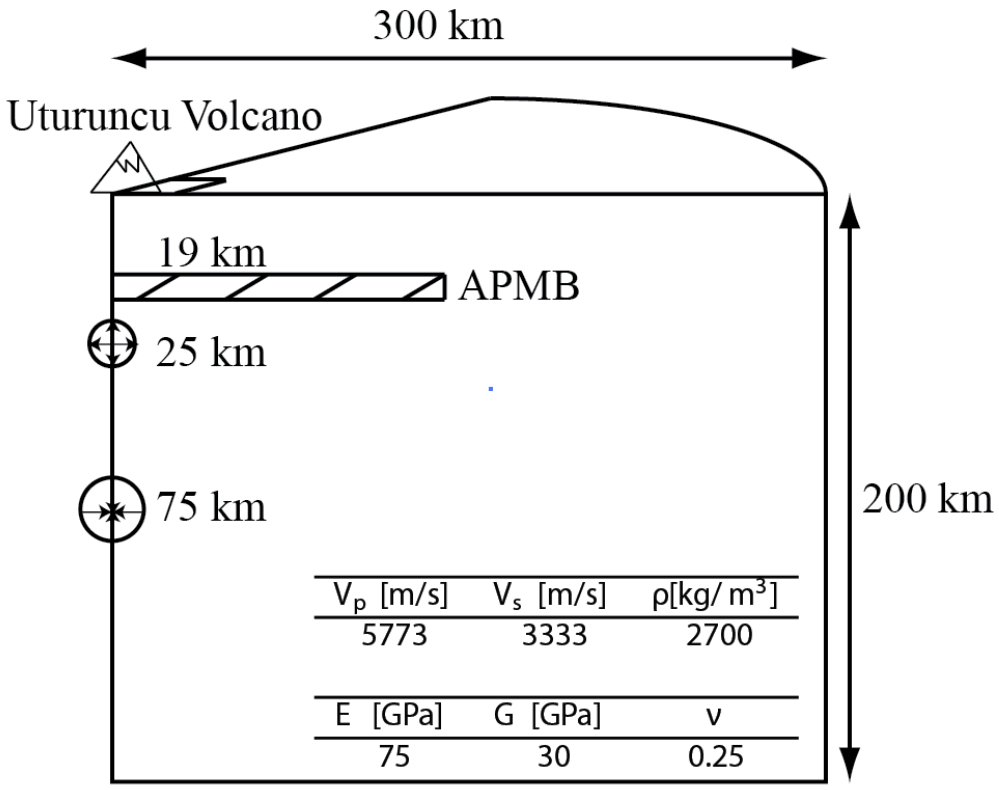

Figure 3.11: Schematic of finite element model mesh, not to-scale. We use a quarter cylinder in order to test large scale 3D heterogeneities within the crust, while minimizing computational cost. The domain has the following boundary conditions: Zero displacements on outer wall and base, zero perpendicular displacements on inner walls, normal tractions applied to spherical reservoir surfaces, and the ground surface is free. The approximate location of the APMB sill *Zandt et al.* (2003) is hatched for reference. Source and sink reservoir locations are for a particular model realization. Included material properties represent homogenous halfspace condition used for benchmarking.

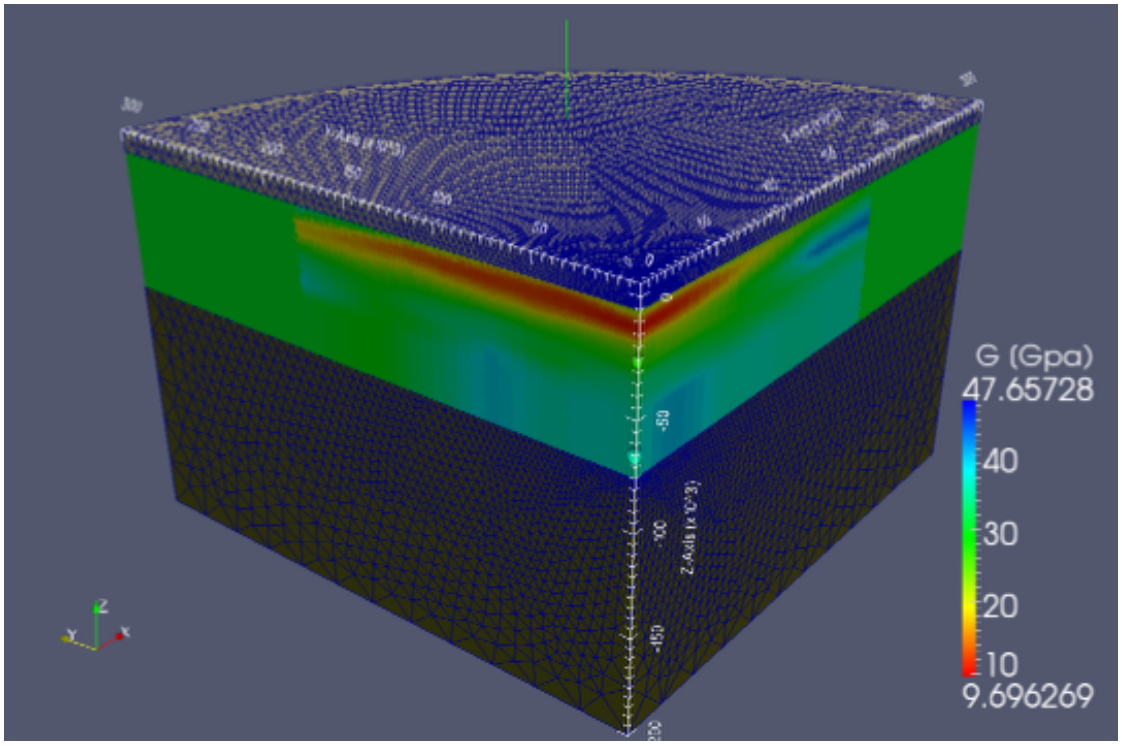

Figure 3.12: Isometric view of finite element model mesh. Shear modulus is shown for the middle crust directly assigned from the 3D seismic velocity model of *Ward et al.* (2014). Two pressurized reservoirs are embedded along the cylinder centerline at 20 and 70 km depth.

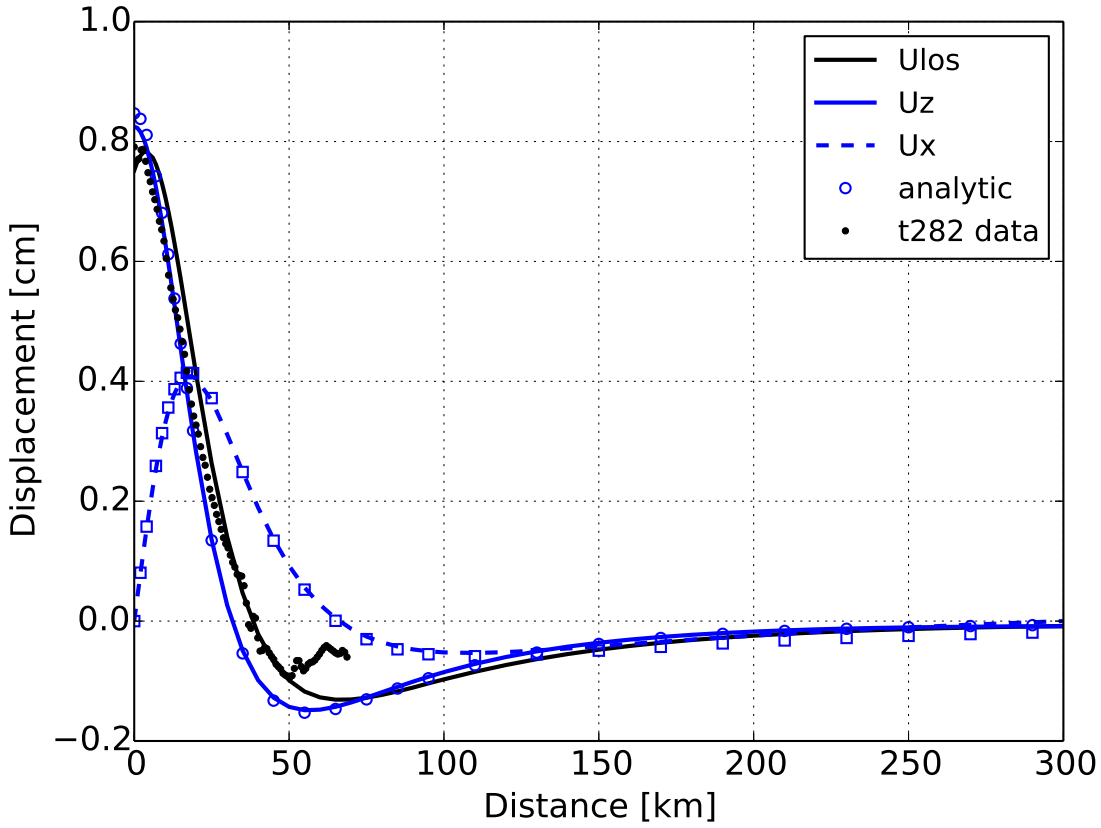

Figure 3.13: Benchmark of finite element mesh and comparison to InSAR data. Blue solid line is vertical displacements predicted by FEM, dashed blue line is radial displacements. Open squares represent the analytical solution. Solid black line shows FEM displacements converted to LOS, and black dots are taken from track 282 data (also show in Figure 3.5). Uplift and transition to subsidence is in agreement with data, however, the width of the moat signal is over-predicted.

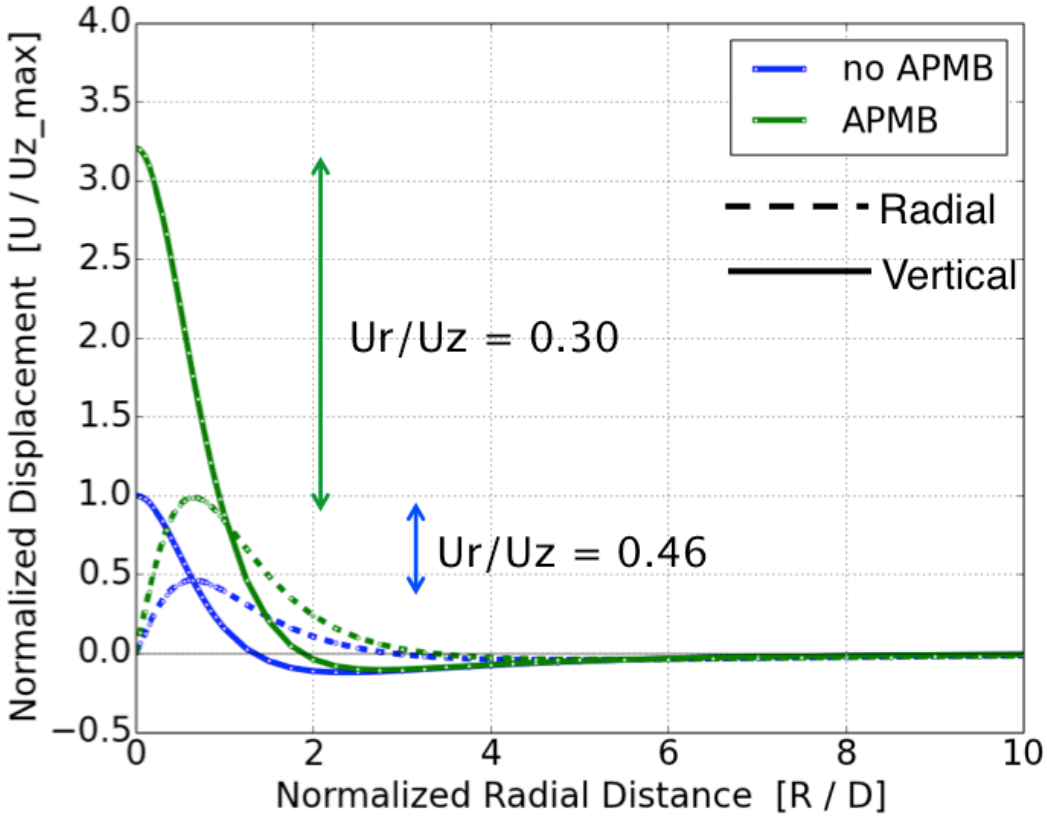

Figure 3.14: Comparison of finite element displacements with and without the APMB. Model setup is described in section 3.4.1. 'R' corresponds to radial distance from the center of deformation, which is normalized to the sink (shallower) reservoir source depth, 'D'. All displacements are normalized with respect to maximum vertical displacement without the APMB present (homogeneous solution). Note that the ratio u_r/u_z is significantly increased for homogeneous dipoles, and significantly decreased by the APMB heterogeneity, with respect to the analytic solution for a single Mogi source $u_r/u_z = 0.38$.

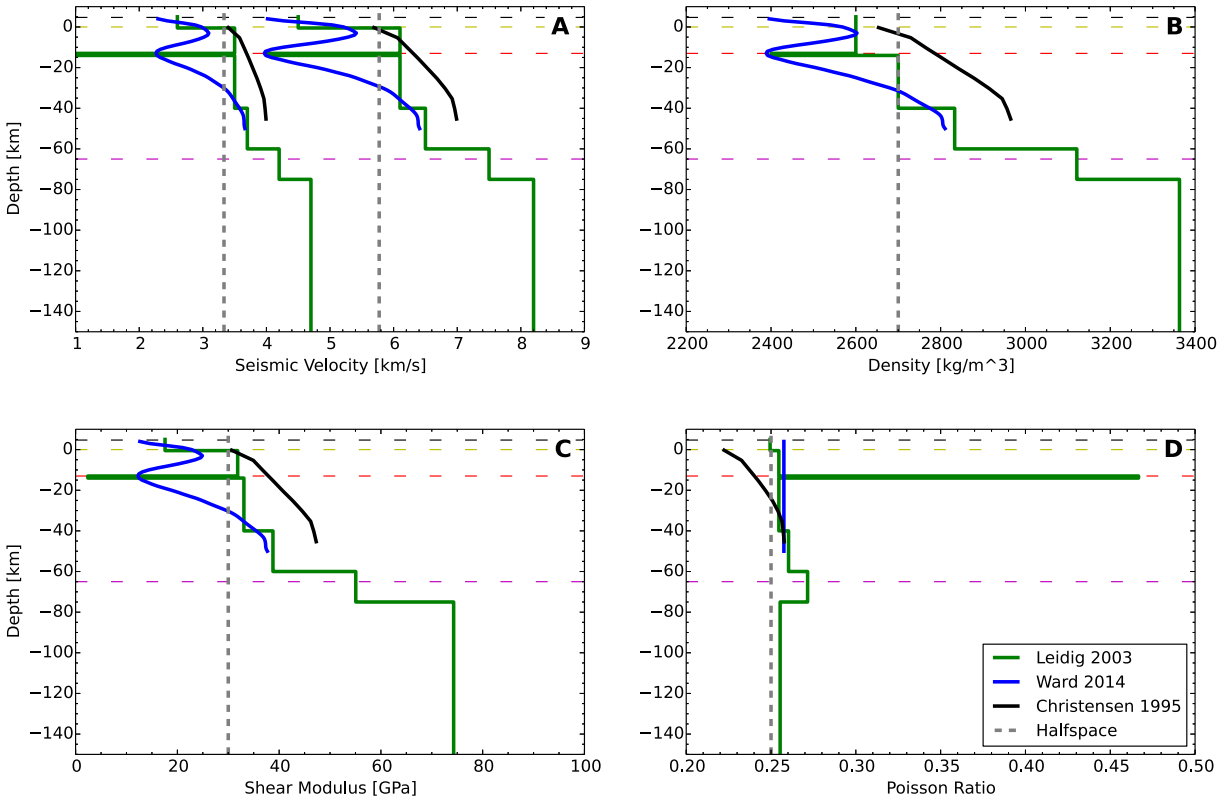

Figure 3.15: Summary of elastic properties derived from seismic data. Note legend in lower right indicating abbreviated references. Also dashed horizontal lines represent surface elevation, BDT (*Jay et al.*, 2012), APMB sill (*Zandt et al.*, 2003), and Moho (*Yuan et al.*, 2000). A: Vp and Vs velocity models proposed under Uturuncu, with average continental crust values for comparison. B: Conversion of seismic velocities to density based on the empirical relation of *Brocher* (2005). C: Dynamic shear modulus calculated from Vp,Vs, and density. D: Poisson ratio calculated from Vp and Vs.

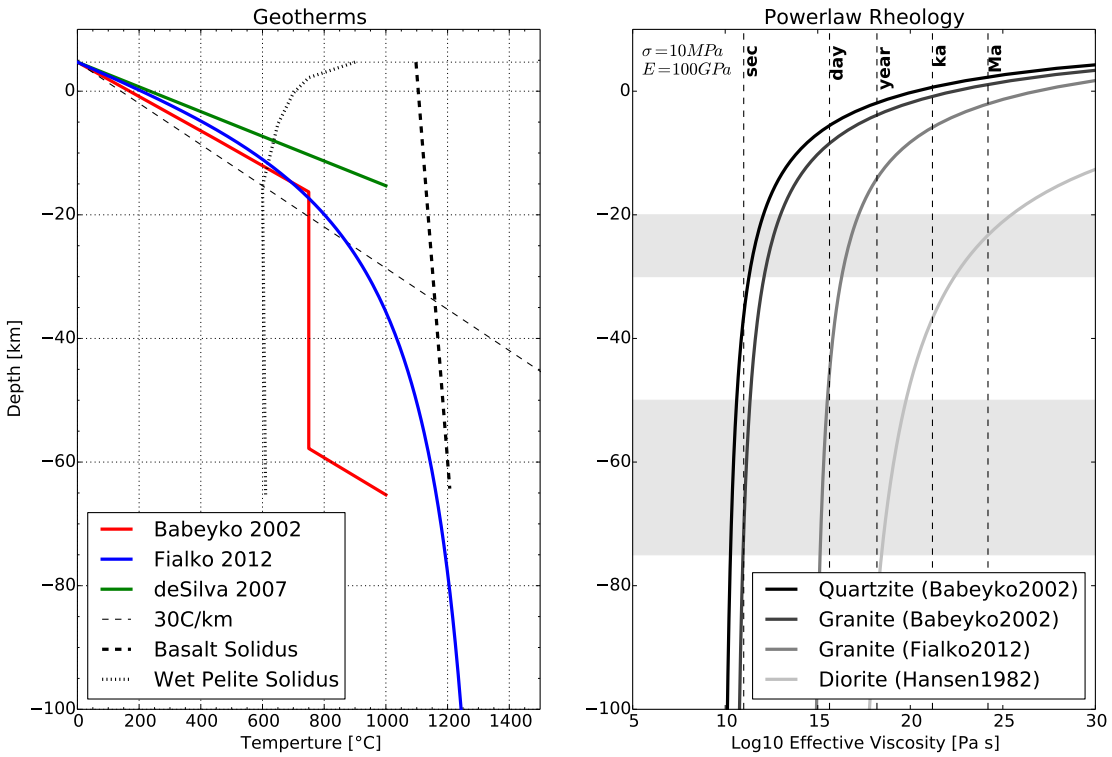

Figure 3.16: Left: Geotherms proposed for the vicinity of Uturuncu Volcano. The basalt solidus is reproduced from (*de Silva and Gosnold*, 2007), and the wet pelite solidus is digitized from (*Thompson*, 1982). Right: Effective viscosities calculated using the geotherm from *Fialko and Pearse* (2012), and laboratory-derived power law creep parameters listed in Table 3.3, for constant differential stress (10 MPa). Horizontal gray bands represent ranges of dipole reservoirs. Dashed vertical lines indicate effective relaxation times (assuming constant E=100 GPa). Depending on chosen composition, a wide range of relaxation times are plausible at each reservoir depth.

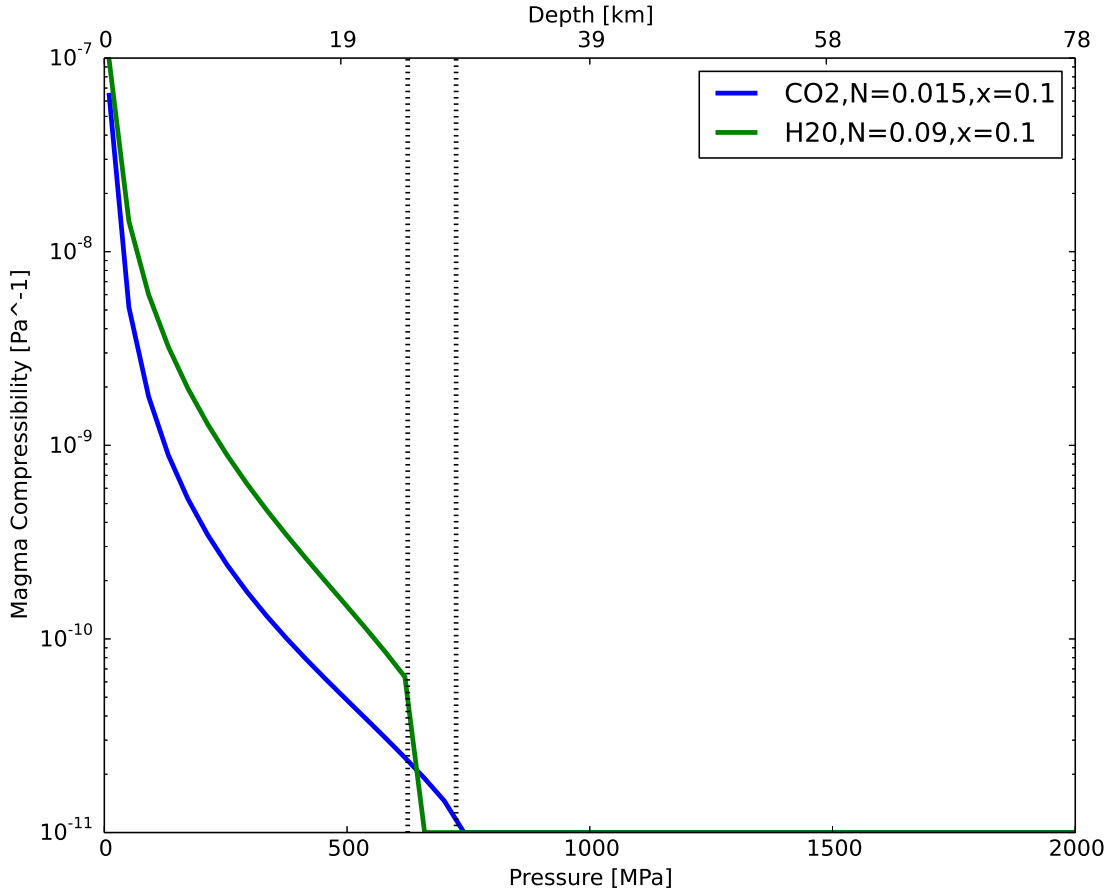

Figure 3.17: Magma compressibility versus depth calculated by equation 3.3 for H_2 and CO_2. For CO_2, initial volatile content is 1.5 wt%, with a solid crystal fraction of 0.1. For H_2, initial volatile content is 9 wt% with solid fraction of 0.1. Saturation depth (indicated by vertical dashed lines is predicted to occur in the mid crust, unsaturated compressibility is set to a value of 10^{-11} Pa^{-1}.

Track	Beam	Pairs	Dates	θ_{min}	θ_{max}	θ_{mean}	α_{mean}
282	2	429	72	18.2	27.3	22.8	-167.7
10	2	107	39	15.8	24.5	20.2	-167.5
3	2	15	22	16.1	23.9	20.0	-13.6
89	6	73	20	38.9	43.3	41.1	-13.0
			ϵ_x	ϵ_y	ϵ_z		
			1.8	20.4	2.2		

Table 3.1: Following conventions in *Wright et al.* (2004b), θ corresponds to incidence angle (measure from vertical direction on the ground surface to the radar line-of-sight vector), α corresponds to satellite heading (counter-clockwise from north), dilution of precision for east-west, north-south, and vertical components for mean viewing angles in this table are given as ϵ_x, ϵ_y, ϵ_z, respectively. ϵ_y=20.4 indicates line of sight uncertainties of 1 line-of-sight unit get mapped to 20.4 unit uncertainties in the inverted north-south displacement vector.

Station	Latitude	Longitude	Altitude [m]	Start	Stop	V_{EW}	V_{NS}	V_Z
UTUR	-22.242	-67.206	5184.079	2010/04/15	2014/03/14	15.5	13.4	3.0
COLO	-22.167	-67.804	4376.913	2010/04/14	2014/07/11	17.0	14.0	-0.1
QUET	-22.198	-67.343	4270.762	2011/03/11	2010/04/16	17.7	10.2	20.7

Table 3.2: Continuous GPS stations at Uturuncu. Rates [mm/yr] are calculated from least squares regression of daily solutions in IGS08 reference frame without removing a seasonal signal. Data has been processed by the University of Nevada Geodetic Laboratory (*Blewitt et al.*, 2013)

Rock type	Saturation	log10(A) [$\mathrm{MPa^{-n}s^{-1}}$]	n	Q [$\mathrm{kJmol^{-1}}$]	reference
quartzite	wet	-3.7	1.9	137	(*Babeyko et al.*, 2002)[a]
granite	?	-5.2	2.4	156	(*Babeyko et al.*, 2002)
granite	intermediate	-5.0	2.6	160	(*Fialko and Pearse*, 2012)[b]
diorite	wet	-1.4	2.4	219	(*Hansen and Carter*, 1982)

Table 3.3: Laboratory-derived powerlaw parameters used in this study, with original references.

[a] The authors take values from Table 1 in (*Ranalli and Murphy*, 1987); however, original references are not cited.

[b] The authors average values for dry and wet westerly granite from Table 4 in (*Carter and Tsenn*, 1987), which are originally from (*Hansen and Carter*, 1983).

CHAPTER 4

INFLUENCE OF CRUSTAL STRUCTURE ON ACTIVE SILL INFLATION AT LAZUFRE VOLCANIC CENTER

4.1 Introduction

The "Lazufre" volcanic uplift signal is situated between the Holocene edifices Lastarria and Cordon del Azufre in the Central Andes Volcanic Zone (*Pritchard and Simons*, 2002). The deformation footprint at Lazufre is often compared to uplift at Uturuncu Volcano approximately 300km to the north. Both signals are unique globally in that they exhibit very broad (>50 km) uplift on the order of 1 cm/yr for at least 15 years. However, the proposed causes of uplift at these centers are very distinct: Lazufre has been modeled as an opening sill at 10 km depth (e.g. *Pritchard and Simons*, 2004; *Ruch et al.*, 2008; *Remy et al.*, 2014), whereas Uturuncu deformation may be caused by vertical ascent of magma (Chapter 3), or diapiric ascent in the mid crust (*Fialko and Pearse*, 2012). This discrepancy arises principally from subtle differences in the spatial pattern of deformation at the two locations: At Uturuncu, a low amplitude 'moat' of subsidence has been observed around a remarkably circular uplift footprint; while at Lazufre there is no evidence of peripheral subsidence and the uplift pattern is slightly elliptical.

The center of deformation at Lazufre is offset approximately 10 km between the summits of the two Holocene edifices (Figure 4.1) and has been interpreted to be caused by a opening of a magmatic sill at 10 km depth. Although the last eruptions of Lastarria and Cordon del Azufre are uncertain (*Siebert et al.*, 2011), evidence for magmatic activity is considerable (*Naranjo*, 1992). In partic-

ular, localized uplift of the edifice of Lastarria Volcano and vigorous fumerolic output of Lastarria has prompted an association between the deep magmatic inflation and persistent hydrothermal activity (*Froger et al.*, 2007). Furthermore, geochemical analysis of the multiple fumarole fields on the edifice of Lastarria (*Aguilera et al.*, 2011), and measurements of the gas plume (*Tamburello et al.*, 2014) show evidence for shallow magmatic fluids.

In this study we present up-to-date InSAR observations, and measurements from recent continuous and campaign GPS surveys, extending observations through 10/2014. To date, models of sill opening at Lazufre have been restricted to the major assumption of a homogeneous crust. In this paper we incorporate local seismic tomography into a three dimensional heterogeneous finite element model to quantify the effects of heterogeneous upper crustal material properties on sill opening.

4.2 Previous Models

Most models of deformation at Lazufre have been constrained by a single viewing geometry, utilizing data from ERS and Envisat tracks 282 data spanning 07/1995 to 01/2008 (*Pritchard and Simons*, 2004; *Froger et al.*, 2007; *Ruch et al.*, 2008, 2009). All models suggest the source reservoir is either an oblate ellipsoid (a:b $\approx$ 10:1) or a rectangular sill-like body with a northerly strike (0-25° E of N) and slight dip to the east (0-10° E). More recently, independent InSAR viewing geometries were used to constrain the best-fit source at a depth (to middle) of 8 km, a:b $\approx$ 3:2, strike of 10° and dip of 10° with an associated volume change of 0.3 km^3/yr (*Pearse and Lundgren*, 2013). The same dataset was processed and

modeled with different methodologies (*Remy et al.*, 2014), and the best-fit results for all studies are compared in Table 4.5. In addition to geodetic modeling, a recent study utilizing magnetotelluric data reveals a strong conductor under the deformation anomaly dipping eastward to the base of the crust: Modeling of the conductivity suggests the feature could be due to 5-8 vol% partial melt which is feeding current sill-inflation in the upper crust (*Budach et al.*, 2013). The crustal thickness in this region is at approximately 60 km depth (*Wölbern et al.*, 2009).

4.3 New InSAR observations

Here we present new data that extends observations through 09/2014. We processed data from the Environmental Satellite (ENVISAT), Advanced Land Observation Satellite-1 (ALOS-1), and TerraSARX Satellite (TSX) with ROI_PAC 3.0.1 software (*Rosen et al.*, 2004). COSMO-SkyMed Satellite (CSK) data was processed with ISCE 1.5 software (*Rosen et al.*, 2012). For all datasets we removed the topographic signal with the SRTM V3.0 data obtained via NASA LPDAAC. For ALOS, TSX and Envisat we used 90m resolution topography (SRTMGL3), and CSK processing utilized the recently released 30m native resolution data (SRTMGL1). Both resolutions have all voids removed by either interpolation or filling with Advanced Spaceborne Thermal Emission and Reflection Radiometer (ASTER) GDEM measurements.

4.3.1 Envisat

All available ERS and Envisat stripmap data between 1995 and 2010 (tracks 282, 318, and 404) have been described in previous studies (*Ruch et al.*, 2009; *Pearse and Lundgren*, 2013; *Remy et al.*, 2014). One additional track has not been reported (track 53), however it is of limited use because it only covers a small portion of the deformation field and has less than 10 combinable dates. There is a large amount of Envisat ScanSAR ("wide swath") data available that has also been largely overlooked. In this specialized mode, Envisat pans through stripmap beams 2 through 6, creating a large footprint image (400x400km) with ground resolution ranging between 20 to 100m (e.g. *Guccione*, 2006). This data is valuable because it provides an additional ascending viewing geometry that captures the complete deformation field.

Generation of wide swath interferograms requires specialized software that only became freely available recently (*Liang et al.*, 2013). Furthermore, adequate radar burst alignment required to generate interferograms was implemented in September 2007, so success rate of forming interferograms is poor prior to that date (e.g. *Ortiz and Zebker*, 2007). We note that the burst alignment may vary significantly between subswaths such that even if generation of a full wide swath interferogram fails, it is possible to work only with the subswath containing a target of interest. An alternative strategy to utilize wide swath data is to extract an individual subswath of data and combine it with co-located stripmap mode acquisition, thereby overcoming the requirement of burst alignment (e.g. *Pepe et al.*, 2011). This approach has been implemented at Uturuncu Volcano for track 89 and resulted in a timeseries of observations with roughly double the number of stripmap dates (*Fialko and Pearse*, 2012).

At Lazufre, ascending wide swath tracks 89 and 361 contain 23 and 29 dates respectively spanning 09/2003 to 11/2009. Unfortunately the subswaths containing Lazufre do not coincide with stripmap acquisitions. *Anderssohn et al.* (2009) successfully generated seven wide swath interferograms, but found only one (09/22/2003 - 04/24/2006) with sufficient signal to noise to utilize in modeling. For comparison, we processed the same wide swath interferogram with the ROI_PAC processor from *Liang et al.* (2013) (Figure 4.3).

4.3.2 ALOS

There are 16 ALOS acquisitions between 2007/02/09 and 2011/02/20, providing additional observations towards the end of the Envisat mission. Unfortunately, many of these dates show strong ionospheric signals, which have been noted in other regional studies (e.g. *Fournier et al.*, 2010; *Henderson and Pritchard*, 2013). Because the PALSAR instrument on ALOS uses L-band (24 cm wavelength), a longer elapsed time is necessary to image cm/yr signals compared to C-band. We stacked 20 successful interferograms and found that the spatial and temporal patterns of deformation are in agreement with previous datasets.

4.3.3 CosmoSkyMed

We generated stacks of CSK data using two ascending and descending satellite passes. Due to a change in incidence angle and polarization in 2012, we are unable to create stacks from a single set of interferograms. Instead, we divided acquisitions into two sets before and after 05/2012 (see Table 4.1). The four

stacks of CSK data are shown in Figure 4.4.

4.3.4 TSX

TerraSARX provides X-band (3.1 cm wavelength) observations of Lazufre from three unique viewing angles. Unfortunately, the smaller footprint of TSX Stripmap acquisitions results in only partial coverage of the complete uplift footprint. Observations with TSX began in 04/2008 and most recently occurred on 09/2014 (see Table 4.1). We note that successful TSX processing required a beta version of upcoming ROI_PAC software 3.1, and SRTM data that was interpolated to 30m per pixel. Select interferograms using TSX data are shown in Figure 4.5.

4.4 GPS Observations

4.4.1 Continuous GPS

We installed three continuous GPS stations intended to monitor volcanic deformation at Lazufre. Station locations and measured component velocities are listed in Table 4.2. Continuous stations were installed only within the country of Chile, and consequently measurements are limited to the Western side of the deformation footprint. Station LCEN was intended to get as close as possible to the center of deformation, LLST was installed on the edifice of Lastarria Volcano, and SOCM was intended as a far-field reference station at approximately equal longitude compared to the other stations. Timeseries data for LCEN is

shown in Figure 4.6 and timeseries data for LLST is shown in Figure 4.7.

4.4.2 Campaign GPS

We supplemented continuous measurements with a campaign survey, installing 10 benchmarks with locations listed in Table 4.3. Two campaigns were conducted during the weeks of 11/14/2012 and 03/20/2014. Benchmarks were occupied with campaign GPS receivers for two to three days. Analysis of this dataset is ongoing, but preliminary determinations of vertical displacements are consistent with InSAR measurements (Table 4.3).

4.4.3 Non-volcanic signals

Isolation of the volcanic inflation signal requires removal of interseismic displacements and seasonal loading displacements. In order to estimate the tectonic signal from interseismic deformation at the instruments we installed, we compiled data from regional campaign GPS surveys published in (*Métois et al.*, 2012, 2013, 2014). Results are shown in figures 4.8 and 4.9. It is clear that both north-south and east-west interseismic displacements are expected at rates greater than 10 mm/yr. Few stations beyond 200km from the trench require an extrapolated estimate of vertical interseismic displacements. However, a generous upper bound estimate would be less than 5 mm/yr. Preliminary estimation of expected seasonal oscillation amplitude with GRACE data also suggests as much as 5 mm of vertical displacements within the survey region.

4.5 Finite Element Model

In order to evaluate the role of crustal heterogeneity on surface uplift we constructed a finite element model using PyLith software. We use a rectangular mesh with a horizontal (dip=0) sill-like reservoir located at 10 km depth. An isometric view of the mesh with sill opening and surface displacements is shown in Figure 4.13. All nodes along the 10 km depth slide can be assigned an initial displacement or traction boundary condition, so that we can test rectangular sill geometries of various lengths and widths. Although most studies suggest a strike of $> 20^{\circ}$ degrees east of north, we keep a strike of zero for mesh simplicity and note that solutions can simply be rotated by $> 20^{\circ}$ degrees. The model domain, 200x200x100 km, is sufficiently large to utilize zero-displacement boundary conditions, and we utilize an element length scale of 2km, which results in 500,000 elements within the entire domain.

4.5.1 Benchmark

To validate the implementation of our finite element model, we compared solutions for a sill opening with the solution for a rectangular dislocation in an elastic half-space (*Okada*, 1985, 1992). Surprisingly, the analytic solution of Okada is independent of material parameters for the special case of a horizontal fault. In other words, a rectangular sill opening one meter should produce the same surface displacement whether it is embedded in rock, cork, or rubber! This does not hold true for the finite element model due to the requirement of having displacements at the edges of the sill taper to zero. For example, for the simplest initial condition of opening at a single node, the dislocation takes on a pyra-

midal shape that has a base length of twice the element size. Opening more closely approximates the analytical rectangular dislocation geometry of *Okada* (1985) as the mesh is refined and more nodes within the sill area are prescribed displacements (Figure 4.15).

We refer to analytic solutions as a 'point sill' if the sill horizontal dimensions are much less than its depth (e.g. $< 1/5$). It is worth noting that *Pritchard and Simons* (2004) performed an inversion of descending InSAR data to determine a point sill of 1 km radius at 18 km depth. In general, finite sources with distributed opening patches in a plane result in depth determinations that are closer to the surface (e.g. (e.g. *Pearse and Lundgren*, 2013; *Remy et al.*, 2014). Performing a convergence test we find that a cell size of 2 km provides sufficient agreement with the benchmark solution and has the benefit of reduced computational time (Figure 4.14). Finally, we remark that a 10x10km sill opening of 10 cm/yr is able to match observations of 3 cm/yr maximum uplift.

4.5.2 Assignment of material properties

In order to add realistic heterogeneous elastic properties to the finite element model, local seismic tomography is required. Recently, a regional ($12 - 42°$S) Ambient Noise Tomography (ANT) dataset became available that covers the Lazufre region (*Ward et al.*, 2013). This analysis utilized 330 broadband stations throughout South America operating at different times over the period May 1994 to August 2012, and provides a model of V_{sv} velocities to a depth of 50km (10km horizontal resolution and 1km vertical resolution). We present a depth-averaged profile of this model to give a first order comparison to homogeneous

half-space values in Figure 4.11.

It is important to note that the ANT technique is insensitive to possible sharp impedance contrasts evidenced by preliminary receiver function analysis (*McFarlin et al.*, 2014). A joint inversion for a Vs velocity model that combined ANT and receiver functions at Uturuncu Volcano (300km North) led to a significant changes in the 3D subsurface velocity field (*Ward et al.*, 2014). In general, we suspect the inclusion of local receiver functions at Lazufre may reduce velocities in the mid crust and 'narrow' the vertical spread in low velocities.

We also utilized the preliminary result from *Spica et al.*, who independently calculated a Vs velocity model centered on Lastarria Volcano using seismic data from 8 stations (6 broadband, 2 intermediate period) from January to March 2012, in addition to a densified local network consisting of 18 stations (17 broadband, 1 short period) between February and March 2008. The tomographic model produced from this analysis has a smaller spatial extent compared to that of *Ward et al.* (2013), but higher resolution (100m sided cells). We present a depth-averaged profile of this model to give a first order comparison to others discussed so far 4.12, and a map view depicting the extents of these datasets in Figure 4.10.

The final step in converting tomographic models into elastic material parameters requires assuming a relationship between Vp, Vs, and density. Often, a constant Vp/Vs ratio is used, because the assumption of Poissonian material ($\nu = 0.25$) requires that Vp/Vs=1.732. Alternatively, empirical relations derived from field studies and laboratory experiments can be used to obtain both Vp and density, for example at Mt. Etna (*Currenti et al.*, 2007). We use the empirical equations of *Brocher* (2005) to obtain the elastic material constants that represent

the crust in out finite element model.

4.6 Discussion

4.6.1 1D Layered Model

Depth-averaged velocity models, though a simplification of the true 3D variation, provide a simple assessment off the effect of material property variation with depth. Indeed, the tomographic model of *Ward et al.* (2013) contains predominantly 1D variation with depth (Figure 4.11). For the same 10cm of opening on a 10x10km sill at 10km depth, this heterogeneity causes a subtle 1.7% increase in maximum vertical displacement and 3.5% increase in maximum radial displacement (Figure 4.16). Because these changes are very small, no modification to source depth or sill opening is warranted.

4.6.2 3D Heterogeneous Model

To first order, the large footprint of deformation at Lazufre is oblate and smoothly varying over a length scale of 10 km. We therefore do not anticipate large amplitude anomalies in crustal mechanical properties less than several kilometers. Nevertheless, we utilize the 3D tomographic dataset from *Spica et al.* in order to quantify the effect of this model for surface displacements. We again utilize the FEM domain with a 10x10km sill at 10km depth and an opening of 10cm/yr. We find that vertical displacements are amplified by up to 6.6% and radial displacements are increased by up to 4.9% (Figure 4.16). The variations

in displacements are mostly constricted to within 10km of the uplift source, beyond which surface displacements are indistinguishable for the three domains tested: homogeneous halfspace, 1D heterogeneity, and 3D heterogeneity.

4.7 Conclusion

We have demonstrated that deformation at Lazufre continues past 2010 until the present (12/2014). Both spatial and temporal patterns appear consistent with previous datasets, suggesting ongoing sill inflation in the upper crust. Campaign and continuous GPS data are consistent with InSAR measurements, providing cross-validation of these geodetic measurements. Finally, we presented a finite element model to evaluate the effect of new 3D velocity models on surface displacements. Results indicate that proposed subsurface heterogeneity from seismic tomography increases the surface displacements for homogeneous crust by less than 7% within a 10km radius of the center of uplift.

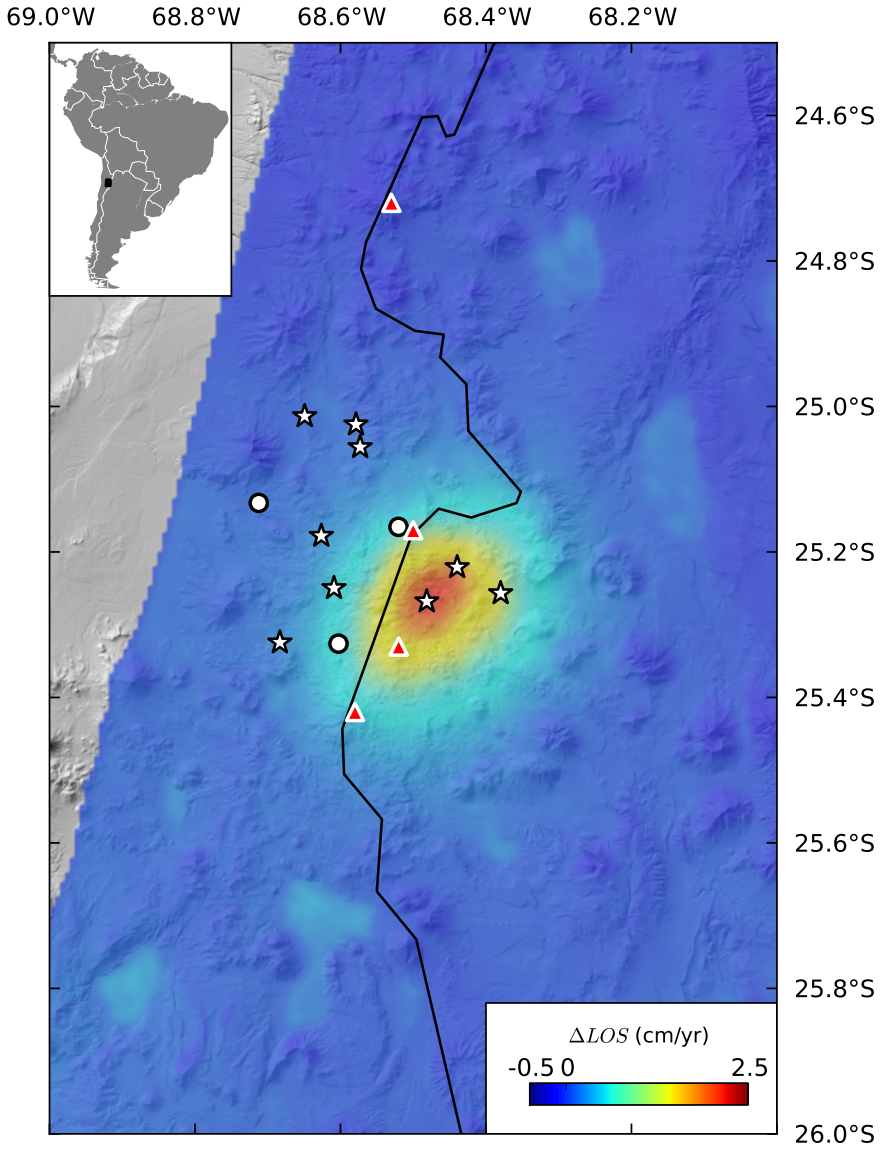

Figure 4.1: Overview map of Lazufre and GPS Survey. White circles are continuous GPS sites, White stars are campaign GPS (for exact locations see Table 4.3). Note that the western-most continuous GPS site was vandalized and is not further reported. Red triangles are active volcanoes from (*Venske et al.*, 2014). InSAR data shown is a stack of Envisat track 282 data from *Henderson and Pritchard* (2013).

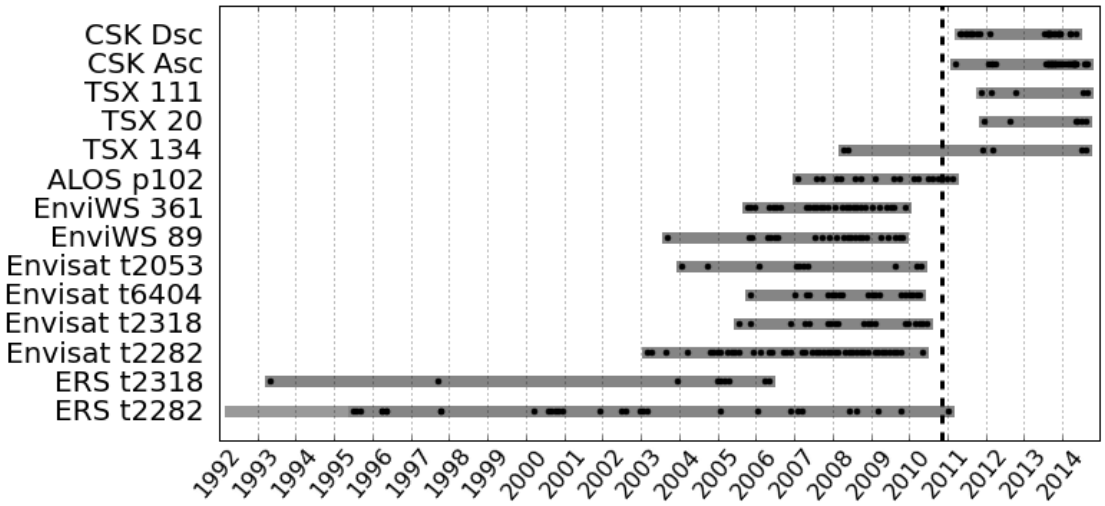

Figure 4.2: Timeline of InSAR data at Lazufre. Dots represent acquisitions used in forming interferograms. Gray bars represent the span from earliest to latest acquisition (not necessarily usable in forming interferograms). The dashed vertical line corresponds to the installation of local continuous GPS sites LLST and LCEN.

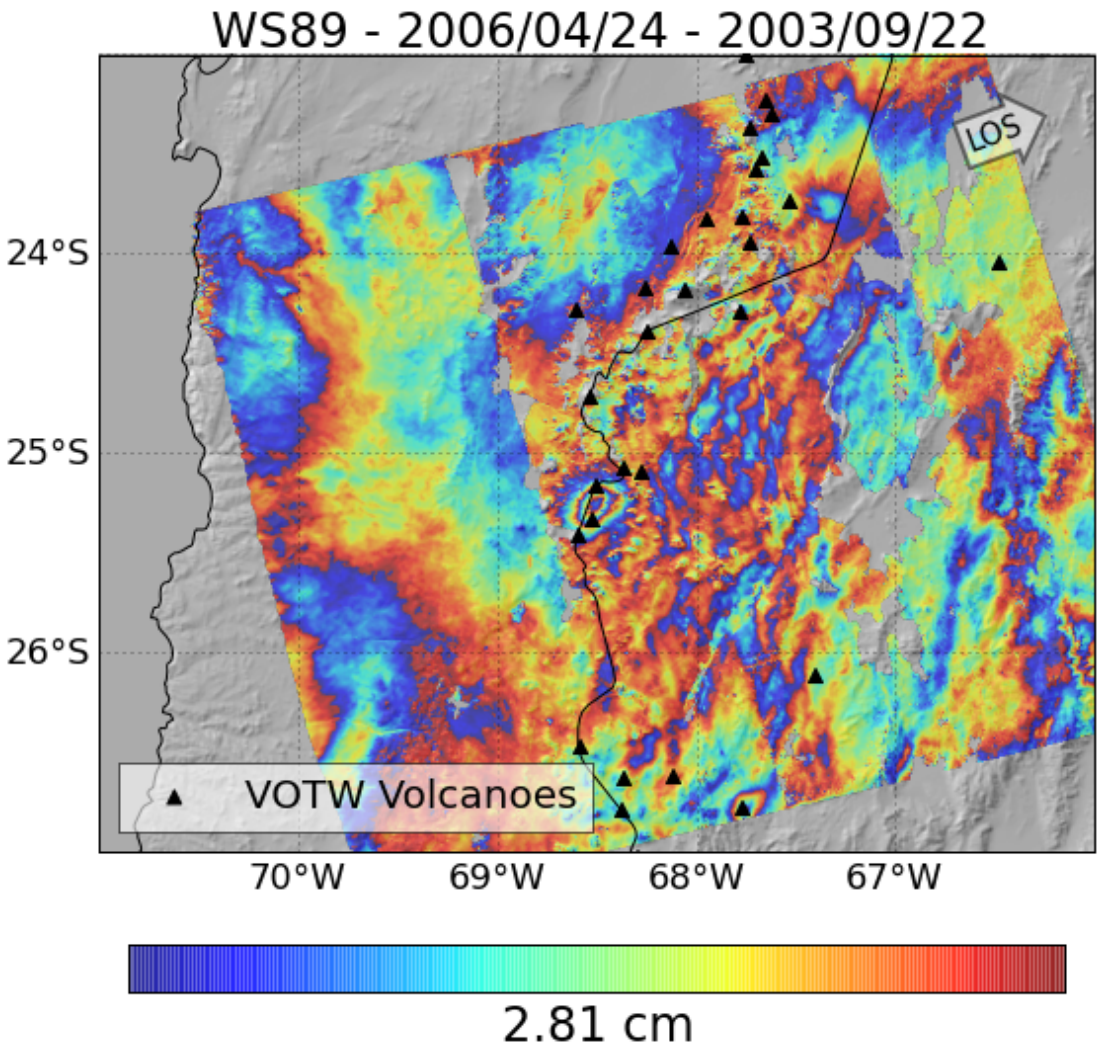

Figure 4.3: Ascending Envisat ScanSAR Interferogram from track 89. Displacements are presented as wrapped values where each color fringe cycle corresponds to 2.81 cm of deformation (half radar wavelength). Black triangles represent active volcanoes. Uplift is clearly seen at Lazufre, displacements are also apparent at Cerro Blanco to the south and Cerro Overo to the northeast.

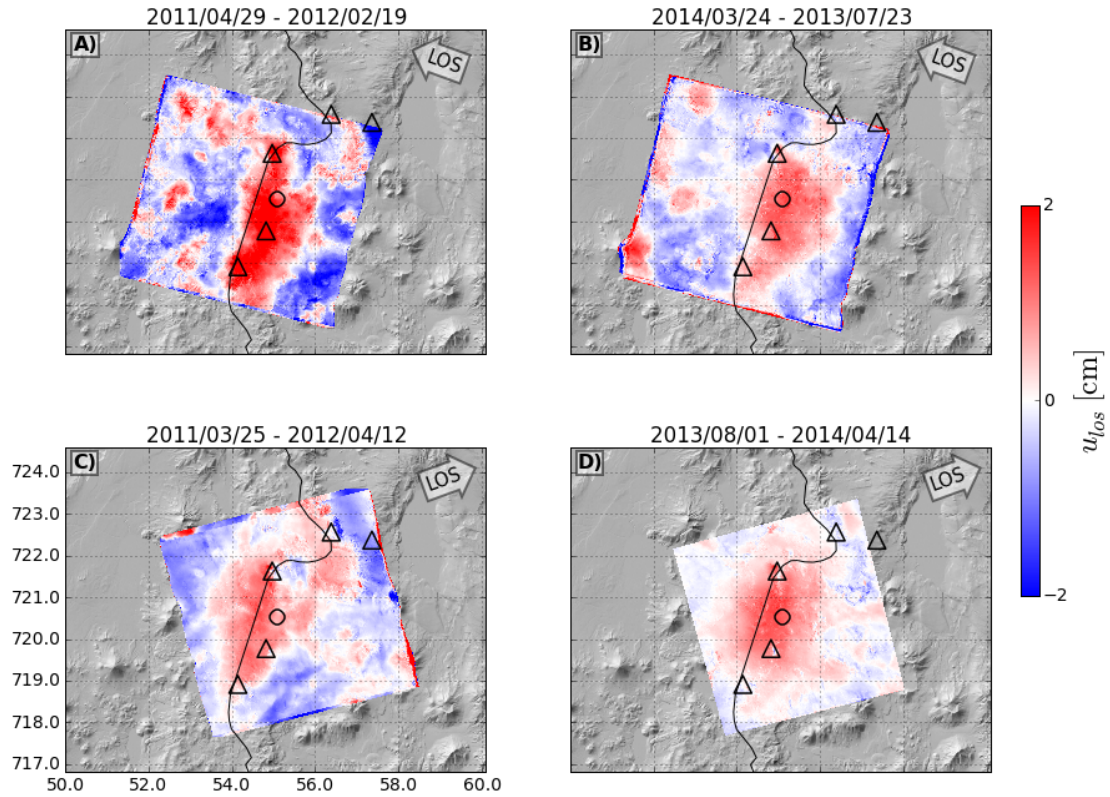

Figure 4.4: Stacks of CosmoSkyMed data over Lazufre. The number of dates and interferograms in each stack is listed in Table 4.1. A) and B) correspond to descending data, while C) and D) correspond to ascending data. Black triangles represent active volcanoes, the black circle represents the modeled centroid of vertical uplift from inSAR data spanning 03/2003 and 05/2010 (*Remy et al.*, 2014). While considerable atmospheric noise is present, the anticipated uplift pattern is emergent in each panel. Coordinates are UTM 19S.

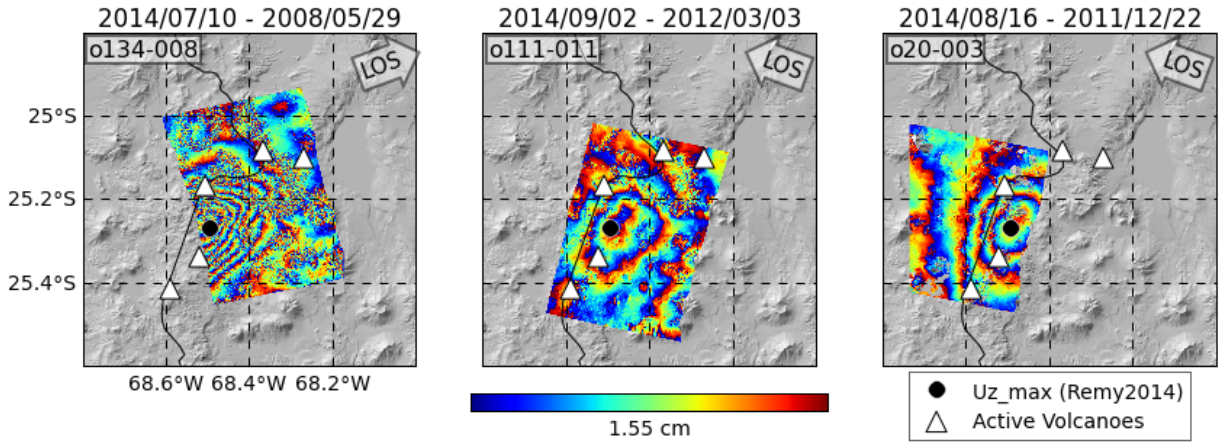

Figure 4.5: TerraSAR-X Interferograms at Lazufre with three distinct viewing geometries (labelled in upper left of each panel). Each fringe corresponds to 1.55 cm of uplift in radar line-of-sight (see Table 4.1). For comparison, the black dot represents the modeled centroid of vertical uplift from inSAR data spanning 03/2003 and 05/2010 (*Remy et al.*, 2014). White triangles are active volcanoes. The solid black line depicts the border between Chile and Argentina.

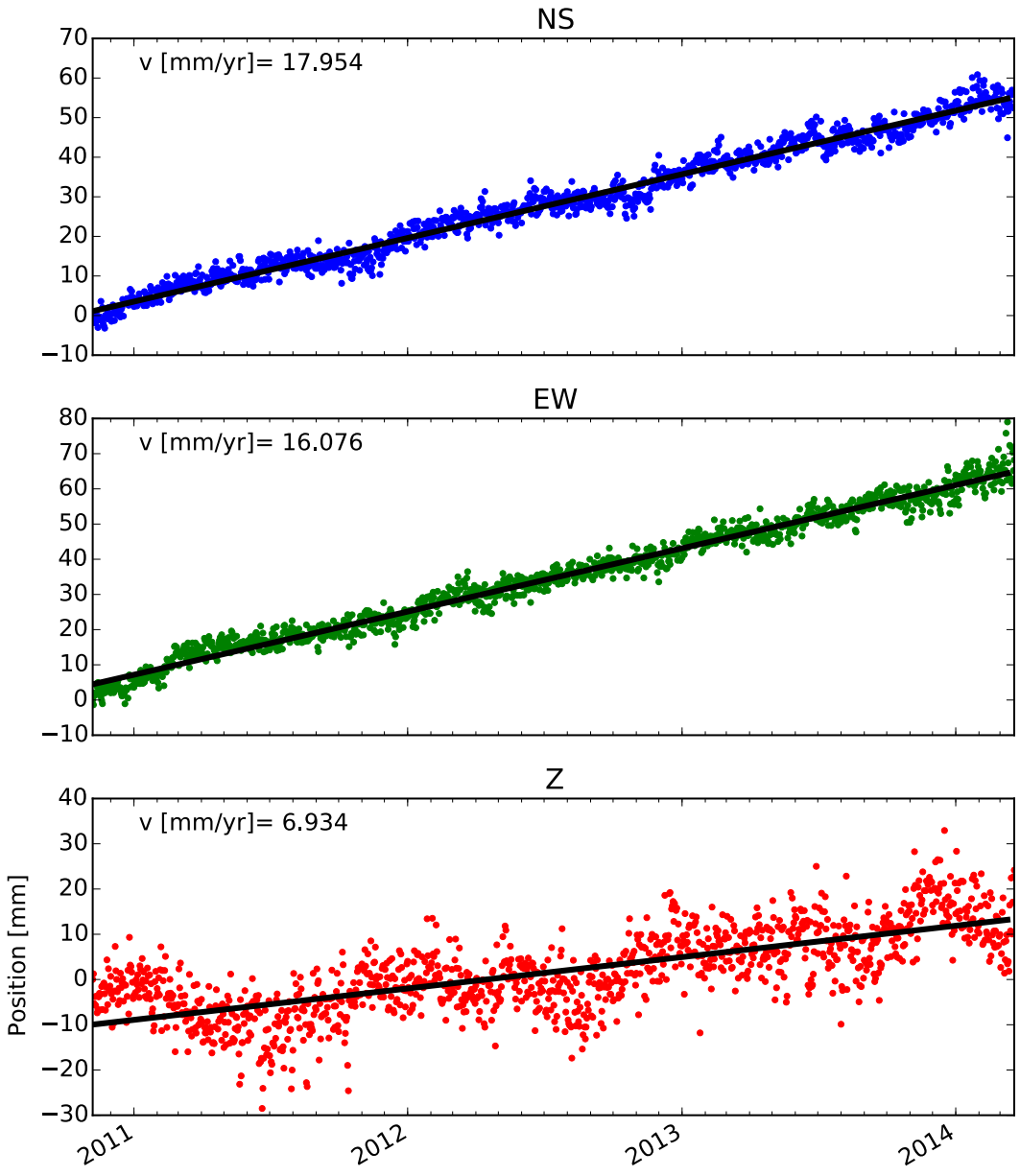

Figure 4.6: LCEN station timeseries. Rates [mm/yr] are calculated from least squares regression of daily IGS08 positions without removing a seasonal signal. Data has been processed by the University of Nevada Geodetic Laboratory (*Blewitt et al.*, 2013).

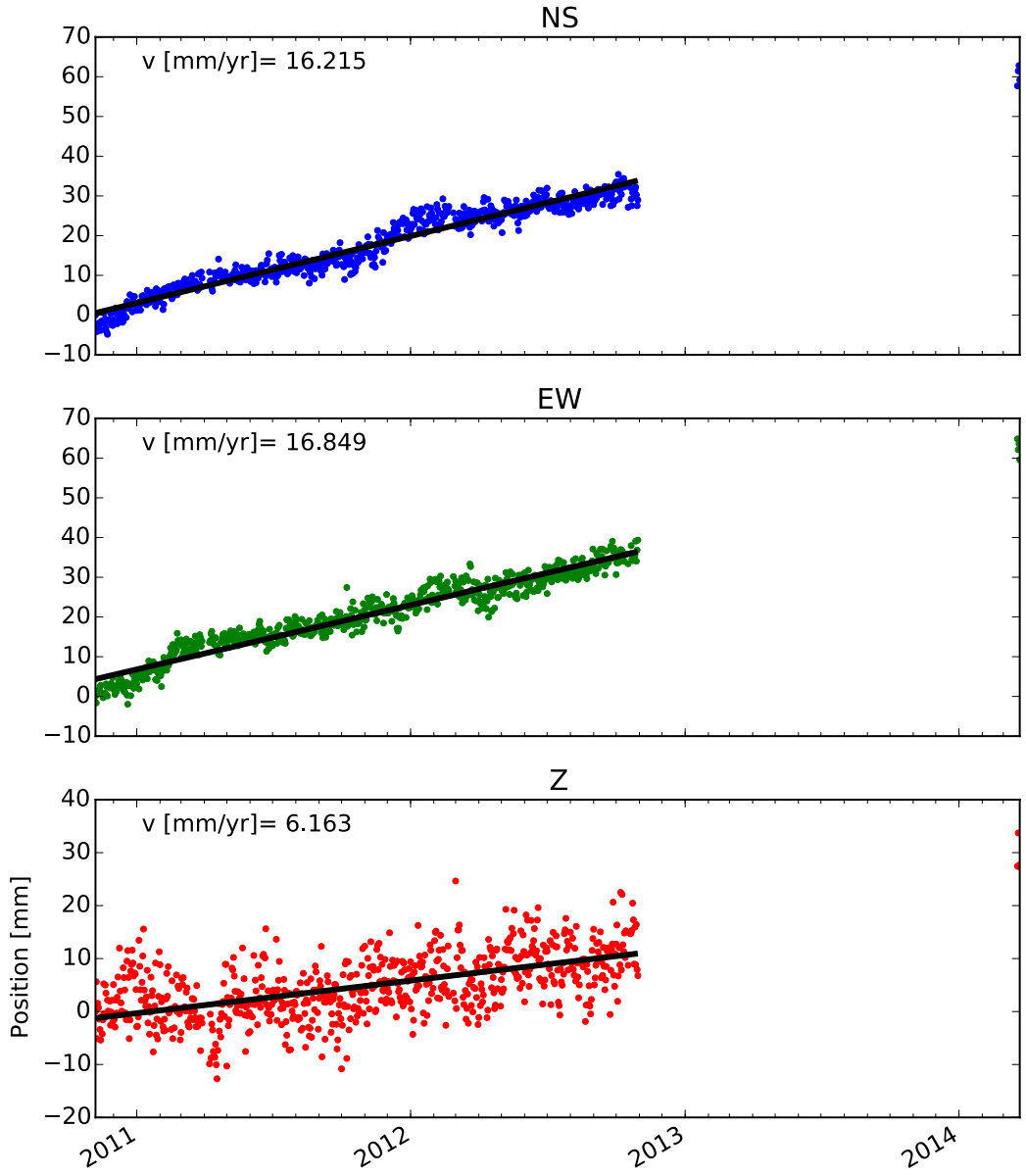

Figure 4.7: LLST station timeseries. Rates [mm/yr] are calculated from least squares regression of daily IGS08 positions without removing a seasonal signal. Data has been processed by the University of Nevada Geodetic Laboratory (*Blewitt et al.*, 2013). The large data gap is due to a missing receiver that was replaced on 03/20/2014, for which three days of data are shown in the upper right corner of each plot.

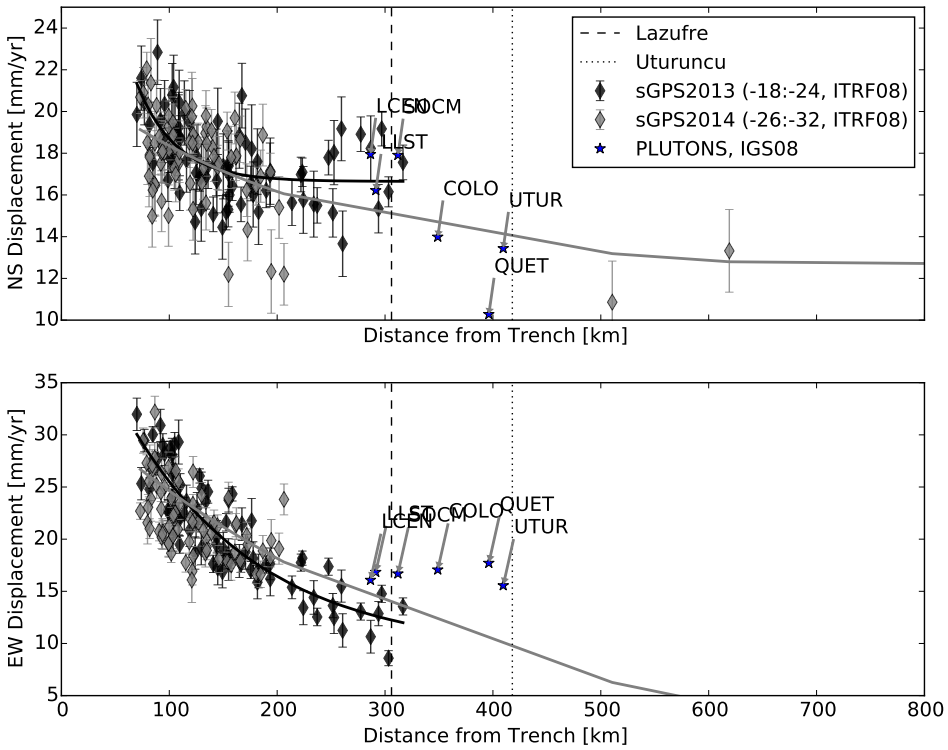

Figure 4.8: Horizontal interseismic velocity from campaign GPS presented in *Métois et al.* (2013, 2014). Discrepancies between PLUTONS continuous stations (blue stars) are expected due to differences in processing and reference frame; however, plot gives first order prediction of northward and eastward motion of stations due to interseismic deformation.

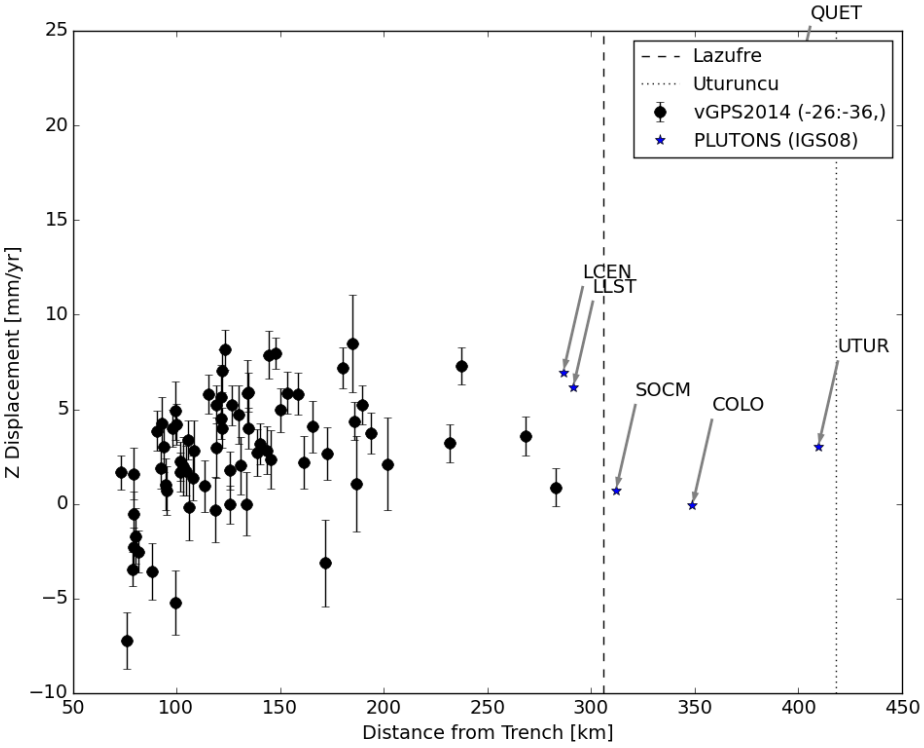

Figure 4.9: Vertical interseismic velocity from campaign GPS presented *Métois et al.* (2013, 2014). Black points have been processed in the NUVEL-1A-NNR reference frame, whereas PLUTONS continuous station vertical velocities are processed in the IGS08 reference frame. From this plot we predict that absolute vertical displacements eastward of Lazufre (300 km from the trench) are less than 5 mm/yr.

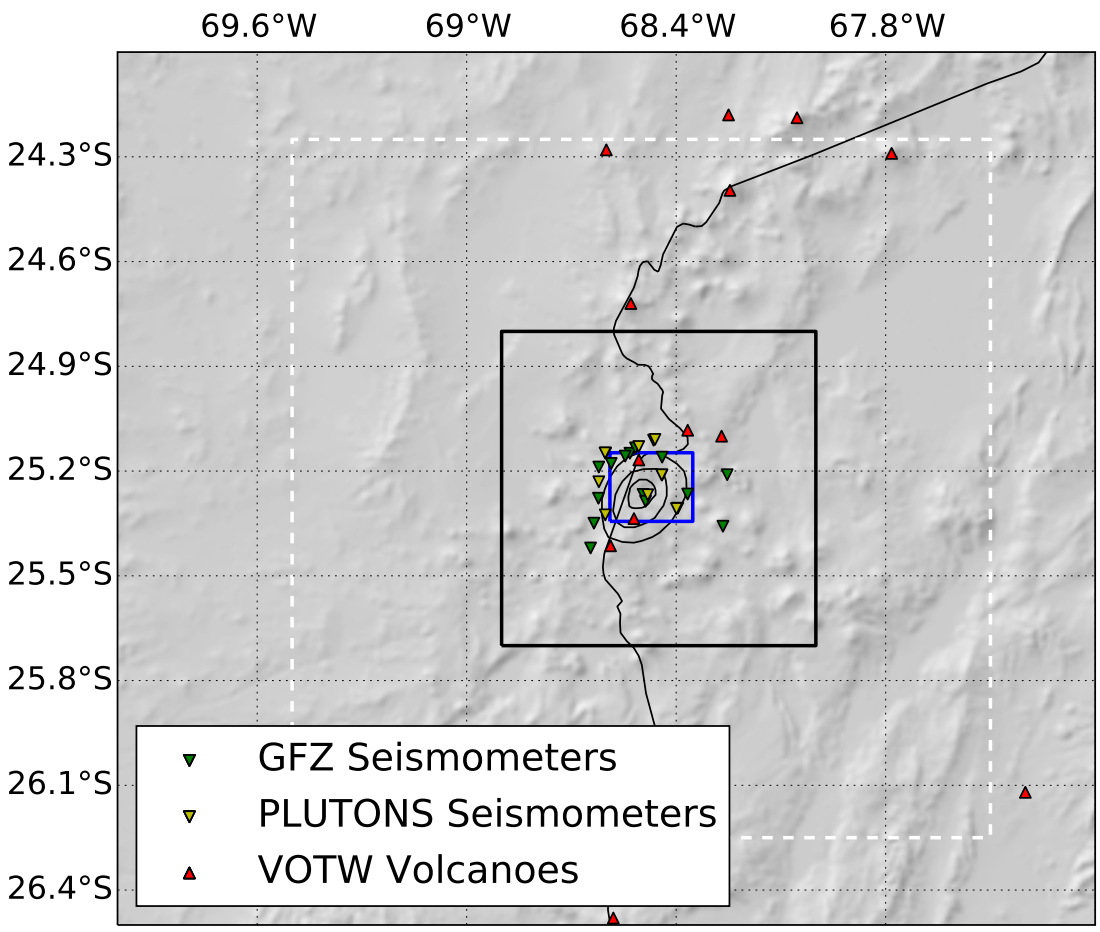

Figure 4.10: Overview map of Lazufre with seismic tomography and FEM extents. FEM areal extent represented by white dashed rectangle, tomography extracted from *Ward et al.* (2013) as black solid rectangle, and tomography from *Spica et al.* as blue solid rectangle. Thin black line is the international border between Chile and Argentina. Red triangles are active Holocene volcanoes, green inverted triangles are seismic stations from the GFZ array and yellow inverted triangles are stations from the PLUTONS seismic array.

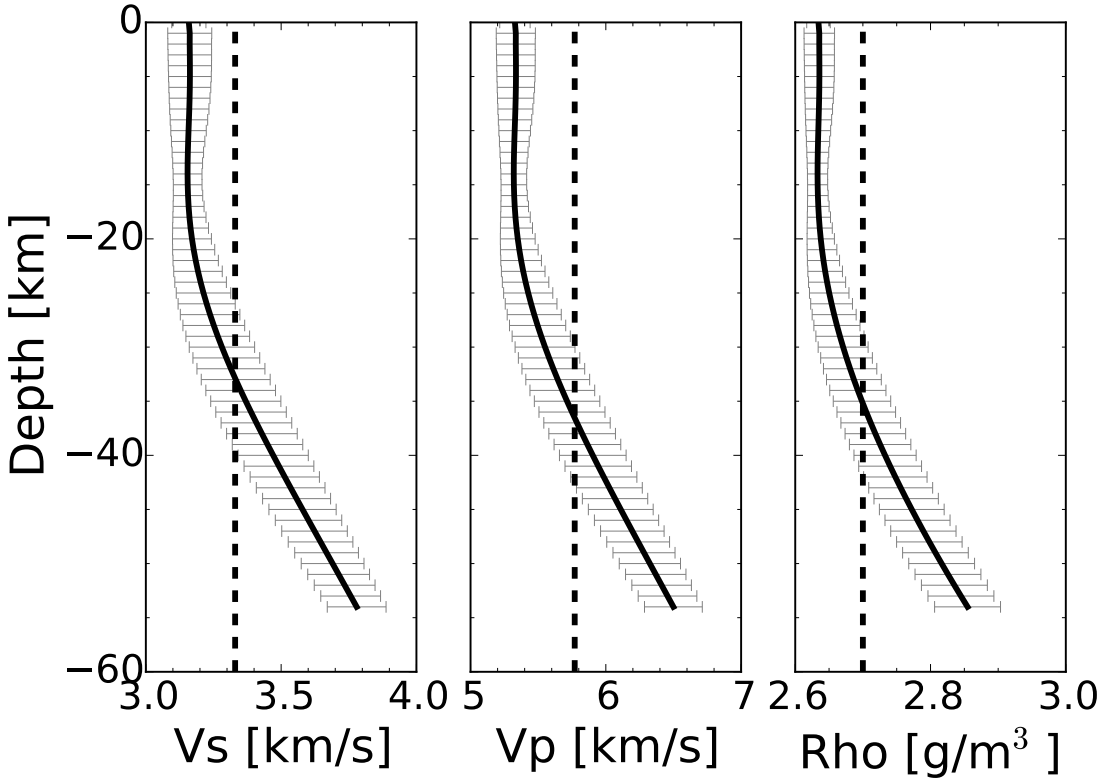

Figure 4.11: Depth-averaged tomography velocity model for Lazufre for a 50x50km square around the uplift centroid extracted from *Ward et al.* (2013). Solid black line represents mean velocities with depth, gray horizontal bars represent one standard deviation. Dashed vertical line represents assumption for homogeneous material used in modeling (*Del Negro et al.*, 2009).

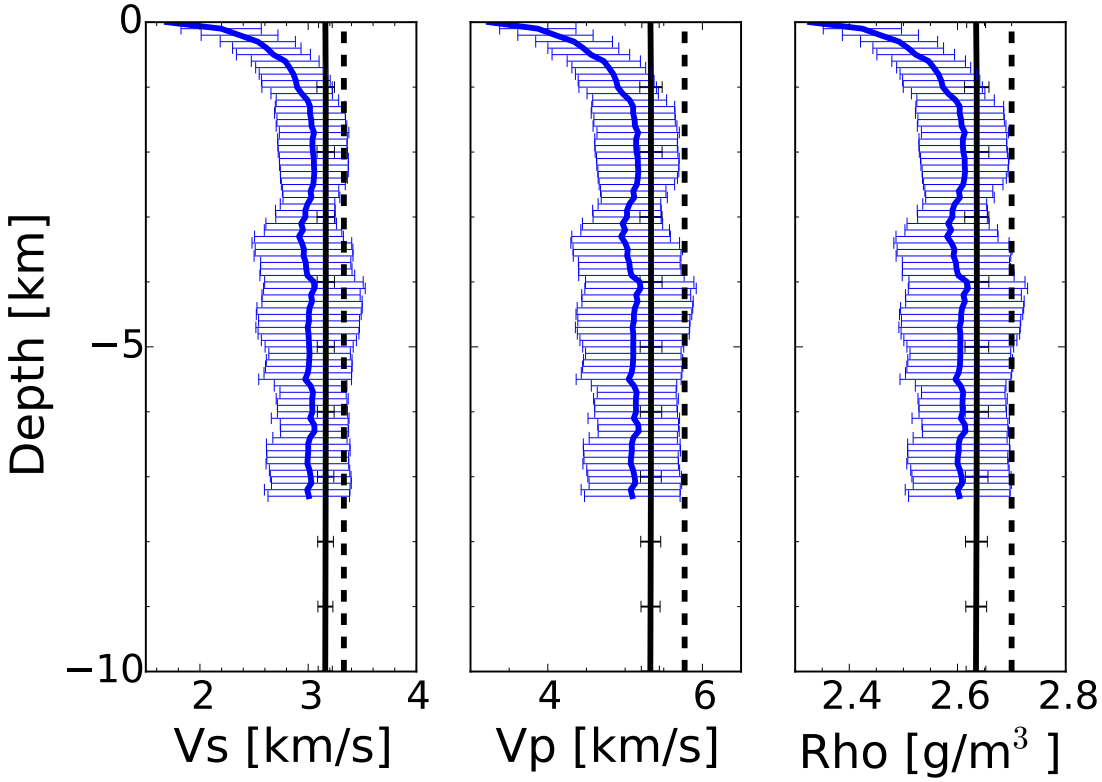

Figure 4.12: Depth-averaged tomography velocity model for Lazufre. Blue line represents mean velocity for an approximately 10x10km square around the uplift Lastarria after *Spica et al.*. Solid black line represents mean velocities with depth, gray horizontal bars represent one standard deviation. Dashed vertical line represents assumption for homogeneous material used in modeling(*Del Negro et al.*, 2009).

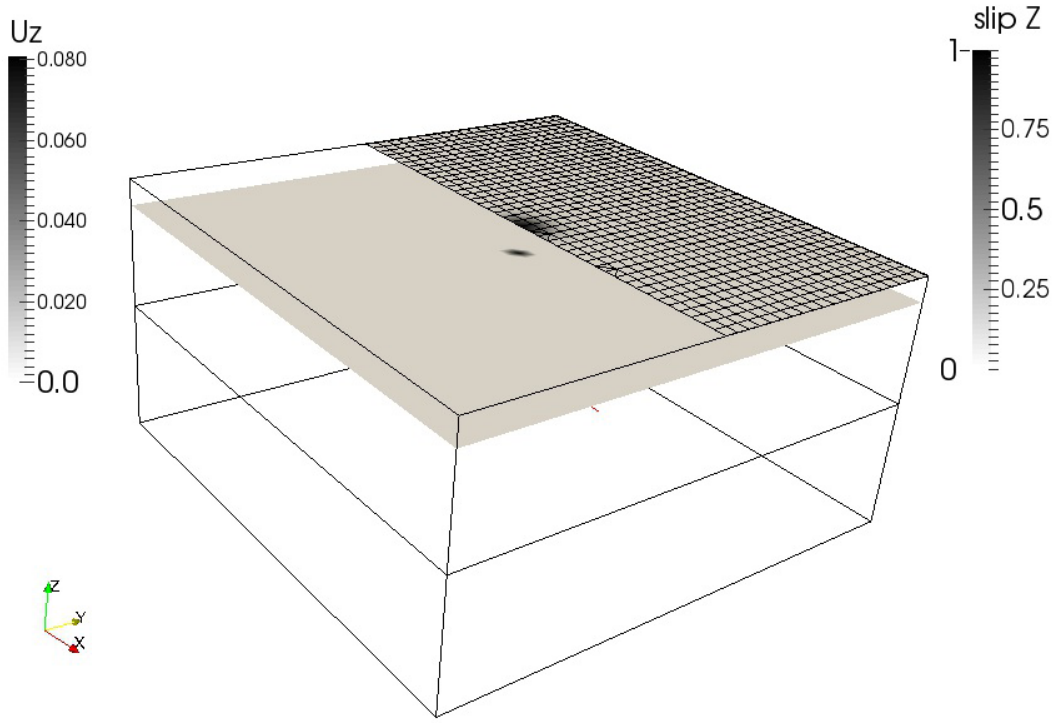

Figure 4.13: Isometric schematic of FEM mesh (200x200x100km) with 'point' sill opening at 10km depth. Note different color scales for sill opening and surface displacements. Half of surface is shown with element edges.

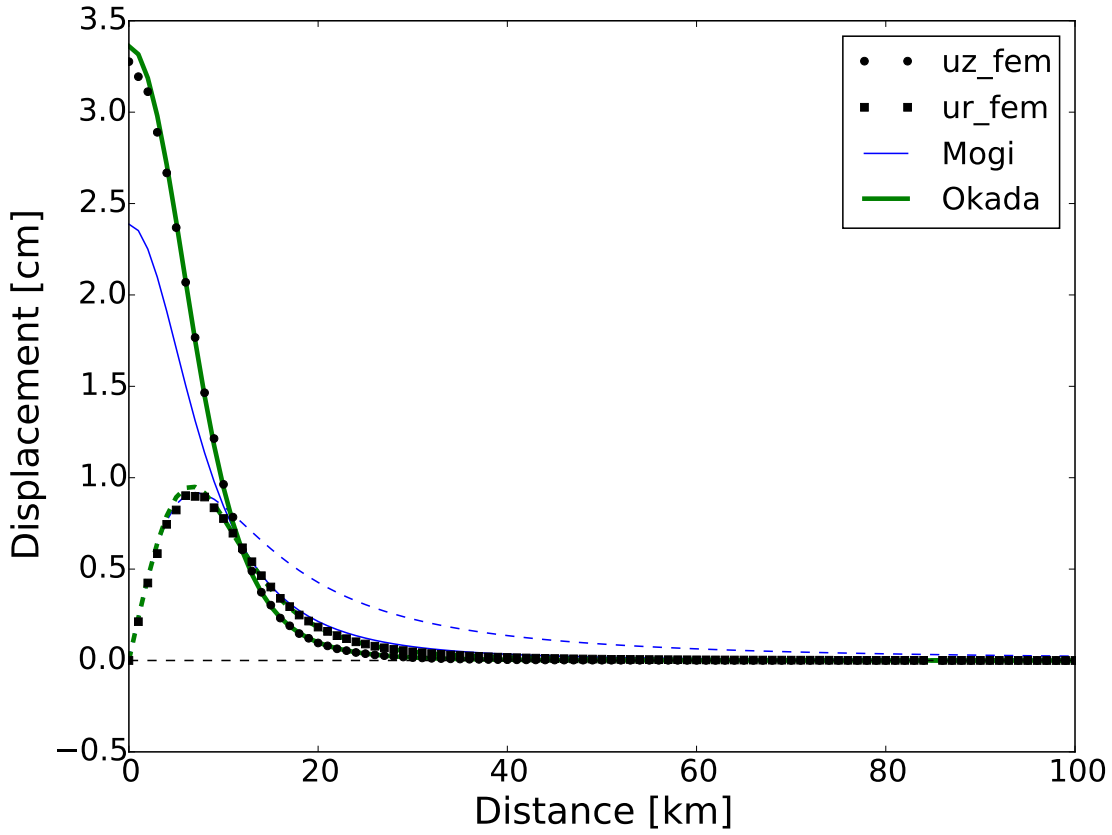

Figure 4.14: FEM finite sill opening benchmark. Solid lines correspond to vertical displacement and dashed lines correspond to radial displacement. FEM solution for a 10x10 km sill with 10 cm of opening at 10 km depth shown in black with squares for radial displacement and circles for vertical displacement at surface node points. Green lines show the analytical solution for a 10x10 km dislocation in a Poissonian half-space (*Okada*, 1985). Blue lines correspond to the solution for a spherical point source with equivalent volume change (0.01km^3) for comparison (*Mogi*, 1958).

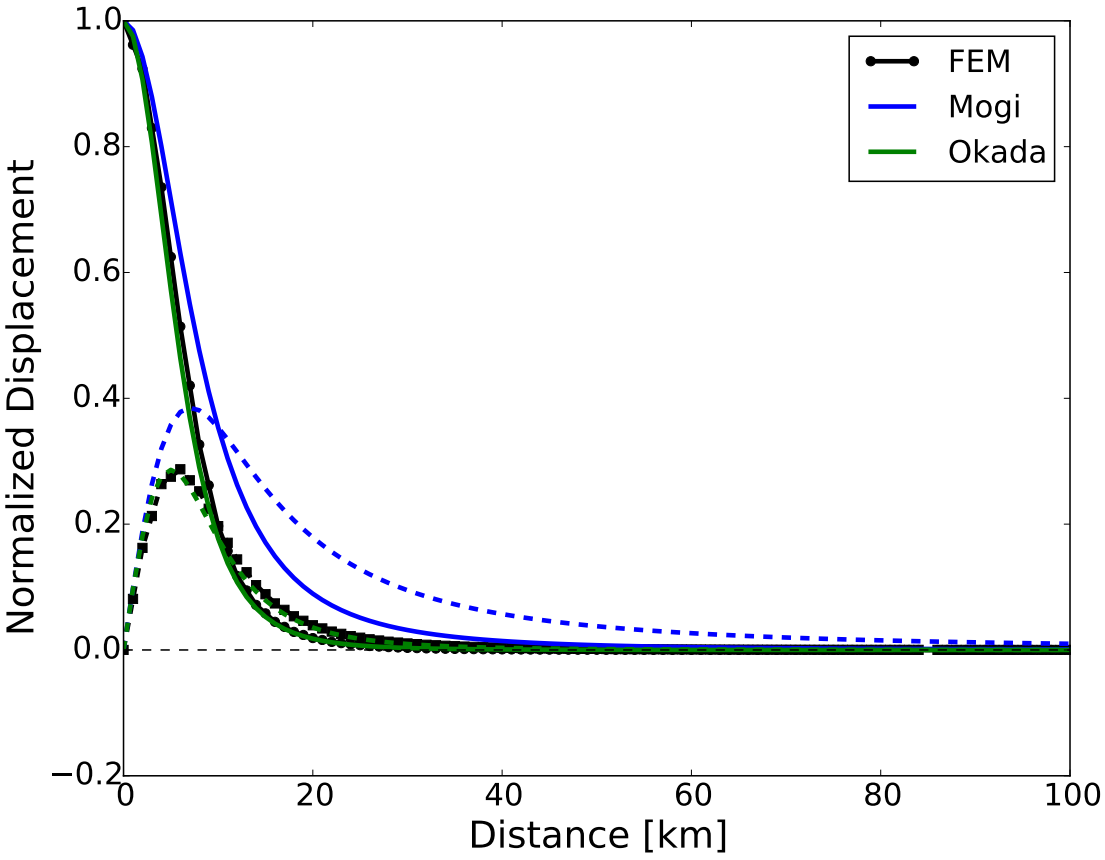

Figure 4.15: FEM point sill benchmark. Solid lines correspond to vertical displacement and dashed lines correspond to radial displacement. FEM solution for a 2x2 km sill at 10km depth shown in black with squares for radial displacement and circles as vertical displacement at surface node points. Green lines correspond to the analytical solution for a 2x2 km dislocation in a Poissonian half-space (*Okada*, 1985). Blue lines correspond the solution for a spherical point source at for comparison (*Mogi*, 1958). Displacements are normalized to maximum vertical displacement.

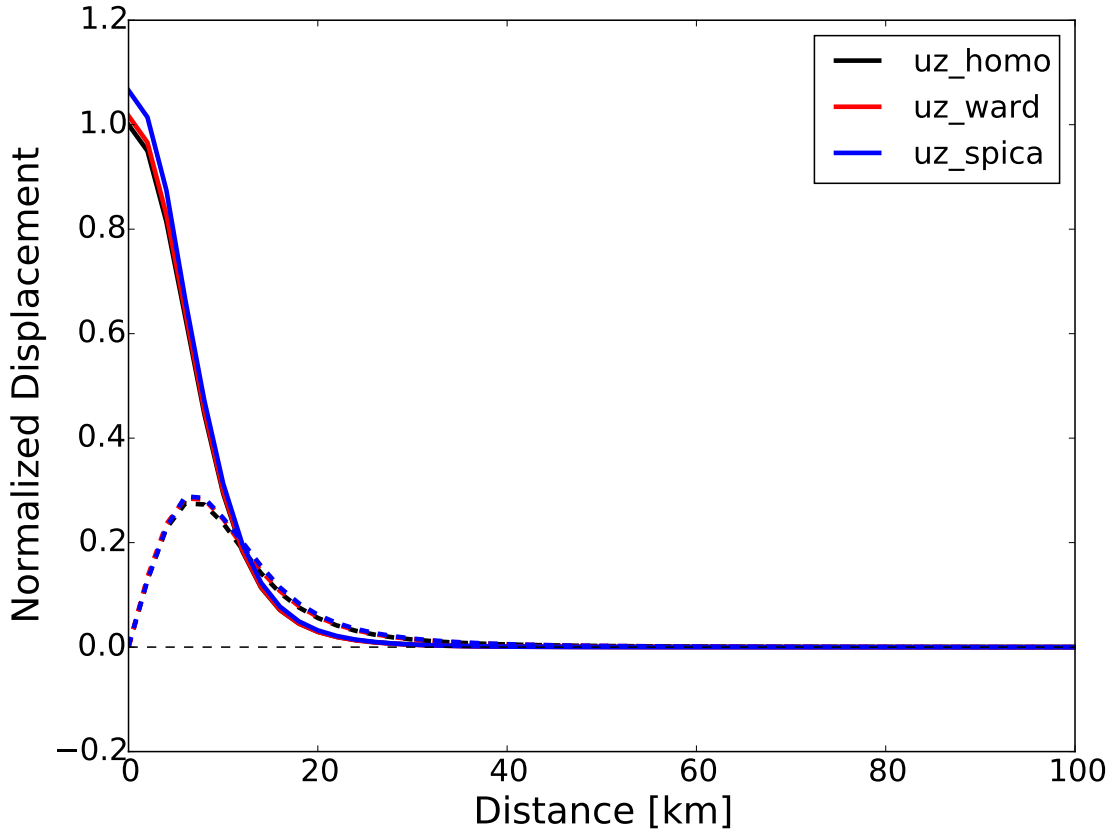

Figure 4.16: Comparison of surface displacements for heterogeneous crust (see 4.4). Solid lines represent vertical displacements, dashed lines are radial displacements. Black corresponds to homogeneous domain, red corresponds to 1D heterogeneity based on *Ward et al.* (2013), Blue corresponds to 3D heterogeneous domain based on *Spica et al.*. All displacements are normalized to maximum vertical displacement for homogeneous case of 10cm opening of a 10x10km sill at 10km depth.

Satellite	Track	Orbit	Beam	Incidence	# Dates	# IFGs	Start	End	$B_\perp$
Envisat	WS89	Asc.	2	25.0	23	1	2003/09/22	2009/11/09	350
Envisat	WS361	Asc.	-	29.5	29	?	2005/10/15	2009/11/28	350
ALOS	102	Asc.	-	34.3	16	26	2007/02/09	2011/02/20	1000
TSX	134	Asc.	8	29.5	6	8	2008/04/26	2014/08/23	320
TSX	20	Dsc.	3	18.4	6	8	2011/12/22	2014/08/16	430
TSX	111	Dsc.	11	39.1	5	8	2011/12/28	2014/09/02	150
CSK	-	Asc.	-	45.5	5	5	2011/03/25	2012/04/12	150
CSK	″	″	-	44.9	32	54	2013/08/01	2014/09/02	150
CSK	-	Dsc.	-	36.0	10	17	2011/04/29	2012/02/19	150
CSK	″	″	-	″	19	27	2013/07/23	2014/09/02	150

Table 4.1: Recent InSAR datasets covering Lazufre. For each track, we list the orbit direction (Asc = Ascending, Dsc = Descending), the number of SAR images (# Dates), the number interferograms (# IFG's), and the oldest (Start) and most recent (End) dates of acquisition. Where applicable, we list the maximum perpendicular baseline used when generating the set of interferograms, '-' indicates that no specific threshold was used. Note that the CSK archive is not organized by track and beam.

Station	Latitude	Longitude	Altitude [m]	Start	End	V_{EW}	V_{NS}	V_Z
LCEN	-25.326	-68.603	4270.943	2010/11/07	2014/03/20	16.0	17.9	6.9
LLST	-25.165	-68.520	5272.150	2010/11/07	2014/03/23	16.2	16.8	6.1
SOCM	-24.455	-68.295	3969.435	2011/11/13	2014/03/14	17.9	16.6	0.7

Table 4.2: Continuous GPS stations at Lazufre. Rates [mm/yr] are calculated from least squares regression of daily IGS08 positions without removing a seasonal signal. Data has been processed by the University of Nevada Geodetic Laboratory (*Blewitt et al.*, 2013).

Station	Latitude	Longitude	Altitude [m]	Start	End	V_{EW}	V_{NS}	V_Z
CNTR	-25.268	-68.481	4646	2011/11/14	2014/03/20	-	-	16.0
FOLD	-25.178	-68.626	4275	2011/11/14	2014/03/20	-	-	11.5
RDHL	-25.257	-68.379	4343	2011/11/14	2014/03/20	-	-	19.8
TQLK	-25.221	-68.429	4375	2011/11/14	2014/03/20	-	-	12.4
VIEW	-25.013	-68.642	3719	2011/11/14	2014/03/20	-	-	16.8
CHNK	-25.025	-68.579	3887	2011/11/14	2014/03/20	-	-	-
SDHL	-25.324	-68.683	3916	2011/11/14	2014/03/20	-	-	-
ICES	-25.250	-68.609	4483	2011/11/14	2014/03/20	-	-	-
WIRG	-25.056	-68.573	4132	2011/11/14	2014/03/20	-	-	-

Table 4.3: Campaign GPS Stations at Lazufre. Rates [mm/yr] are calculated after removing the seasonal signal predicted by a GRACE-based model at continuous station LCEN. Recording equipment was set up at each benchmark for at least 3 days from designated start and end dates. Note that not all data is reported because processing has not yet been completed.

	Vs [km/s]	Vp [km/s]	Rho [g/cm^3]	nu	E [GPa]	G [GPa]
Ward et al. (2013)						
min	3.0	5.1	2.6	0.23	58	24
mean	3.3	5.7	2.7	0.23	75	47
max	4.0	6.9	2.9	0.25	116	77
Spica et al.						
min	1.3	2.7	2.2	0.23	9.5	3.5
mean	2.9	5.0	2.6	0.24	57	23
max	3.6	6.1	2.8	0.37	89	36
Del Negro et al. (2009)						
	3.3	5.7	2.7	0.25	75	30

Table 4.4: Elastic properties from tomography at Lazufre. Ward study goes to -54km below the surface in an area 50x50km. Spica has resolution to -7.3 km below the surface in an area approximately 10x10km (see Figure 4.10). Typical half-space parameters for volcano modeling taken from Del Negro 2009.

Geometry	Depth [km]	Volume [km^3/yr]	A [km]	B [km]	Strike [°E of N]	Dip [°E]	Reference
horizontal square sill	10	?	7	7	0	0	*Pritchard and Simons* (2004)
horizontal ellipsoid	10	0.01	10	1	25	9	*Froger et al.* (2007)
expanding horizontal sill	13	?	20	7	28	0	*Ruch et al.* (2009)
expanding horizontal sill	10	?	24	13	30	0	*Anderssohn et al.* (2009)
dipping rectangular sill	8	0.03	30	20	10	10	*Pearse and Lundgren* (2013)
dipping ellipsoid	11	0.03	30	12	24	3	*Remy et al.* (2014)

Table 4.5: Review of Lazufre geodetic models. Note that all values are rounded to nearest kilometer, depths are relative to the surface (≈4.8km above sea level) and 'A' axis is along-strike. All models assume Poissonian crust. Tendency towards broader sill size and larger opening rates at relatively fixed strike, dip, and depth reflects increasing observed amplitude and static spatial pattern of surface deformation.

CHAPTER 5

SUMMARY OF KEY RESULTS

Here I re-state key conclusions from the preceding chapters as simple bulletized lists:

5.1 Chapter 1

- Observations of volcano deformation have increased greatly with advent of GPS and InSAR. There were 44 known volcanoes in 1997, and now 211 known in 2014
- The Central Andes Volcanic Zone is unique in that it contains 70 Holocene Volcanoes (40% of those in SA), but lags in terms of large eruptions (12.5% of 593 confirmed eruptions of with a VEI greater than 2).
- Geodetic observations since 1992 have so far revealed that 40% of volcanic deformation events in the Andes occur in the CVZ, and half of the 20 known uplifting volcanoes in the Andes occur in the CVZ

5.2 Chapter 2

- An InSAR-based survey enables consistent comparison of spatial and temporal deformation trends in the CVZ from 1992 through 2011. Uplift footprints range in size from 2 km diameter to 150 km diameter, and are observed as short-lived pulses, monotonic rates, and periods of acceleration.

- We described 3 previously undocumented volcanic deformation centers: Putana Volcano, Cerro Overo, and Sillajhuay Volcano. The later two are not clearly associate with a Holocene edifice, and therefore demonstrate the importance of geodetic observations in classifying 'active' volcanoes.
- Combining four independent viewing geometries at Uturuncu Volcano revealed an unprecedented continuous 'moat' of subsidence out to 150 km from the center of deformation. This observation prompted the detailed modeling study in Chapter 3.

5.3 Chapter 3

- Vertically-aligned 'dipole' magma reservoirs represent a physically plausible model for deformation at Uturuncu Volcano
- The ratio of vertical to radial displacements for single inflation source is increased by adding a dipole 'source' reservoir (deflation), but decreased to a greater degree by crustal heterogeneity
- Volume discrepancies of 1-10x between source and sink reservoirs are expected given known ranges of lower crustal material properties

5.4 Chapter 4

- InSAR Measurements beyond 2010 are presented for the first time. Preliminary analysis of Cosmo-SkyMed and TerraSAR-X data from 2010 through the present (09/2014) indicates that the spatial and temporal patterns of uplift remain consistent with observations described in Chapter 2

- Proposed subsurface heterogeneity from seismic tomography increases the surface displacements for homogeneous crust by less than 7% within a 10km radius of the center of uplift

5.5 Future Research Directions

While this thesis describes several advances in our understanding of magmatic ascent in the Central Andes Volcanic Zone, there are many remaining questions that should be examined in future work. Therefore, I end the document by identifying key questions and recommendations for continued study.

5.5.1 Recommendation for continued observation

The installation of continuous GPS stations at Uturuncu and Lazufre have been critical to overcome the temporal aliasing of InSAR observations (and in filling in the geodetic timeseries after Envisat and ALOS satellites failed). Biannnual servicing during the last five years has shown that three stations per deformation site should be considered minimum in light of common equipment malfunction and theft. The station near the summit of Lastarria volcano will require maintenance since the antenna mast and electric connections are corroding rapidly due to nearby gas emissions. The continuity of GPS observations will be critical in determining the true temporal variation of deformation at Uturuncu and Lazufre.

Currently functioning InSAR satellites (TSX, CSK, Sentinel-1, ALOS-2) have more frequent observation intervals (biweekly) that are coincident in time with

GPS observations. InSAR acquisitions over Uturuncu and Lazufre should be as frequent as possible and sustained for a decade or more in order to identify low amplitude signals as was done for the 1992 to 2011 time period. Furthermore, the ability to process ScanSAR data with new interferometry software (e.g. ISCE, SNAP) will be a major advantage for conducting arc-scale surveys and characterizing long-wavelength signals such as the moat of subsidence at Uturuncu. Finally, it is hopefully that near real time monitoring of volcanic deformation can be communicated to volcano observatories in order to forecast eruptive activity and predict volumes of effusion.

5.5.2 How can finite element models be improved?

While myriad finite element software packages exist for geodynamic modeling, I have chosen to utilize PyLith software for this work. COMSOL and ABAQUS are alternative commercial packages that are commonly used in studies of earthquake and volcano deformation; however, they are extremely costly and focused on engineering rather than geophysical problems. While already very capable, the roadmap for PyLith development is very promising for the near future (http://wiki.geodynamics.org/software:pylith:plans:2014). In particular, the incorporation of 'multiphysics', or the ability to couple deformation with heat transport will be advantageous to volcanic studies. Finally, the usefulness of finite element models is largely dictated by the availability of seismic tomography, which provides a direct measure of subsurface material properties. Detailed 3D geophysical images are just now becoming available after the PLUTONS research project. We have already seen in Chapter 3 how additional data and refined tomographic techniques have reshaped our understanding of upper

crustal features. Undoubtedly, different tomographic models of the subsurface will be proposed in coming years, and finite element modeling will provides a means to check these models against surface deformation data.

5.5.3 Has Uturuncu stopped deforming?

GPS measurements over the last 4 years indicate deformation at Uturuncu may have a nonlinear rate of deformation, suggesting either changes in the deformation source, or mis-interpretation of a 'constant' rate in previous InSAR studies due to temporal aliasing. Remaining work with GPS data includes isolating the volcanic uplift signal from interseismic and seasonal loading signals.

It will be interesting to see if another broad uplift anomaly is detected elsewhere in the CVZ over the next two decades. If so, perhaps the association of deformation with Uturuncu is merely coincidental and perturbations of the partially molten APMB lead to distributed uplift events throughout the region on a timescale of centuries to millennia.

5.5.4 Which magma ascent mechanism is most likely at Uturuncu?

The ascent mechanism of magma underneath Uturuncu is still debated. In order to decipher between diapiric ascent versus porous flow or conduit flow between discrete chambers will require further monitoring and modeling. Smoothly varying temporal trends and maintained spatial extents would lend support to

the hypothesis of steady state en masse rise, whereas abrupt changes in spatial and temporal patterns are more easily explained by non-steady state transient subsurface movement of magma.

5.5.5 Why is peripheral subsidence rarely observed?

It is odd that peripheral subsidence is not readily observed at other uplifting areas of the CVZ, since both the diapir model and transport between vertically aligned chambers predict such a signal. Possible explanations are that peripheral subsidence is below the level of noise in most areas or that sustained steady-state transport is required to accumulate an observable signal at other areas. More needs to be known about deep properties of the crust (composition, rheological constitutive law) and magmas (volatile content, ascent rates) in order to improve our understanding of the conditions under which peripheral subsidence will produce a detectable surface signal.

BIBLIOGRAPHY

Aagaard, B. T., M. G. Knepley, and C. A. Williams (2013), A domain decomposition approach to implementing fault slip in finite-element models of quasi-static and dynamic crustal deformation, *Journal of Geophysical Research: Solid Earth (1978–2012)*, *118*(6), 3059–3079.

Aguilera, F., F. Tassi, T. Darrah, S. Moune, and O. Vaselli (2011), Geochemical model of a magmatic–hydrothermal system at the Lastarria volcano, northern Chile, *Bulletin of Volcanology*, *74*(1), 119–134.

Allmendinger, R. W., T. E. Jordan, S. M. Kay, and B. L. Isacks (1997), The evolution of the altiplano-puna plateau of the central andes, *Anuual Review of Earth and Planetary Science*, *25*, 139:174.

Amelung, F., H. Zebker, P. Segall, and S. Jónsson (2000), Widespread uplift and trapdoor faulting on 'Galpagos' volcanoes observed with radar interferometry, *Nature*, *407*(6807), 993–996.

Anderssohn, J., M. Motagh, T. R. Walter, M. Rosenau, H. Kaufmann, and O. Oncken (2009), Surface deformation time series and source modeling for a volcanic complex system based on satellite wide swath and image mode interferometry: The Lazufre system, central Andes, *Remote Sensing of Environment*, *113*(10), 2062–2075.

Annen, C., J. D. Blundy, and R. S. J. Sparks (2006), The genesis of intermediate and silicic magmas in deep crustal hot zones, *Journal of Petrology*, *47*(3), 505–539.

Armienti, P., C. Perinelli, and K. Putirka (2012), A New Model to Estimate Deep-

level Magma Ascent Rates, with Applications to Mt. Etna (Sicily, Italy), *Journal of Petrology*, *0*(0), 1–19.

Arndt, J., T. Bartel, E. Scheuber, and F. R. Schilling (1997), Thermal and rheological properties of granodioritic rocks from the Central Andes, North Chile, *Tectonphysics*, *271*(1-2), 75–88.

Babeyko, A. Y., S. V. Sobolev, R. B. Trumbull, O. Oncken, and L. L. Lavier (2002), Numerical models of crustal scale convection and partial melting beneath the Altiplano-Puna plateau, *Earth˜Planet.˜Sci.˜Lett.*, *199*, 373–388.

Bachmann, O., C. Miller, and S. L. de Silva (2007), The volcanic–plutonic connection as a stage for understanding crustal magmatism, *Journal of Volcanology and Geothermal Research*, *167*(1-4), 1–23.

Baker, D. R., and M. Alletti (2012), Fluid saturation and volatile partitioning between melts and hydrous fluids in crustal magmatic systems: The contribution of experimental measurements and solubility . . . , *Earth-Science Reviews*.

Baker, M. C. W., and P. W. Francis (1978), Upper Cenozoic volcanism in the Central Andes — Ages and volumes, *Earth˜Planet.˜Sci.˜Lett.*, *41*(2), 175–187.

Barazangi, M., and B. Isacks (1976), Spatial distribution of earthquakes and subduction of the Nazca plate beneath South America, *Geology*, *4*(11), 686–692.

Bechor, N., and H. Zebker (2006), Measuring two-dimensional movements using a single InSAR pair, *Geophys Res . . . .*

Berardino, P., G. Fornaro, R. Lanari, S. Member, and E. Sansosti (2002), A New Algorithm for Surface Deformation Monitoring Based on Small Baseline Differential SAR Interferograms, *Geoscience and Remote Sensing, IEEE Transactions on*, *40*(11), 2375–2383.

Bianchi, M., B. Heit, A. Jakovlev, X. Yuan, and S. M. Kay (2013), Teleseismic tomography of the southern Puna plateau in Argentina and adjacent regions, *Tectonphysics*, *586*, 65–83.

Biggs, J., T. Wright, Z. Lu, and B. Parsons (2007), Multi-interferogram method for measuring interseismic deformation: Denali Fault, Alaska, *Geophys J Int*, *170*(3), 1165–1179.

Biggs, J., S. K. Ebmeier, W. P. Aspinall, Z. Lu, M. E. Pritchard, R. S. J. Sparks, and T. A. Mather (2014), Global link between deformation and volcanic eruption quantified by satellite imagery, *Nature Communications*, *5*.

Bills, B. G., S. L. de Silva, D. R. Currey, R. S. Emenger, K. D. Lillquist, A. Donnellan, and B. Worden (1994), Hydro-isostatic deflection and tectonic tilting in the central Andes: Initial results of a GPS survey of Lake Minchin shorelines, *Geophys Res . . .*, *21*(4), 293–296.

Blewitt, G., C. Kreemer, W. C. Hammond, and J. M. Goldfarb (2013), Terrestrial reference frame NA12 for crustal deformation studies in North America, *Journal of Geodynamics*, *72*, 11–24.

Blundy, J. D., K. V. Cashman, A. C. Rust, and F. Witham (2010), A case for CO2-rich arc magmas, *Earth˜Planet.˜Sci.˜Lett.*, *290*(3-4), 289–301.

Bonafede, M., M. Dragoni, and F. Quareni (1986), Displacement and stress fields produced by a centre of dilation and by a pressure source in a viscoelastic half-space: application to the study of ground deformation and seismic activity at Campi Flegrei, Italy, *Geophys J Int*, *87*, 455–485.

Brocher, T. M. (2005), Empirical Relations between Elastic Wavespeeds and Den-

sity in the Earth's Crust, *Bulletin of the Seismological Society of . . .*, *95*(6), 2081–2092.

Brooks, B. A. (2012), Seeing Is Believing, *Science (Washington, D.C.); (United States)*, *338*(6104), 207–208.

Brown, M. (2007), Crustal melting and melt extraction, ascent and emplacement in orogens: mechanisms and consequences, *Journal of the Geological Society*, *164*, 709–730.

Brunori, C. A., C. Bignami, S. Stramondo, and E. Bustos (2013), 20 years of active deformation on volcano caldera: Joint analysis of InSAR and AInSAR techniques, *International Journal of Applied Earth Observations and Geoinformation*, *23*, 279–287.

Budach, I., H. Brasse, and D. Diaz (2013), Crustal-scale electrical conductivity anomaly beneath inflating Lazufre volcanic complex, Central Andes, *Journal of South American Earth Sciences*, pp. 1–25.

Buergmann, R., P. A. Rosen, and E. J. Fielding (2000), Synthetic Aperture Radar Interferometry to Measure Earth's Surface Topography and Its Deformation, *Anuual Review of Earth and Planetary Science*, *28*, 169–209.

Burnham, C. W. (1975), Water and magmas; a mixing model, *Geochimica et Cosmochimica Acta*, *39*(8), 1077–1084.

Cahill, T., and B. Isacks (1992), Seismicity and shape of the subducted Nazca Plate, *Journal of Geophysical Research: Solid Earth (1978–2012)*, *97*(B12), 17–503–17–529.

Carter, N. L., and M. C. Tsenn (1987), Flow properties of continental lithosphere, *Tectonphysics*.

Cashman, K., and R. S. J. Sparks (2013), How volcanoes work: A 25 year perspective, *Geological Society Of America Bulletin*, *125*(5-6), 664–690.

Casu, F., M. Manzo, and R. Lanari (2006), A quantitative assessment of the SBAS algorithm performance for surface deformation retrieval from DInSAR data, *Remote Sensing of Environment*, *102*(3-4), 195–210.

Casu, F., M. Manzo, A. Pepe, R. Lanari, and S. Member (2008), SBAS-DInSAR Analysis of Very Extended Areas : First Results on a 60 000-km 2 Test Site, *Geoscience and Remote Sensing Letters, IEEE*, *5*(3), 438–442.

Chen, C. W., and H. Zebker (2001), Two-dimensional phase unwrapping with use of statistical models for cost functions in nonlinear optimization, *Journal of the Optical Society of America*, *18*(2), 338–351.

Cheng, C. H., and D. H. Johnston (1981), Dynamic and static moduli, *Geophys Res . . .*, *8*(1), 39–42.

Chmielowski, J., G. Zandt, and C. Haberland (1999), The Central Andean Altiplano-Puna Magma Body, *Geophys Res . . .*, *26*(6), 783–786.

Clemens, J. D., and C. Mawer (1992), Granitic magma transport by fracture propagation, *Tectonphysics*, *204*(3-4), 339–360.

Crosweller, H. S., et al. (2012), Global database on large magnitude explosive volcanic eruptions (LaMEVE), *Journal of Applied Volcanology*, *1*(1), 1–13.

Currenti, G., C. Del Negro, and G. Ganci (2007), Modelling of ground deformation and gravity fields using finite element method: an application to Etna volcano, *Geophys J Int*, *169*(2), 775–786.

Davis, J. L. (2004), Climate-driven deformation of the solid Earth from GRACE and GPS, *Geophys Res . . .*, *31*(24), 2–5.

de Silva, S. L. (1989), Altiplano-Puna volcanic complex of the central Andes, *Geology*, *17*, 1102–1106.

de Silva, S. L., and P. W. Francis (1991), *Volcanos of the Central Andes*, Springer-Verlag, New York.

de Silva, S. L., and W. D. Gosnold (2007), Episodic construction of batholiths: Insights from the spatiotemporal development of an ignimbrite flare-up, *Journal of Volcanology and Geothermal Research*, *167*(1-4), 320–335.

Del Negro, C., G. Currenti, and D. Scandura (2009), Temperature-dependent viscoelastic modeling of ground deformation: Application to Etna volcano during the 1993–1997 inflation period, *Physics of the Earth and Planetary Interiors*, *172*(3-4), 299–309.

Delacourt, C., P. Briole, and J. Achache (1998), Tropospheric corrections of SAR interferograms with strong topography. Application to Etna, *Geophys Res . . .*, *25*(15), 2849–2852.

Delaney, P. T., and D. F. McTigue (1994), Volume of magma accumulation or withdrawal estimated from surface uplift or subsidence , with application to the 1960 collapse of Kilauea Volcano, *Bulletin of Volcanology*, *56*, 417–424.

Deligne, N. I., and S. G. Coles (2010), Recurrence rates of large explosive volcanic eruptions, *Journal of Geophysical Research: Solid Earth (1978–2012)*.

Deruelle, B. (1982), Petrology of the plio-quaternary volcanism of the south-central and meridional andes, *Journal of Volcanology and Geothermal Research*, *14*, 77–124.

Dieterich, J. H., and R. W. Decker (1975), Finite Element Modeling of Surface Deformation Associated With Volcanism, *Journal of Geophysical Research: Solid Earth (1978–2012)*, *80*(29), 4094–4102.

Doornbos, E., and R. Scharroo (2005), Improved ERS and Envisat precise orbit determination, in *Proceedings of the 2004 Envisat and ERS Symposium*, edited by H. Lacoste and L. Ouwehand, pp. 1–8, Salzburg, Austria.

Dosseto, A., S. P. Turner, and J. A. Van-Orman (2011), *Timescales of Magmatic Processes*, From Core to Atmosphere, John Wiley & Sons.

Dvorak, J. J., and D. Dzurisin (1997), Volcano geodesy: The search for magma reservoirs and the formation of eruptive vents, *Reviews of Geophysics*, *35*(3), 343–384.

Dzurisin, D. (2000), Volcano geodesy: challenges and opportunities for the 21st century, *Philosophical Transactions of the Royal Society A: Mathematical, Physical and Engineering Sciences*, *358*(1770), 1547–1566.

Dzurisin, D. (2003), A comprehensive approach to monitoring volcano deformation as a window on the eruption cycle, *Reviews of Geophysics*, *41*(1), 1–29.

Dzurisin, D. (2007), *Volcano deformation*, geodetic monitoring techniques, Springer Verlag.

Ebmeier, S. K., J. Biggs, T. A. Mather, and F. Amelung (2013), On the lack of InSAR observations of magmatic deformation at Central American volcanoes, *Journal of Geophysical Research: Solid Earth (1978–2012)*, *118*(5), 2571–2585.

Farr, T. G., et al. (2007), The Shuttle Radar Topography Mission, (2005), 1–33.

FernandezTuriel, J. L., J. Saavedra, J. F. Perez-Torrado, A. Rodriguez-Gonzalez, J. C. Carracedo, M. Osterrieth, J. I. Carrizo, and G. Esteban (2013), The largest holocene eruption of the Central Andes found, in *AGU*.

Ferretti, A., C. Prati, and F. Rocca (2001), Permanent scatterers in SAR interferometry, *Geoscience and Remote Sensing, IEEE Transactions on*, *39*(1), 8–20.

Ferretti, A., G. Savio, R. Barzaghi, A. Borghi, S. Musazzi, F. Novali, C. Prati, and F. Rocca (2007), Submillimeter Accuracy of InSAR Time Series: Experimental Validation, *Geoscience and Remote Sensing, IEEE Transactions on*, *45*(5), 1142–1153.

Fialko, Y. A. (2006), Interseismic strain accumulation and the earthquake potential on the southern San Andreas fault system, *Nature*, *441*(7096), 968–971.

Fialko, Y. A., and J. Pearse (2012), Sombrero Uplift Above the Altiplano-Puna Magma Body: Evidence of a Ballooning Mid-Crustal Diapir, *Science (Washington, D.C.); (United States)*, *338*(6104), 250–252.

Fialko, Y. A., Y. Khazan, and M. Simons (2001a), Deformation due to a pressurized horizontal circular crack in an elastic half-space, with applications to volcano geodesy, *Geophys J Int*, *146*, 181–190.

Fialko, Y. A., M. Simons, and D. C. Agnew (2001b), The complete (3D) surface displacement field in the epicentral area of the 1999 Mw 7.1 Hector Mine earthquake, California, from space geodetic observations, *Geophys Res ...*, *28*(16), 3063–3066.

Finnegan, N. J., M. E. Pritchard, R. B. Lohman, and P. R. Lundgren (2008), Constraints on surface deformation in the Seattle, WA, urban corridor from satellite radar interferometry time-series analysis, *Geophys J Int*, *174*(1), 29–41.

Foroozan, R., D. Elsworth, B. Voight, and G. Mattioli (2010), Dual reservoir structure at Soufrière Hills Volcano inferred from continuous GPS observations and heterogeneous elastic modeling, *Geophys Res . . .*, *37*.

Fournier, T., M. E. Pritchard, and N. Finnegan (2011), Accounting for Atmospheric Delays in InSAR Data in a Search for Long-Wavelength Deformation in South America, *Geoscience and Remote Sensing, IEEE Transactions on*, *49*(10), 3856–3867.

Fournier, T. J., M. E. Pritchard, and S. N. Riddick (2010), Duration, magnitude, and frequency of subaerial volcano deformation events: New results from Latin America using InSAR and a global synthesis, *Geochemistry Geophysics Geosystems*, *11*(1), 1–29.

Freed, A. M., and R. Buergmann (2004), Evidence of power-law flow in the Mojave desert mantle., *Nature*, *430*(6999), 548–551.

Freed, A. M., R. Buergmann, and T. Herring (2007), Far-reaching transient motions after Mojave earthquakes require broad mantle flow beneath a strong crust, *Geophys Res . . .*, *34*(19), 1–5.

Froger, J.-L., D. Remy, S. Bonvalot, and D. Legrand (2007), Two scales of inflation at Lastarria-Cordon del Azufre volcanic complex, central Andes, revealed from ASAR-ENVISAT interferometric data, *Earth˜Planet.˜Sci.˜Lett.*, *255*(1-2), 148–163.

Fu, Y., and J. T. Freymueller (2012), Seasonal and long-term vertical deformation in the Nepal Himalaya constrained by GPS and GRACE measurements, *Journal of Geophysical Research: Solid Earth (1978–2012)*.

Fu, Y., D. F. Argus, and J. T. Freymueller (2013), ... motion in elastic response to seasonal loading of rain water in the Amazon Basin and monsoon water in Southeast Asia observed by GPS and inferred from GRACE, *Geophys Res ...*.

Geyer, A., and J. Gottsmann (2010), The influence of mechanical stiffness on caldera deformation and implications for the 1971-1984 Rabaul uplift (Papua New Guinea), *Tectonphysics*, *483*, 399–412.

Geyer, A., and J. Martí (2008), The new worldwide collapse caldera database (CCDB): A tool for studying and understanding caldera processes, *Journal of Volcanology and Geothermal Research*, *175*(3), 334–354.

Giordano, D., J. K. Russell, and D. B. Dingwell (2008), Viscosity of magmatic liquids: A model, *Earth˜Planet.˜Sci.˜Lett.*, *271*(1-4), 123–134.

Glazner, A. F., J. M. Bartley, D. Coleman, W. Gray, and R. Taylor (2004), Are plutons assembled over millions of years by amalgamation from small magma chambers?, *GSA Today*, *14*(4/5), 4–12.

Goldstein, R. M. (1995), Atmospheric limitations to repeat-track radar interferometry, *Geophys Res ...*, *22*(18), 2517–2520.

Gonzalez-Ferran, O. (1995), *Volcanes de Chile*, 1 ed., Instituto Geographico Militar, Santiago, Chile.

Got, J. L., A. Peltier, and T. Staudacher (2013), Edifice strength and magma transfer modulation at Piton de la Fournaise volcano, *Journal of ...*.

Gray, A. L., K. E. Mattar, and G. Sofko (2000), Influence of ionospheric electron density fluctuations on satellite radar interferometry, *Geophys Res ...*, *27*(10), 1451–1454.

Guccione, P. (2006), Interferometry with ENVISAT wide swath ScanSAR data, *Geoscience and Remote Sensing Letters, IEEE*, *3*(3), 377–381.

Gudmundsson, A. (2012), Magma chambers: formation, local stresses, excess pressures, and compartments, *Journal of Volcanology and Geothermal Research*.

Hansen, F. D., and N. L. Carter (1982), Creep of selected crustal rocks at 1000 MPa, *Eos*, *63*(18), 437.

Hansen, F. D., and N. L. Carter (1983), Semibrittle Creep Of Dry And Wet Westerly Granite At 1000 MPa, *The 24th U.S. Symposium on Rock Mechanics (USRMS)*.

Hautmann, S., J. Gottsmann, R. S. J. Sparks, G. Mattioli, I. S. Sacks, and M. H. Strutt (2010), Effect of mechanical heterogeneity in arc crust on volcano deformation with application to Soufrière Hills Volcano, Montserrat, West Indies, *Journal of Geophysical Research: Solid Earth (1978–2012)*, *115*(B9), 1–18.

Henderson, S. T., and M. E. Pritchard (2013), Decadal volcanic deformation in the Central Andes Volcanic Zone revealed by InSAR time series, *Geochemistry Geophysics Geosystems*, *14*(5), 1358–1374.

Hetland, E. A., P. Muse, M. Simons, Y.-n. N. N. Lin, P. S. Agram, and C. J. DiCaprio (2011), Multiscale InSAR Time Series (MInTS) analysis of surface deformation, *Journal of Geophysical Research: Solid Earth (1978–2012)*, *117*(February), 1–17.

Hickey, J., J. Gottsmann, and R. del Potro (2013), The large-scale surface uplift in the Altiplano-Puna region of Bolivia: A parametric study of source characteristics and crustal rheology using finite element analysis, *Geochemistry Geophysics Geosystems*, *14*(3), 540–555.

Hildreth, W., and S. Moorbath (1988), Crustal contributions to arc magmatism in the Andes of Central Chile, *Contributions to Mineralogy and Petrology*, *98*, 455–489.

Holtkamp, S. G., M. E. Pritchard, and R. B. Lohman (2011), Earthquake swarms in South America, *Geophys J Int*, *187*(1), 128–146.

Hooper, A., D. Bekaert, K. Spaans, and M. Arıkan (2011), Recent advances in SAR interferometry time series analysis for measuring crustal deformation, *Tectonphysics*, *514-517*, 1–13.

Houghton, B. F., D. Swanson, J. Rausch, and R. J. Carey (2013), Pushing the Volcanic Explosivity Index to its limit and beyond: Constraints from exceptionally weak explosive eruptions at Kīlauea in 2008, ...

Hunter, J. D. (2007), Matplotlib: a 2D graphics environment, *Computing in Science & Engineering*.

Huppert, H. E., and A. W. Woods (2002), The role of volatiles in magma chamber dynamics, *Nature*, *420*(6915), 493–495.

Huppert, H. E., and A. W. Woods (2006), Gravity-driven flows in porous layers, *Journal of Fluid Mechanics*, *292*(-1), 55–69.

Isacks, B. L. (1988), Uplift of the Central Andean Plateau and Bending of the Bolivian Orocline, *Journal of Geophysical Research: Solid Earth (1978–2012)*, *93*(B4), 3211–3231.

James, D. E. (1971), Andean Crustal and Upper Mantle Structure, *Journal of Geophysical Research: Solid Earth (1978–2012)*, *76*(14), 3246–3271.

Jay, J. A., M. E. Pritchard, M. E. West, D. Christensen, M. Haney, E. Minaya, M. Sunagua, S. R. McNutt, and M. Zabala (2012), Shallow seismicity, triggered seismicity, and ambient noise tomography at the long-dormant Uturuncu Volcano, Bolivia, *Bulletin of Volcanology*, *74*(4), 817–837.

Jay, J. A., F. Costa, M. E. Pritchard, L. Lara, B. S. Singer, and J. Herrin (2014), Locating magma reservoirs using InSAR and petrology before and during the 2011–2012 Cordón Caulle silicic eruption, *Earth˜Planet.˜Sci.˜Lett.*, *395*, 254–266.

Johnson, D., F. Sigmundsson, and P. T. Delaney (2000), Comment on "Volume of magma accumulation or withdrawal estimated from surface uplift or subsidence, with application to the 1960 collapse of Kilauea Volcano" by P.T. Delaney and D.F. McTigue, *Bulletin of Volcanology*, *61*, 491–493.

Kay, S. M., B. L. Coira, P. J. Caffe, and C.-H. Chen (2010a), Regional chemical diversity, crustal and mantle sources and evolution of central Andean Puna plateau ignimbrites, *Journal of Volcanology and Geothermal Research*, *198*(1-2), 81–111.

Kay, S. M., B. Coira, G. Worner, R. W. Kay, and B. S. Singer (2010b), Geochemical, isotopic and single crystal 40Ar/39Ar age constraints on the evolution of the Cerro Galán ignimbrites, *Bulletin of Volcanology*, *73*(10), 1487–1511.

Kelemen, P. B., J. A. Whitehead, E. Aharonov, and K. A. Jordahl (1995), Experiments on flow focusing in soluble porous media, with applications to melt extraction from the mantle, *Journal of Geophysical Research: Solid Earth (1978–2012)*, *100*(B1), 475.

Kirby, S., and A. Kronenberg (1987), Rheology of the Lithosphere: Selected Topics, *Reviews of Geophysics*, *25*(6), 1–26.

Lauknes, T. R., H. Zebker, and Y. Larsen (2011), InSAR Deformation Time Series Using an L1-Norm Small-Baseline Approach, *Geoscience and Remote Sensing, IEEE Transactions on*, *49*(1), 536–546.

Leidig, M., and G. Zandt (2003), Modeling of highly anisotropic crust and application to the Altiplano-Puna volcanic complex of the central Andes, *Journal of Geophysical Research: Solid Earth (1978–2012)*, *108*(B1), 1–15.

Liang, C., Q. Zeng, J. Jia, J. Jiao, and X. Cui (2013), ScanSAR interferometric processing using existing standard InSAR software for measuring large scale land deformation, *Computers & Geosciences*, *51*, 439–448.

Lipman, P. W. (2007), Incremental assembly and prolonged consolidation of Cordilleran magma chambers: Evidence from the Southern Rocky Mountain volcanic field, *Geosphere*, *3*(1), 42–70.

Lohman, R. B. (2005), Some thoughts on the use of InSAR data to constrain models of surface deformation: Noise structure and data downsampling, *Geochemistry Geophysics Geosystems*, *6*(1).

Loveless, J. P., M. E. Pritchard, and N. Kukowski (2010), Testing mechanisms of subduction zone segmentation and seismogenesis with slip distributions from recent Andean earthquakes, *Tectonphysics*, *495*, 15–33.

Lu, Z., C. Wicks, J. Power, D. Dzurisin, W. Thatcher, and T. Masterlark (2002), Interferometric Synthetic Aperture Radar Studies of Alaska Volcanoes, *IEEE*, pp. 191–194.

Lundgren, P., S. Usai, E. Sansosti, R. Lanari, M. Tesauro, G. Fornaro, and P. Berardino (2001), Modeling surface deformation observed with synthetic aper-

ture radar interferometry at Campi Flegrei caldera, *Journal of Geophysical Research: Solid Earth (1978–2012)*, *106*(B9), 19,355–19,366.

Mason, B. G., D. M. Pyle, and C. Oppenheimer (2004), The size and frequency of the largest explosive eruptions on Earth, *Bulletin of Volcanology*, *66*(8), 735–748.

Massonnet, D., P. Briole, and A. Arnaud (1995), Deflation of Mt Etna monitored by spaceborne radar interferometry, *Nature*, *375*, 567–570.

Matthews, S. J., M. Gardeweg, and R. S. J. Sparks (1997), The 1984 to 1996 cyclic activity of Lascar Volcano, northern Chile: cycles of dome growth, dome subsidence, degassing and explosive eruptions, *Bulletin of Volcanology*, *59*(1), 72–82.

McFarlin, H., D. H. Christensen, g. thompson, and S. R. McNutt (2014), Receiver Function Analyses of Uturuncu Volcano, Bolivia and Lastarria/Cordon Del Azufre Volcanoes, Chile, in *AGU 2014*.

McGlashan, N., L. D. Brown, and S. M. Kay (2008), Crustal thickness in the central Andes from teleseismically recorded depth phase precursors, *Geophys J Int*, *175*(3), 1013–1022.

McTigue, D. F. (1987), Elastic Stress and Deformation Near a Finite Spherical Magma Body: Resolution of the Point Source Paradox, *Journal of Geophysical Research: Solid Earth (1978–2012)*, *92*(B12), 12–931–12–940.

Menand, T. (2011), Physical controls and depth of emplacement of igneous bodies: A review, *Tectonphysics*, *500*(1-4), 11–19.

Menand, T., M. de Saint-Blanquat, and C. Annen (2011), Emplacement of magma pulses and growth of magma bodies, *Tectonphysics*, *500*(1-4), 1–2.

Métois, M., a. Socquet, and C. Vigny (2012), Interseismic coupling, segmentation and mechanical behavior of the central Chile subduction zone, *J geophys Res*, *117*(B3), n/a–n/a.

Métois, M., a. Socquet, C. Vigny, D. Carrizo, S. Peyrat, A. Delorme, E. Maureira, M.-C. Valderas-Bermejo, and I. Ortega (2013), Revisiting the North Chile seismic gap segmentation using GPS-derived interseismic coupling, *Geophys J Int*, *194*, 1283–1294.

Métois, M., C. Vigny, a. Socquet, A. Delorme, S. Morvan, I. Ortega, and C. M. Valderas-Bermejo (2014), GPS-derived interseismic coupling on the subduction and seismic hazards in the Atacama region, Chile, *Geophys J Int*, *196*, 644–655.

Mogi, K. (1958), Relations between the Eruptions of Various Volcanoes and the Deformations of the Ground Surfaces around them, *Bulletin of the Earthquake Research Institute*, *36*, 99–134.

Moran, S. C., C. Newhall, and D. C. Roman (2011), Failed magmatic eruptions: late-stage cessation of magma ascent, *Bulletin of Volcanology*, *73*(2), 115–122.

Muir, D., J. D. Blundy, M. Hutchinson, and A. C. Rust (2014a), Petrological imaging of an active pluton beneath Cerro Uturuncu, Bolivia, *Contributions to Mineralogy and Petrology*, pp. 1–101.

Muir, D. D., J. D. Blundy, A. C. Rust, and J. Hickey (2014b), Experimental constraints on dacite pre-eruptive magma storage conditions beneath Uturuncu Volcano, *Journal of Petrology*, *55*(4), 749–767.

Naranjo, J. (1992), Chemistry and petrological evolution of the Lastarria vol-

canic complex in the north Chilean Andes, *GEOLOGICAL MAGAZINE-LONDON-*.

Newhall, C., and D. Dzurisin (1988), *Historical Unrest at Large Calderas of the World: Vol 1&2*, U.S. Geological Survey Bulletin, Washington D.C.

Newhall, C., and D. Dzurisin (1989), Caldera Unrest, *Science (Washington, D.C.); (United States)*, *245*(4923), 1167.

Newhall, C., and S. Self (1982), The volcanic explosivity index (VEI) an estimate of explosive magnitude for historical volcanism, *Journal of Geophysical Research: Solid Earth (1978–2012)*, *87*, 1231–1238.

Newman, a., T. Dixon, G. Ofoegbu, and J. Dixon (2001), Geodetic and seismic constraints on recent activity at Long Valley Caldera , California: evidence for viscoelastic rheology, *Journal of Volcanology and Geothermal Research*, *105*(3), 183–206.

Okada, B. Y. Y. (1985), Surface deformation due to shear and tensile faults in a half-space, *Bulletin of the Seismological Society of . . .*, *75*(4), 1135–1154.

Okada, B. Y. Y. (1992), Internal deformation due to shear and tensile faults in a half-space, *Bulletin of the Seismological Society of . . .*, *82*(2), 1018–1040.

Ortiz, A. B., and H. Zebker (2007), ScanSAR-to-stripmap mode interferometry processing using ENVISAT/ASAR data, *Geoscience and Remote Sensing, IEEE Transactions on*.

Parfitt, L., and L. Wilson (2009), *Fundamentals of Physical Volcanology*, John Wiley & Sons.

Pascal, K., J. Neuberg, and E. Rivalta (2014), On precisely modelling surface deformation due to interacting magma chambers and dykes, *Geophys J Int*, *196*(1), 253–278.

Pavez, a., D. Remy, S. Bonvalot, M. Diament, G. Gabalda, J.-L. Froger, P. Julien, D. Legrand, and D. Moisset (2006), Insight into ground deformations at Lascar volcano (Chile) from SAR interferometry, photogrammetry and GPS data: Implications on volcano dynamics and future space monitoring, *Remote Sensing of Environment*, *100*(3), 307–320.

Pearse, J., and P. Lundgren (2013), Source model of deformation at Lazufre volcanic center, central Andes, constrained by InSAR time series, *Geophys Res . . .*, *40*(6), 1059–1064.

Pepe, A., E. Sansosti, P. Berardino, and R. Lanari (2005), On the Generation of ERS/ENVISAT DInSAR Time-Series Via the SBAS Technique, *Geoscience and Remote Sensing Letters, IEEE*, *2*(3), 265–269.

Pepe, A., A. B. Ortiz, P. R. Lundgren, P. A. Rosen, and R. Lanari (2011), The Stripmap-ScanSAR SBAS Approach to Fill Gaps in Stripmap Deformation Time Series With ScanSAR Data, *Geoscience and Remote Sensing, IEEE Transactions on*, *49*(12), 4788–4804.

Petford, N. (1996), Dykes or diapirs?, *Transactions of the Royal Society of Edinburgh*, *87*, 105–114.

Pinel, V., M. Poland, and A. Hooper (2014), Volcanology: Lessons learned from Synthetic Aperture Radar imagery, *Journal of Volcanology and Geothermal Research*, *289*, 81–113.

Poland, M. (2010), Learning to recognize volcanic non-eruptions, *Geology*, *38*(3), 287–288.

Poland, M., M. Hamburger, and a. Newman (2006), The changing shapes of active volcanoes: History, evolution, and future challenges for volcano geodesy, *Journal of Volcanology and Geothermal Research*, *150*, 1–13.

Polyansky, O. P., A. V. Babichev, S. N. Korobeynikov, and V. V. Reverdatto (2010), Computer modeling of granite gneiss diapirism in the Earth's crust: Controlling factors, duration, and temperature regime, *Petrology*, *18*(4), 432–446.

Pritchard, M. E., and M. Simons (2002), A satellite geodetic survey of large-scale deformation of volcanic centres in the central Andes., *Nature*, *418*(6894), 167–171.

Pritchard, M. E., and M. Simons (2004), An InSAR-based survey of volcanic deformation in the central Andes, *Geochemistry Geophysics Geosystems*, *5*(2), 1–42.

Pritchard, M. E., et al. (2014), Reconnaissance earthquake studies at nine volcanic areas of the central Andes with coincident satellite thermal and InSAR observations, *Bulletin of Volcanology*, pp. 90–103.

Ranalli, G., and D. C. Murphy (1987), Rheological stratification of the lithosphere, *Tectonphysics*, *132*(4), 281–295.

Remy, D., J.-L. Froger, H. Perfettini, S. Bonvalot, G. Gabalda, F. Albino, V. Cayol, D. Legrand, and M. D. Saint Blanquat (2014), Persistent uplift of the Lazufre volcanic complex (Central Andes): New insights from PCAIM inversion of InSAR time series and GPS data, *Geochemistry Geophysics Geosystems*, *15*(9), 3591–3611.

Richet, P., A. M. Lejeune, F. Holtz, and J. Roux (1996), Water and the viscosity of andesite melts, *Chemical Geology*.

Riller, U., I. Petrinovic, J. Ramelow, and M. Strecker (2001), Late Cenozoic tectonism, collapse caldera and plateau formation in the central Andes, *Earth˜Planet.˜Sci.˜Lett.*, *188*, 299–311.

Rivalta, E., and P. Segall (2008), Magma compressibility and the missing source for some dike intrusions, *Geophys Res . . .*, *35*(4), 0–4.

Rosen, P. A., S. Hensley, I. Joughin, F. Li, S. N. Madsen, E. Rodriguez, and R. M. Goldstein (2000), Synthetic Aperture Radar Interferometry, *Proceedings of the IEEE*, *88*(3), 333–382.

Rosen, P. A., S. Hensley, G. Peltzer, and M. Simons (2004), Updated repeat orbit interferometry package released, *Eos*, *85*(5), 47.

Rosen, P. A., S. Hensley, and C. W. Chen (2010), Measurement and Mitigation of the Ionosphere in L-band Interferometric SAR Data, in *2010 IEEE Radar Conference*, pp. 1459–1463, IEEE.

Rosen, P. A., E. Gurrola, G. F. Sacco, and H. Zebker (2012), The InSAR scientific computing environment, in *EUSAR*, pp. 730–733, VDE.

Rubin, A. M. (1992), Dike-induced faulting and graben subsidence in volcanic rift zones, *Journal of Geophysical Research: Solid Earth (1978–2012)*, *97*(B2), 1839.

Rubin, A. M. (1995), Propagation of Magma-Filled Cracks, *Anuual Review of Earth and Planetary Science*, *23*(1), 287–336.

Ruch, J., and T. R. Walter (2010), Relationship between the InSAR-measured

uplift, the structural framework, and the present-day stress field at Lazufre volcanic area, central Andes, *Tectonphysics*, *492*(1-4), 133–140.

Ruch, J., J. Anderssohn, T. R. Walter, and M. Motagh (2008), Caldera-scale inflation of the Lazufre volcanic area, South America: Evidence from InSAR, *Journal of Volcanology and Geothermal Research*, *174*(4), 337–344.

Ruch, J., a. Manconi, G. Zeni, G. Solaro, a. Pepe, M. Shirzaei, T. R. Walter, and R. Lanari (2009), Stress transfer in the Lazufre volcanic area, central Andes, *Geophys Res . . .*, *36*(22), 1–6.

Salisbury, M. J., B. R. Jicha, S. L. de Silva, B. S. Singer, N. C. Jimenez, and M. H. Ort (2011), 40Ar/39Ar chronostratigraphy of Altiplano-Puna volcanic complex ignimbrites reveals the development of a major magmatic province, *Geological Society Of America Bulletin*, *123*(5-6), 821–840.

Sambridge, M. (1999), Geophysical inversion with a neighbourhood algorithm – I. Searching a parameter space, *Geophys J Int*, *138*, 479–494.

Savage, J. C., and M. M. Clark (1982), Magmatic resurgence in Long Valley Caldera, California: possible cause of the 1980 Mammoth Lakes earthquakes, *Science (Washington, D.C.); (United States)*, *217*(4559), 531–533.

Scharroo, R., and P. Visser (1998), Precise orbit determination and gravity field improvement for the ERS satellites, *Journal of Geophysical Research: Solid Earth (1978–2012)*, *103*(C4), 8113–8127.

Schilling, F. R., G. M. Partzsch, H. Brasse, and G. Schwarz (1997), Partial melting below the magmatic arc in the central Andes deduced from geoelectromagnetic field experiments and laboratory data, *Physics of the Earth and Planetary Interiors*, *103*, 17–31.

Schilling, F. R., et al. (2006), Partial Melting in the Central Andean Crust : a Review of Geophysical, Petrophysical, and Petrologic Evidence, in *Frontiers in Earth Sciences: The Andes, Active Subduction Orogeny*, edited by O. Oncken, G. Chong, G. Franz, P. Giese, H. J. Götze, V. Ramos, M. Strecker, and P. J. Wigger, pp. 459–474, Springer, Berlin.

Segall, P. (2010), Earthquake and Volcano Deformation.

Sella, G. F. (2002), REVEL: A model for Recent plate velocities from space geodesy, *Journal of Geophysical Research: Solid Earth (1978–2012)*, *107*(B4), 2081.

Siebert, L., T. Simkin, and P. Kimberly (2011), *Volcanoes of the World*, 3 ed., University of California Press, Los Angeles, CA.

Sillitoe, R., and D. Burrows (2002), New field evidence bearing on the origin of the el laco magnetite deposit, Northern Chile, *Economic Geology*, *97*, 1101–1109.

Simons, M., and P. A. Rosen (2007), Treatise on Geophysics, Interferometric Synthetic Aperture Radar Geodesy, *Treatise on Geophysics*, *3*, 391–446.

Small, C., and T. Naumann (2001), The global distribution of human population and recent volcanism, *Global Environmental Change Part B: ...*.

Sparks, R. S. J. (1978), The dynamics of bubble formation and growth in magmas: a review and analysis, *Journal of Volcanology and Geothermal Research*, *3*(3), 1–37.

Sparks, R. S. J., C. B. Folkes, M. C. Humphreys, D. N. Barfod, J. Clavero, M. C. Sunagua, S. R. McNutt, and M. E. Pritchard (2008), Uturuncu volcano, Bolivia: Volcanic unrest due to mid-crustal magma intrusion, *American Journal of Science*, *308*(6), 727–769.

Spera, F. J. (2000), Physical Properties of Magma, in *Encyclopedia of Volcanos*, edited by H. Sigurdsson, pp. 171–190, Encyclopedia of volcanoes.

Spica, Z. J., D. Legrand, A. Iglesias, and T. R. Walter (), Lazufre Tomography, in *AGU 2014*.

Tamburello, G., T. H. Hansteen, S. Bredemeyer, A. Aiuppa, and F. Tassi (2014), Gas emissions from five volcanoes in northern Chile and implications for the volatiles budget of the Central Volcanic Zone, *Geophys Res ...*, *41*(14), 4961–4969.

Tassi, F., F. Aguilera, O. Vaselli, T. Darrah, and E. Medina (2011), Gas discharges from four remote volcanoes in northern Chile (Putana , Olca, Irruputuncu and Alitar): a geochemical survey, *Annals of Geophysics*, *54*(2), 121–136.

Thompson, A. B. (1982), Dehydration melting of pelitic rocks and the generation of H 2 O-undersaturated granitic liquids, *American Journal of Science*, *282*, 1567–1595.

Tiampo, K., J. B. Rundle, J. Fernández, and J. Langbein (2000), Spherical and ellipsoidal volcanic sources at Long Valley caldera, California, using a genetic algorithm inversion technique, *Journal of Volcanology and Geothermal Research*, *102*(3-4), 189–206.

Tilling, R. I. (2009), Advances in Geosciences Volcanism and associated hazards: the Andean perspective, *Advances in Geosciences*, *22*, 125–137.

Tizzani, P., P. Berardino, F. Casu, P. Euillades, M. Manzo, G. Ricciardi, G. Zeni, and R. Lanari (2007), Surface deformation of Long Valley caldera and Mono Basin, California, investigated with the SBAS-InSAR approach, *Remote Sensing of Environment*, *108*(3), 277–289.

Trasatti, E., C. Giunchi, and M. Bonafede (2005), Structural and rheological constraints on source depth and overpressure estimates at the Campi Flegrei caldera, Italy, *Journal of Volcanology and Geothermal Research*, *144*(1-4), 105–118.

Tullis, T. E., F. G. Horowitz, and J. Tullis (1991), Flow laws of polyphase aggregates from end-member flow laws, *Journal of Geophysical Research: Solid Earth (1978–2012)*, *96*(B5), 8081.

Turcotte, D. L., and G. Schubert (2002), *Geodynamics*, 2 ed., Cambridge University Press.

Unsworth, M. J., M. Comeau, and F. Ticona (2013), Distribution of melt beneath the Altiplano-Puna volcanic complex from magnetotelluric data, in *AGU Fall Meeting Abstracts*, p. 2601.

Venske, E., L. Siebert, and T. Simkin (2014), Volcanoes of the World (VOTW) Database 4.3.1, Smithsonian Global Volcanism Program.

Voight, B., R. P. Hoblitt, A. B. Clarke, and A. B. Lockhart (1998), Remarkable cyclic ground deformation monitored in real-time on Montserrat, and its use in eruption forecasting, *Geophys Res . . .*, *25*(18), 3405–3408.

Wallace, P. J. (2005), Volatiles in subduction zone magmas: concentrations and fluxes based on melt inclusion and volcanic gas data, *Journal of Volcanology and Geothermal Research*.

Walter, T. R., and M. Motagh (2014), Deflation and inflation of a large magma body beneath Uturuncu volcano, Bolivia? Insights from InSAR data, surface lineaments and stress modelling, *Geophys J Int*.

Ward, K. M., R. C. Porter, G. Zandt, S. L. Beck, L. S. Wagner, E. Minaya, and

H. Tavera (2013), Ambient noise tomography across the Central Andes, *Geophys J Int*.

Ward, K. M., G. Zandt, S. L. Beck, D. H. Christensen, and H. McFarlin (2014), Earth and Planetary Science Letters, *Earth˜Planet.˜Sci.˜Lett.*, *404*(C), 43–53.

Weinberg, R., and Y. Podladchikov (1995), The rise of solid-state diapirs, *Journal of Structural Geology*, *17*(8), 1183–1195.

West, M. E., E. Kukarina, and I. Koulakov (2013), Structure of Uturuncu volcano from seismic tomography, in *AGU Fall Meeting Abstracts*, p. 2600.

Whelley, P. L., J. A. Jay, E. S. Calder, M. E. Pritchard, N. J. Cassidy, S. Alcaraz, and a. Pavez (2011), Post-depositional fracturing and subsidence of pumice flow deposits: Lascar Volcano, Chile, *Bulletin of Volcanology*, *74*(2), 511–531.

Wölbern, I., B. Heit, X. Yuan, G. Asch, R. Kind, J. Viramonte, S. Tawackoli, and H. Wilke (2009), Receiver function images from the Moho and the slab beneath the Altiplano and Puna plateaus in the Central Andes, *Geophys J Int*, *177*(1), 296–308.

Wright, T. J., B. Parsons, P. C. England, and E. J. Fielding (2004a), InSAR observations of low slip rates on the major faults of western Tibet., *Science (Washington, D.C.); (United States)*, *305*(5681), 236–239.

Wright, T. J., B. Parsons, and Z. Lu (2004b), Toward mapping surface deformation in three dimensions using InSAR, *Geophys Res . . .*, *31*(1), 1–5.

Wright, T. J., C. Ebinger, J. Biggs, A. Ayele, G. Yirgu, D. Keir, and A. Stork (2006), Magma-maintained rift segmentation at continental rupture in the 2005 Afar dyking episode., *Nature*, *442*(7100), 291–294.

Xu, Z.-W., J. Wu, and Z.-S. Wu (2004), A survey of ionospheric effects on space-based radar, *Waves in Random Media*, *14*(2), S189–S273.

Yuan, X., et al. (2000), Subduction and collision processes in the Central Andes constrained by converted seismic phases., *Nature*, *408*(6815), 958–961.

Yuan, X., S. V. Sobolev, and R. Kind (2002), Moho topography in the central Andes and its geodynamic implications, *Earth˜Planet.˜Sci.˜Lett.*

Zandt, G., M. Leidig, J. Chmielowski, D. Baumont, and X. Yuan (2003), Seismic Detection and Characterization of the Altiplano-Puna Magma Body, Central Andes, *Pure and Applied Geophysics*, *160*, 789–807.

Zebker, H., P. A. Rosen, and S. Hensley (1997), Atmospheric effects in interferometric synthetic aperture radar surface deformation and topographic maps, *Journal of Geophysical Research: Solid Earth (1978–2012)*, *102*, 7547–7563.

APPENDIX A

CHAPTER 2 SUPPLEMENTAL MATERIALS

A.1 Time Series Inversion Methodology

A.1.1 Interferogram selection

Small BAseline Subset (SBAS) algorithms attempt to limit temporal and spatial decorrelation by only using interferograms under maximum timespan and maximum baseline thresholds. Our methodology differs slightly from SBAS in that we do not impose strict requirements for maximum baseline or timespan when creating interferograms, thereby incorporating more, albeit noisy, data into the analysis. This approach is advantageous in a high-altitude, arid region such as the CVZ, for which C-band coherence is typically very high for interferograms spanning several years (*Pritchard and Simons*, 2004). Before proceeding we manually identify and omit scenes with obvious unwrapping errors and ionospheric signals that are unlikely to cancel out via stacking or inversion.

A.1.2 Masking

Mask files are generated such that the trend-removed phase variance of a 5x5 pixel box is normalized to have a value between 0 and 1. These values serve as an estimate of Signal-to-Noise Ratio (SNR) with 0 being very decorrelated, and 1 meaning pixel values are highly correlated with adjacent pixels. Omitting pixels that have mask values under a specified threshold sacrifices spatial cover-

age for data quality. We experimented with various mask threshold values and found that a threshold of 0.1 successfully removes spurious processing artifacts while maintaining spatial continuity in inversion results. However, it is important to note that this masking scheme will retain signals related to correlated atmospheric noise. We also require that pixels are coherent in more than 10 interferograms to increase the probability that atmospheric artifacts will average out.

A.1.3 Combination of ERS and Envisat Interferograms

Although ERS and Envisat are both C-band satellites and their viewing geometries are nearly identical, the slightly different carrier frequencies for each satellite prohibit the formation of cross-interferograms. However, interferograms generated from each satellite may be combined via InSAR inversion techniques as a post-processing step (e.g. *Pepe et al.*, 2005). To efficiently combine ERS and Envisat Interferograms, we assign them an equal wavelength of 5.64 cm, which represents a slight departure from the normalization procedure outlined by (*Pepe et al.*, 2005). ERS operates with a wavelength of 5.656 cm whereas Envisat uses a 5.623 m. This difference of 0.17 mm can accumulate errors when converting from unwrapped phase to LOS deformation, but stays at the sub-millimeter level as long as there are less than 6 fringes in an unwrapped interferogram. Our uncertainty analysis suggests that at worst this discrepancy is an order of magnitude less than the overall uncertainty in our measured velocities.

A.1.4 Interpolation

While interferograms in the CVZ benefit from high coherence, long tracks of InSAR data often contain large data gaps and the spatial extents of ERS and Envisat scenes are not identical. For these reasons we do not interpolate masked data points before performing the inversion, as doing so with standard techniques can fill in large regions with spurious data. In order to avoid interpolation we reform the design matrix for each pixel within our rectified grid, using only dates for which there is a coherent measurement of deformation. This has the disadvantage of reducing temporal resolution for some pixels; however, by setting the masking threshold to a low value (0.1) loss of temporal coverage is minimized.

A.1.5 Orbital ramp removal

Misestimated orbits often cause linear ramps in an interferogram, and it has been shown that quadratic ramps are common to long tracks (*Fournier et al.*, 2011). In addition, some tectonic signals, such as subduction-related interseismic deformation and orogenic uplift, can cause long wavelength signals on the order of 100 km in interferograms spanning several years. Volcanic deformation typically occurs at spatial scales of 1-10 km, and can therefore be obscured if high amplitude, long wavelength ramps are present. We therefore remove a best-fit surface to each interferogram (excluding regions of known deformation signals) before the inversion. Ramp removal also serves as a normalization step by forcing the mean value of background pixels in an interferogram to be zero.

It is important to note that ramp removal will remove real signals in some

cases. For example, at Uturuncu there is evidence for bowl-shaped subsidence surrounding the uplift signal with a diameter of 150 km. We report further on this feature in the results section. In track 89 the diameter of this broad zone of subsidence covers most of the scene. Consequently, removal of a best-fitting quadratic surface from track 89 interferograms would eliminate the moat signal, whose wavelength of approximately 150 km is comparable to the track's azimuthal extent of 220 km. *Fournier et al.* (2011) recommend quadratic ramp removal for much longer tracks, and we therefore use a linear ramp removal for track 89, and quadratic ramp removal for all other tracks in this study.

A.1.6 Filtering

As a final step, SBAS-based algorithms often perform a series of temporal and spatial filters to remove signals related to Digital Elevation Model (DEM) errors and atmospheric noise (*Berardino et al.*, 2002). We do not include a term for topography errors. We also do not apply atmospheric filters, which require an a priori model for the characteristic wavelength of correlated noise throughout the track (e.g. *Lohman*, 2005). However, the long tracks of data used in this study contain significant variability in noise characteristics that depend on many factors such as distance from the coast, relief, and micro-climates. We assume that large atmospheric signals will cancel out through stacking or time series inversion (as long as interferograms containing the date with strong atmospheric signals is paired with sufficient other dates). Nevertheless, persistent or unique atmospheric signals may propagate through stacking and time series. We therefore examined the correlation between calculated velocities and topography for any suspected volcanic deformation signals, and confirmed that

significant trends were not present.

A.2 Mogi Source Inversion

Here we present additional figures demonstrating the inverse modeling results for newly-discovered deformation centers in this study. Figures A.1 and A.2 shows the data, model, residual and source location for Cerro Overo during periods of subsidence and uplift. Figure A.3 is the same plot for the uplift episode at Putana Volcano.

A.3 Uturuncu and Lazufre Source Geometry

Assuming inflation sources are embedded in an elastic or maxwell viscoelastic half-space, the location of maximum uplift in the radar line-of-sight will be a function of both vertical and horizontal displacements (*Fialko et al.*, 2001a; *Fialko and Pearse*, 2012). Because the geometry of the inflation source contributes to the ratio of horizontal to vertical displacement at the surface, when viewed from different angles the location of maximum offset will vary. Here we present additional figures showing offset of maximum LOS uplift in ascending and descending tracks over Uturuncu (Figure A.4) and Lazufre (Figure A.5).

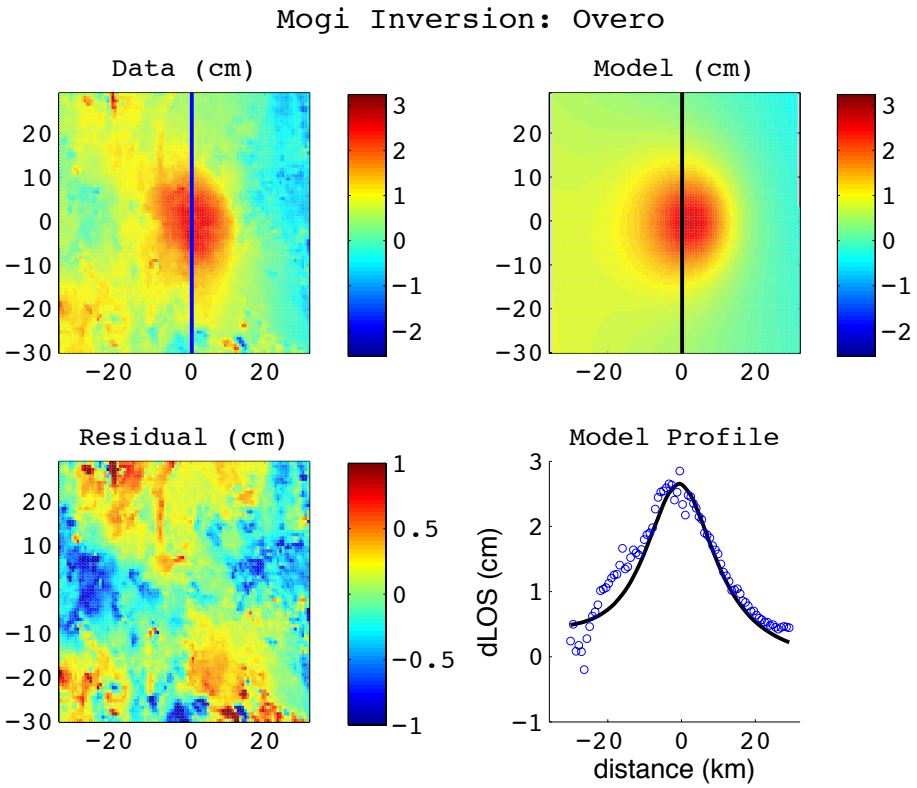

Figure A.1: Inverse modeling results for subsidence episode at Cerro Overo. Best-fit parameters are listed in table 3 of the main text.

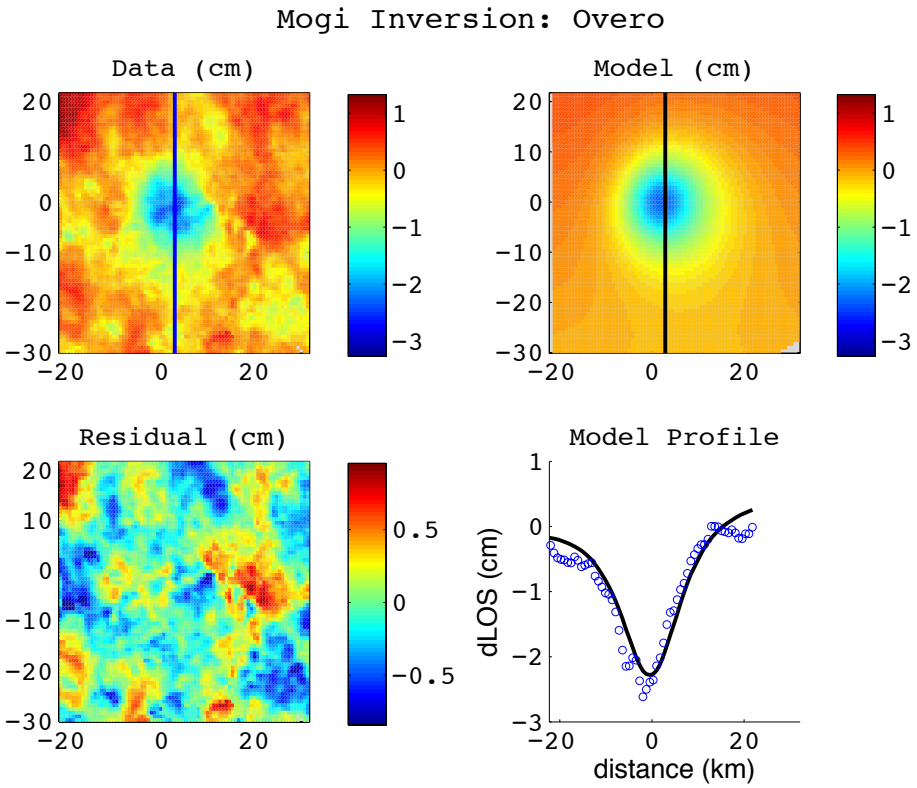

Figure A.2: Inverse modeling results for uplift episode near Cerro Overo. Best-fit parameters are listed in table 3 of the main text.

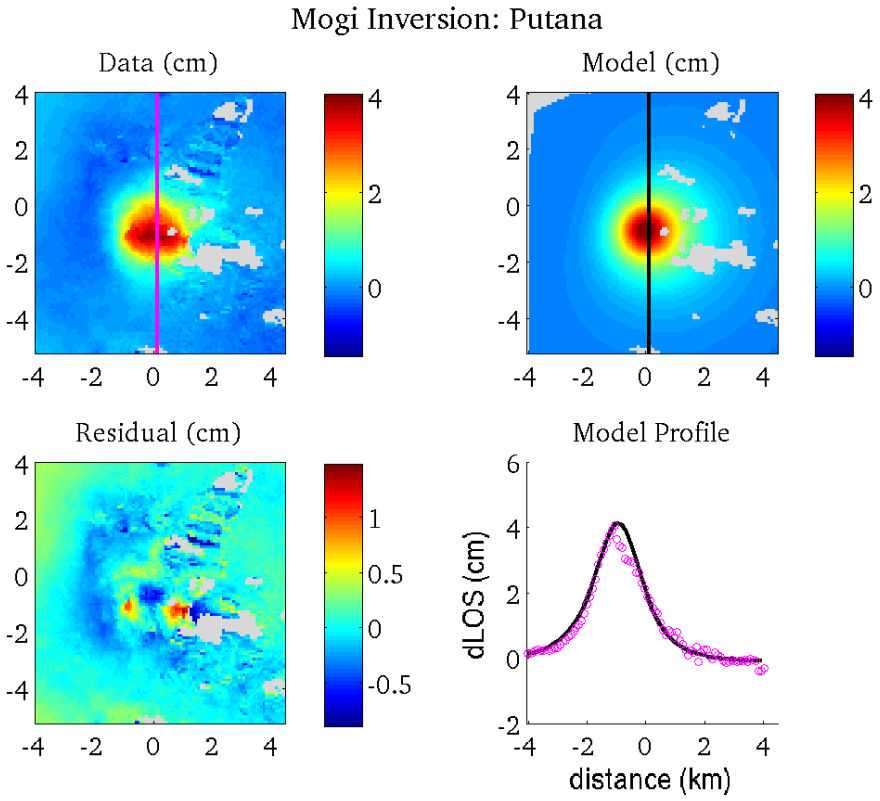

Figure A.3: Inverse modeling results for short-lived uplift at Putana Volcano. Best-fit parameters are listed in table 3 of the main text

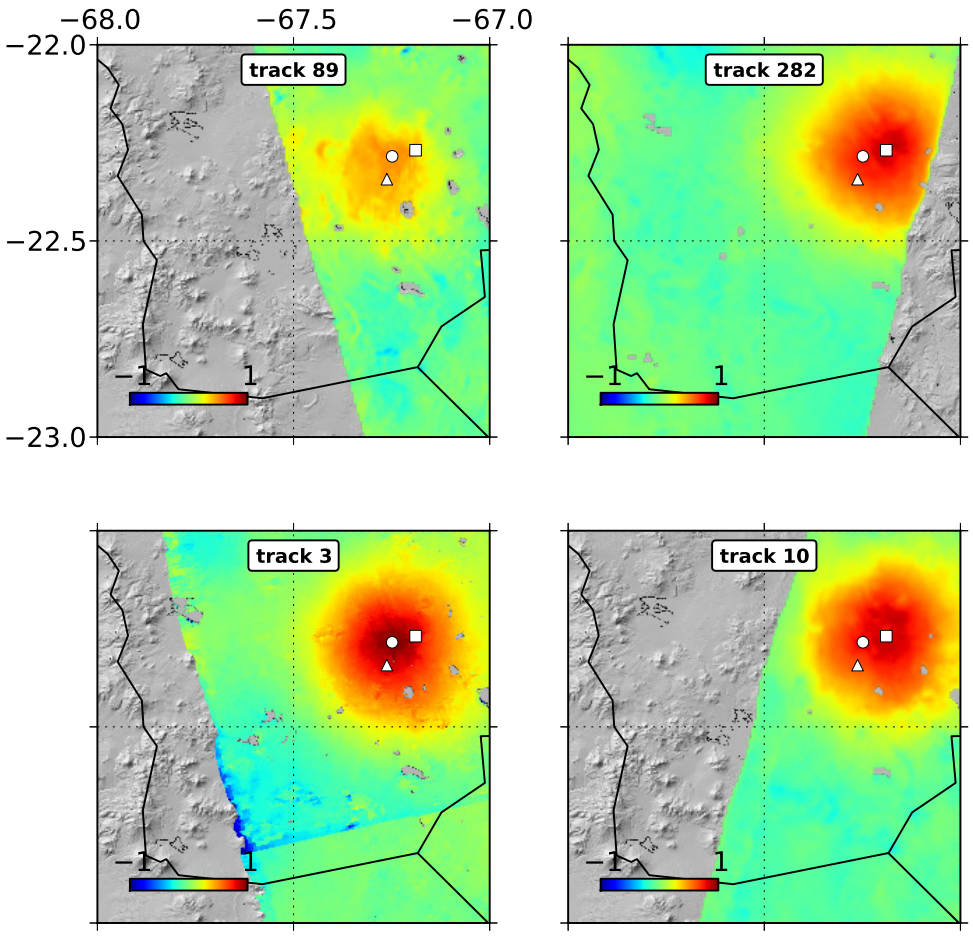

Figure A.4: Offsets of location of maximum uplift for interferogram stacks covering Uturuncu Volcano. The white square marks center of uplift in descending tracks 10 and 282 (offset is indistinguishable). The white circle marks the center of deformation in ascending track 3 which is offset to the southwest 6 $\pm$ 2 km. The white triangle marks the approximate center of deformation in track 89, although the more diffuse uplift pattern adds significant uncertainty to this location.

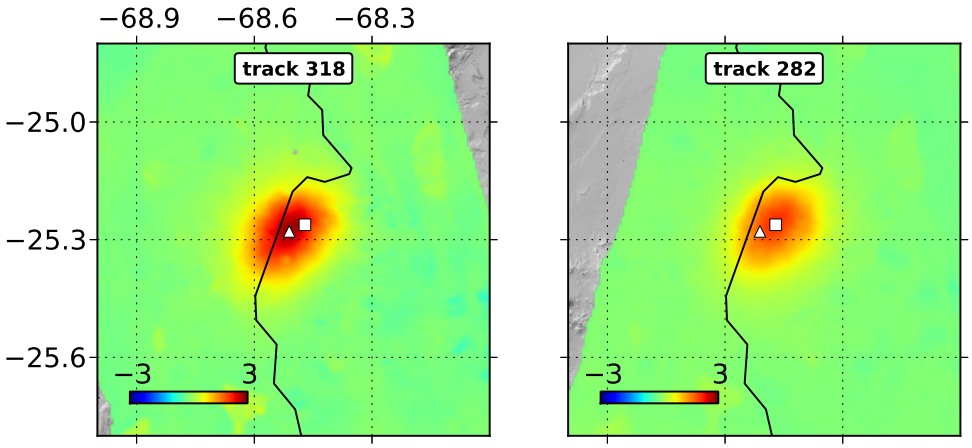

Figure A.5: Offsets of location of maximum uplift for interferogram stacks covering the Lazufre uplift. The white square marks center of uplift in descending track 282. The white triangle marks the center of deformation in ascending track 318 which is offset to the southwest 4 ± 2 km.

APPENDIX B

CHAPTER 3 SUPPLEMENTAL MATERIALS

B.1 GPS Processing Methodology

B.1.1 Calculation of interseismic velocities

In order to estimate the expected displacements at our installed continuous and campaign GPS stations due to interseismic deformation we took two approaches. First, we used the slip model described in *Fournier et al.* (2011) to predict the magnitude of deformation along the volcanic arc. In figure B.1 we show the model prediction (components in NS, EW, and Z directions) projected into the radar line-of-sight for Envisat beam 2 along the strike of the volcanic arc. We note that the contribution of absolute displacements is less than 1.3 mm/yr, and the relative displacements within an interferogram are expected to be less than 0.5 mm/yr. Second, we interpolated regional interseismic campaign data from a series of recent papers (*Métois et al.*, 2013, 2014).

B.1.2 Estimation of seasonal signal

We used Gravity Recovery and Climate Experiment (GRACE) estimates of seasonal density variation to remove the seasonal displacement signal from both continuous and campaign GPS stations (*Fu and Freymueller*, 2012; *Fu et al.*, 2013).

B.2 New InSAR Observations

B.2.1 ALOS

Descending data covering Uturuncu is very sparse, with only 3 dates between 2007/07/21 and 2008/01/21. Ascending data is more abundant, from tracks 98 and 99 with 49 and 42 acquisitions respectively (Table B.1). However, the ascending data contains significant ionospheric noise, rendering many scenes unusable for surface deformation studies. Ascending data is taken approximately 11:30PM local time, descending is 10:30AM local time.

B.2.2 TSX

Of the currently functioning radar satellites, TerraSAR-X (TSX) acquisitions over Uturuncu begin in 06/2012, and currently end in 10/2014. We have generated a single interferogram that spans this 2 year period, but do not observe deformation. At previous rates we expect 15 mm of accumulated relative displacement would be at the limit of detectable signal, such that several more years of observation may be required before ground deformation is discernible in TSX acquisitions.

B.3 Finite Element Benchmark

We have benchmarked our finite element mesh against the first order semi-analytical solution of for two point expansion sources in a homogeneous elastic

half space. The solution is derived in a variety of sources (e.g. *Mogi*, 1958; *McTigue*, 1987):

$$u_z = \frac{(1-\nu)pa^3}{\mu}\left[\frac{d}{(\rho^2+d^2)^{3/2}}\right] u_\rho = \frac{(1-\nu)pa^3}{\mu}\left[\frac{\rho}{(\rho^2+d^2)^{3/2}}\right] \tag{B.1}$$

Where ν is crustal poisson's ratio, μ is crustal shear modulus, p is the spherical source pressure (where positive values represent expansion), a is the source radius, d is the source depth and ρ is the radial distance from the source epicenter. The equations are valid as long as $d >> a$. It is worth noting that the above equation is derived from the solid mechanics equilibrium equation (force balance) and the small-strain elastic constitutive law. Often, the change in volume of the chamber is of most interest from a volcanic hazards perspective, and fortuitously it is straightforward to do this by integrating the full-space radial displacements, $u_r = \frac{pa^3}{4\mu r^2}$, around the chamber surface. Once again, since this relationship requires the radial displacements for a *full-space* solution, and thus is an approximation again that only holds for $a << d$.

$$u_z = \frac{(1-\nu)\Delta V}{\pi}\left[\frac{d}{(\rho^2+d^2)^{3/2}}\right] u_\rho = \frac{(1-\nu)\Delta V}{\pi}\left[\frac{\rho}{(\rho^2+d^2)^{3/2}}\right] \tag{B.2}$$

While this model is often described as pressurization of spherical void or chamber, we remark that it may be more appropriate to envision a region that is roughly equidimensional in which multiple intrusions may occur. As an example, a rapid series of intrusions that stall at 20 km would be well-described by this model so long as the intrusions are constrained to a volume described by $\frac{4}{3}\pi r^3$, where $r \approx 4km$.

Finite element computations are performed using Pylith Software (*Aagaard*

et al., 2013). Figure 3.13 shows the agreement between the finite element and analytical solution. We accept 10% errors between the numerical and analytical solution as acceptable in order to minimize computation time.

B.4 Viscoelastic Finite Element Model

Caldera deformation has been modeled in the past using viscoelastic formulations for a variety of compelling reasons. First, for a typical geothermal gradient, deep intrusions occur in hot country rock, which deforms according to steady-state creep laws (e.g. *Carter and Tsenn*, 1987). Stalled intrusions supply additional heat to surrounding country rock, raising temperature and lowering viscosity. Furthermore, post-seismic transients have shown that evidence for viscosities in the lower crust and upper mantle on the order of $10^{17} - 10^{19}$ Pa s (e.g. *Freed et al.*, 2007). Thus, volcanic models have been considered in which the entire crust is treated as a viscoelastic material (*Bonafede et al.*, 1986), or a shell of material surrounding the reservoir is treated as viscoelastic (e.g. *Newman et al.*, 2001; *Del Negro et al.*, 2009). There are several other practical reasons for including viscoelasticity. First, a viscoelastic rheology effectively reduces the pressure required for a given amplitude of surface deformation, thereby overcoming physically unrealistic determinations of reservoir overpressure for elastic crust (e.g. *Hickey et al.*, 2013). Second, time dependent deformation can be explained via material response rather than changes in intrusion rate, which may permit more realistic intrusion time histories.

Many viscoelastic formulations exist, but perhaps the most commonly utilized in volcano geodesy are the linear maxwell (MX), standard linear solid

(SLS), and nonlinear powerlaw (PL) model. The appropriate constitutive law is likely site dependent, and for Uturuncu we appeal to various regional datasets and previous studies to approximate mid and lower crustal viscosities.

Arndt et al. (1997) studied thermal and rheological properties of granodioritic rocks from the North Chilean Coastal Cordillera. While these samples are from the exhumed Jurassic Arc, they are believed to resemble current upper mid crustal rocks underlaying the active arc. Importantly, these rocks show a strong decrease in thermal conductivity 2.71 W/ m K to 1.66 W/m K at 1 GPa and 800 C. Given the high surface heat-flow of $> 100mW/m^2$ in the Altiplano Plateau, these conductivities imply the basalt solidus (1250 C) is reached at approximately 35 km depth, which is unreasonable given thicker crust of felsic composition. These measurements may be explained if convective heat transfer occurs in the crust. Thermally-activated creep in the samples is calculated based on combing dominant quartz and plagioclase phase power laws (*Tullis et al.*, 1991), and resultant viscosities at 35 km are within the range 10^{17} to 10^{19} Pa s. Given an order of magnitude shear modulus of 10 GPa, these viscosities correspond to relaxation times of 0.3 to 30 years respectively.

B.4.1 Viscoelastic Results

Viscoelastic material introduces a trade-off between time-dependent pressurization versus time-dependent material creep. For example, linear uplift rates could be caused by continuous supply of magma into an elastic crust. Alternatively, a single batch of magma intruded into maxwell viscoelastic material causes a linear time-dependent response (*Bonafede et al.*, 1986). This is well il-

lustrated in Figure B.2), which shows a linear vertical uplift rate of 13 mm/yr for constant overpressures of 10 MPa/yr and 50 MPa/yr, and a crustal viscosity of 10^{18} Pa s. The time zero solution corresponds to the elastic solution. We note that the point of transition from uplift to subsidence remains essentially constant in time, but the moat of subsidence is seen to deepen and grow laterally out from the center of deformation. Reducing the viscosity achieves a given deformation state in a shorter amount of time.

A second model treats the upper 10 km of the crust as elastic in accordance with seismically-determined BDT. Consequently, the uplift rate diminishes significantly to 0.8 mm/yr, requiring increased pressurization, weaker materials, or a thinner elastic cap to match observations.

Unfortunately, continuous GPS data do not yet capture displacement transients that could be diagnostic of viscoelastic rheology, but the lack of significant displacements in 4 years is informative. Assuming a cessation of overpressure, SLS, Kelvin-Voight, or Powerlaw formulations predict time-dependent subsidence as the material returns to approximately its pre-pressurized state. Alternatively, Maxwell material is predicted to undergo instantaneous subsidence corresponding to an elastic component, followed by no deformation.

B.5 Dynamics of transfer between reservoirs

The dipole model only considers the initial and final states of magma migration, and consequently the dynamics of transport remain unaddressed. There are three predominate theories for how magma ascends through the crust: porous flow, dyking, and diapirism, each with equations for theoretical ascent rates

(e.g. *Dosseto et al.*, 2011). One intriguing implication of the dipole model at Uturuncu is that it provides a framework for assessing melt transport rates. If InSAR observations are truly recording an elastic response of the crust, the implication is that transport has a timescale that matches the period of observation. In other words, magma ascends from a concentrated region in the lower crust approximately 30 km to the mid crust quasi-steadily over 20 years. Thus, ascent velocities are required on the order of 10 km/yr (or $3e{-}4$ m/s). Petrologic measurements of ascent rates for the deep sections of plumbing systems are scarce, but one study of Mt Etna suggests $3e{-}3$ m/s (*Armienti et al.*, 2012). We note that while InSAR data implies a constant rate over the last 20 years, radar acquisition gaps ranging from 1 month to several years may contribute to some temporal aliasing. Nevertheless, in the following discussion we assume a constant ascent velocity over the observational period, and consider which ascent mechanism if any, is viable.

B.5.1 Diapirism

Diapiric ascent requires en masse buoyant rise of material (e.g (*Weinberg and Podladchikov*, 1995)). Diapir rise is typically modeled as the buoyant rise of a solid sphere through liquid fluid ("Stoke's flow"):

$$v_s = \frac{2(\rho_l - \rho_s)ga^2}{9\eta_l} \tag{B.3}$$

For the extremely high viscosities of crustal rocks ($\eta_l = 10^{19} Pas$), ascent of a 2-3 km radius buoyant rock mass should take place over million year timescales. Consequently, to first order, we do not expect to observe significant deforma-

tion transients in GPS measurements. Ascent rates are increased by assuming temperature-dependent powerlaw viscosities for thermally perturbed crust (e.g. *Polyansky et al.*, 2010; *Fialko and Pearse*, 2012); however, the required 10 km/yr is still not achieved.

The Stoke's flow equation has been applied in a different manner to determine 10 km/hr ascent speeds of lavas through the lithosphere in the following fashion: In order to entrain peridotite xenoliths, the relative velocity v_s of the xenolith must equal the velocity of its surroundings (magma ascent velocity). So looking at the largest peridotite xenoliths in Kilauea lavas gives an extraordinary magma ascent estimate of 10 km/hr (or 3 m/s), which indicates that magma can traverse 100 km thick lithosphere in 32 hours. Application of this methodology to Uturuncu is questionable given the vastly different tectonic setting, magma composition, and lack of lower crustal xenoliths.

B.5.2 Porous flow

Porous flow is often invoked to describe magmatism at mid ocean ridges (e.g (*Kelemen et al.*, 1995; *Huppert and Woods*, 2006)). A basic estimate for porous flow velocities comes from Darcy's law and an assumed permeability model. Assuming equal pressures in the liquid and solid matrix, after *Turcotte and Schubert* (2002):

$$v_l - v_s = -\frac{b^2 \phi (\rho_s - \rho_l) g}{24 \pi \eta_l} \tag{B.4}$$

Upward motion of the solid fraction is predicted to be on the order of 1

mm/yr assuming typical crustal values. Whereas the liquid phase moves at 1-10 m/yr rates. Ascent via porous flow is thus orders of magnitude slower than rates required by the dipole model.

B.5.3 Dykes

There are myriad publications that address theory and field studies of dyke propagation; for review we refer to *Rubin* (1995). On a basic level, dykes are planar intrusive bodies that have been observed to propagate at 1 m/s in the shallow crust. Some field exposures show linear dyke swarms that extend for 10's of km, which propagate in the direction of the direction of locally most compressive stress. *Clemens and Mawer* (1992) argue that for pluton formation on geologically reasonable timescales, granite melt must be trasnported via dyke systems.

B.5.4 Pipe

We envision a pipe to represent an idealization of a network of dykes continuously traversing the crust underneath Uturuncu. For buoyancy-driven Poisuelle flow in an existing cylindrical pipe, the average ascent velocity velocity is given by *Turcotte and Schubert* (2002) (section 6-48):

$$v = \frac{(\rho_s - \rho_l) g R^2}{8 \eta_l} \tag{B.5}$$

As with porous flow, the liquid velocity depends on the radius squared.

Satellite	PathOrbit	Geometry	# Dates	# IFGs	Date1	Date2	$B_\perp$
ALOS	420	Dsc.	4	3	2007/07/21	2008/01/21	690
ALOS	98	Asc.	17	49	2007/03/05	2011/03/16	2000
ALOS	99	Asc.	14	42	2007/02/04	2011/02/15	2000
TSX	111_009	Dsc.	6	8	2012/06/10	2014/10/27	460

Table B.1: Recent InSAR Data covering Uturuncu Volcano. For each track, we list the orbit direction (Asc = Ascending, Dsc = Descending), the number of SAR images (# Dates), the number interferograms (# IFG's), and the first and last dates of those SAR images (Date1 and Date2), the maximum perpendicular baseline used as a criterion for generating interferograms ($B_\perp \max[\mathrm{m}]$). In addition to minimum perpendicular baseline, interferograms were only made for timespans greater than 1 year. The incidence angle is approximately 36 degrees for TSX, and is 34 degrees for all ALOS tracks.

However, because the pipe has a much larger radius compared to the pores, much higher velocities are possible. For example, the required velocity of 3e-4 m/s is achievable with a radius of just 0.3 mm given the same parameters used in the previous porous flow calculation. The large compressive stresses in the lower crust argue against maintaining an open pipe. However, assuming a conduit does exist, such a configuration would provide an upper bound on ascent velocity through the crust.

B.5.5 Summary

If deformation at Uturuncu is predominantly elastic, this presents a problem in that the commonly-invoked magmatic transport mechanisms underpredict the required ascent velocities. In particular, it is impossible to achieve required ascent velocities of 3e-4 m/s with first order estimates of diapiric ascent or porous flow. Required ascent velocities can be achieved with conduit flow models (e.g. pre-existing fracture network), although maintaining an open pathway over tens of km throughout the lower crust is difficult to justify.

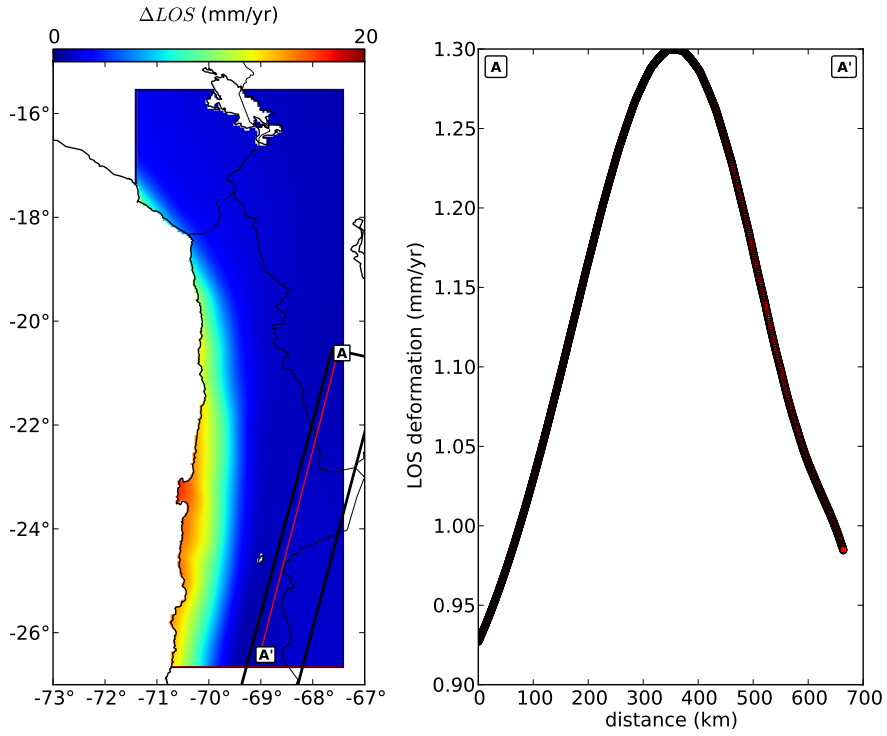

Figure B.1: Predicted interseismic displacement based on the model of *Fournier et al.* (2011). Displacement magnitudes are projected into a radar line-of-sight assuming a constant incidence angle of 23 degrees and heading of -167 degrees (average values for Envisat descending beam 2) throughout the model domain. Black outline shows the extent of track 282 within the region of the interseismic deformation model. The A-A profile demonstrates that expected interseismic signals are expected to be less than 1.3 mm/yr in radar line-of-sight at Uturuncu and Lazufre.

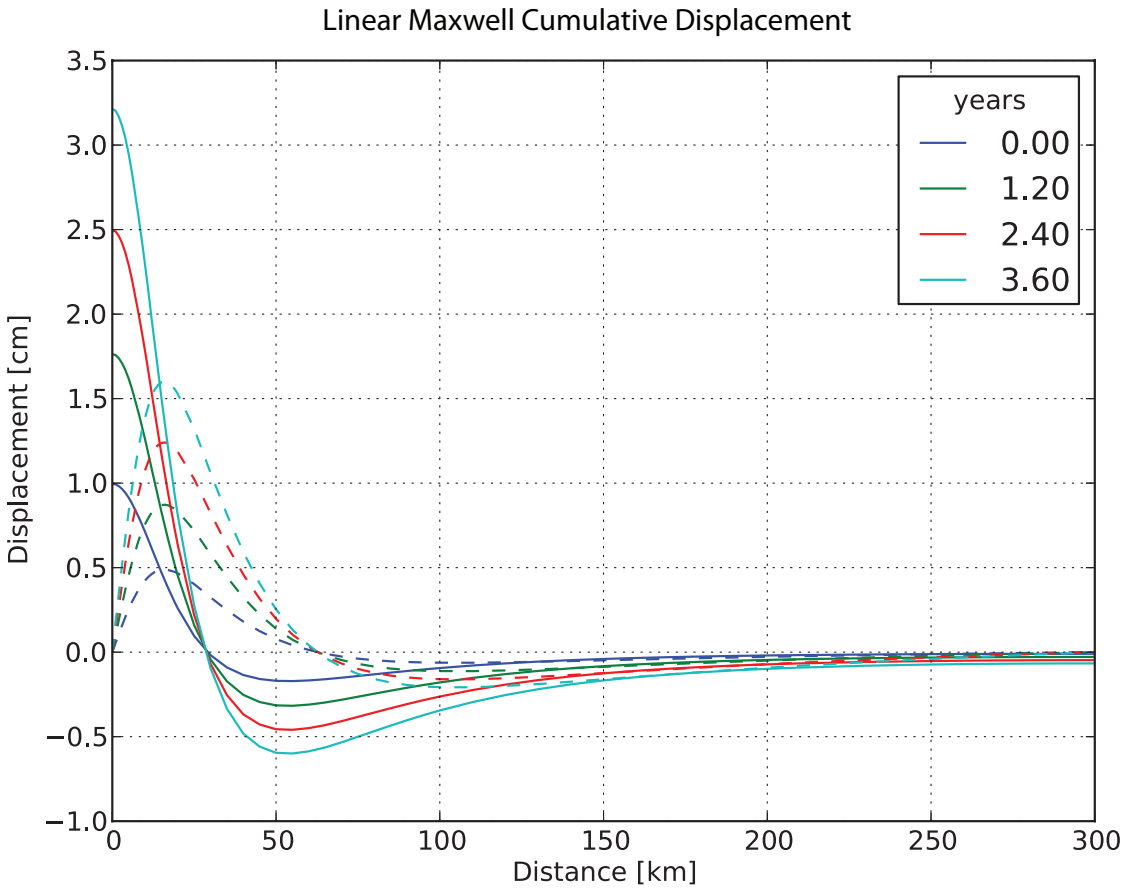

Figure B.2: Dipole surface deformation predicted for applied constant pressure in a linear maxwell viscoelastic crust ($\eta = 10^{18}$ Pa s, $\tau \approx 1yr$). Solid colors are vertical displacements, dashed lines are radial displacements. Both the uplift and peripheral subsidence decrease at linear rates in agreement with geodetic data. Note that the transition from uplift to subsidence stays fixed, while the moat grows in amplitude and radial extent.

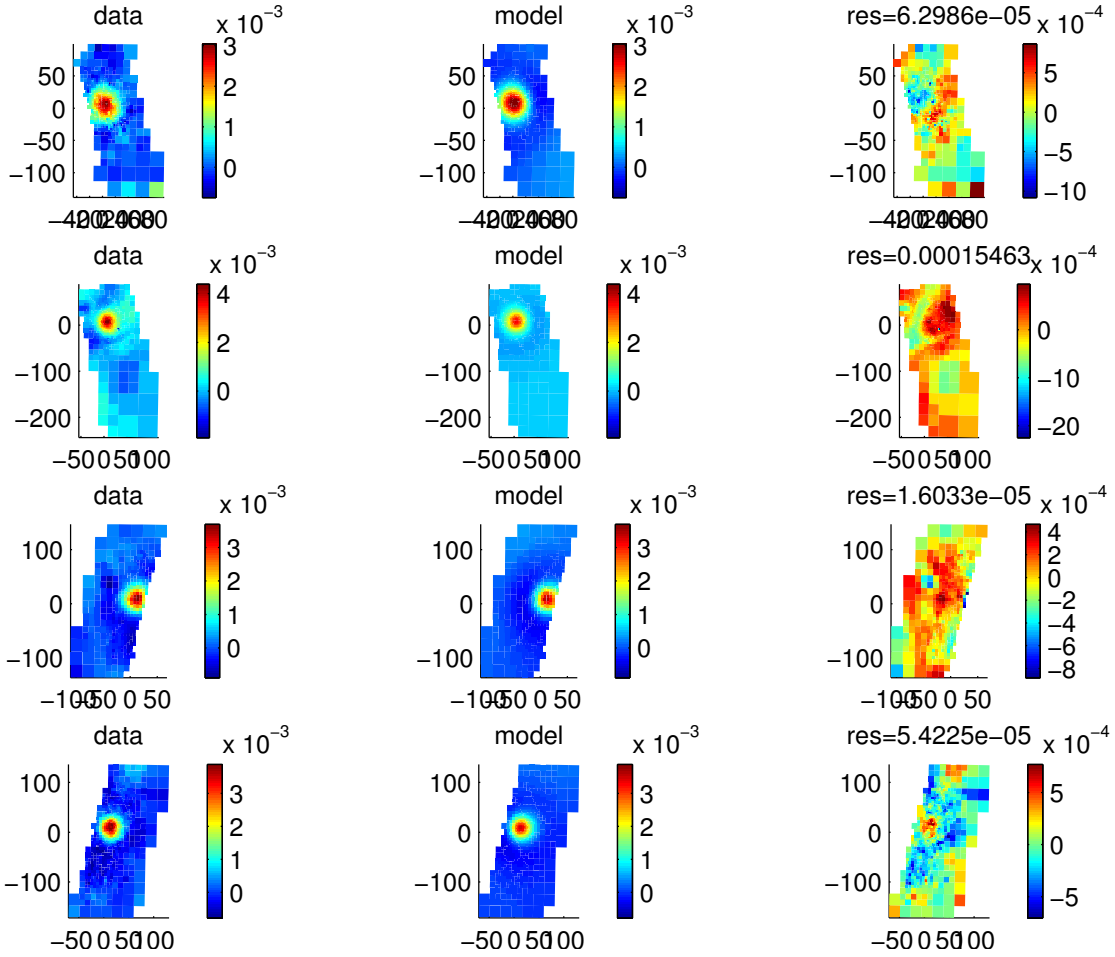

Figure B.3: Neighborhood Algorithm joint inversion using four InSAR tracks (from top to bottom: 89, 3, 282, 10). The left column contains resampled InSAR velocity maps, the middle column is prediction of surface displacements from best-fit model, and right column contains residual maps. Inversion assumes isotropic, homogeneous, Poissonian crust.

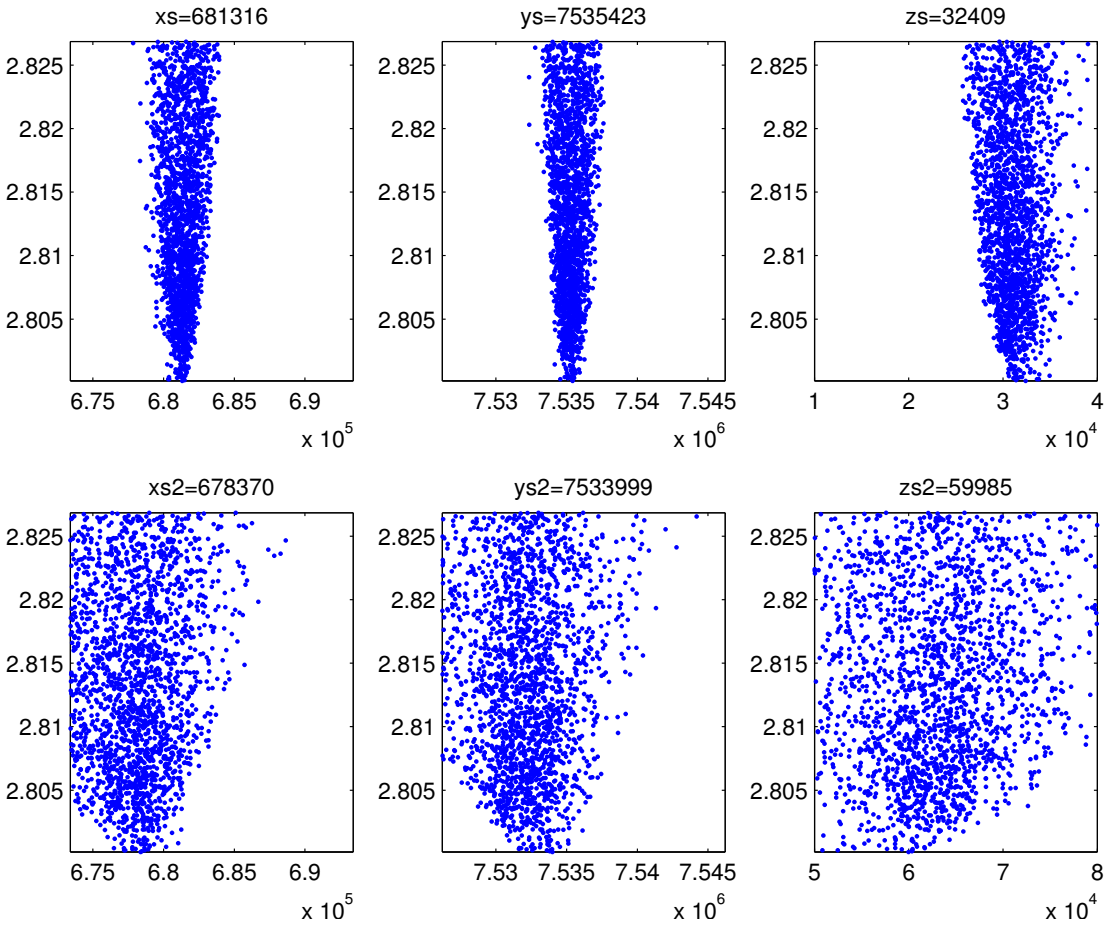

Figure B.4: Parameter space of reservoir locations queried in Neighborhood Algorithm joint inversion using four InSAR tracks to determine best fit solution shown in Figure B.3.

APPENDIX C

GLOSSARY

ACRONYMS

APMB Altiplano-Puna Melt Body.

APULVZ Altiplano-Puna Ultra Low Velocity Zone.

APVC Altiplano-Puna Volcanic Complex.

AVZ Austral Andes Volcanic Zone.

CVZ Central Andes Volcanic Zone.

ERS-1 European Remote Sensing Satellite-1.

GPS Global Positioning System.

InSAR Interferometric Synthetic Aperture Radar.

ITRF08 International Terrestrial Reference Frame 2008.

NVZ Northen Andes Volcanic Zone.

SVZ Southern Andes Volcanic Zone.

VEI Volcano Explosivity Index.

VOTW Volcanoes Of The World Database (Smithsonian).